

---

Electronic Theses and Dissertations, 2004-2019


---

2012

## High-efficiency Blue Phase Liquid Crystal Displays

Yan Li

University of Central Florida

 Part of the [Electromagnetics and Photonics Commons](#), and the [Optics Commons](#)  
Find similar works at: <https://stars.library.ucf.edu/etd>  
University of Central Florida Libraries <http://library.ucf.edu>

This Doctoral Dissertation (Open Access) is brought to you for free and open access by STARS. It has been accepted for inclusion in Electronic Theses and Dissertations, 2004-2019 by an authorized administrator of STARS. For more information, please contact [STARS@ucf.edu](mailto:STARS@ucf.edu).

---

### STARS Citation

Li, Yan, "High-efficiency Blue Phase Liquid Crystal Displays" (2012). *Electronic Theses and Dissertations, 2004-2019*. 2347.

<https://stars.library.ucf.edu/etd/2347>

# **HIGH-EFFICIENCY BLUE PHASE LIQUID CRYSTAL DISPLAYS**

by

YAN LI

B.S. Zhejiang University, P. R. China, 2005

M.S. Zhejiang University, P. R. China, 2007

A dissertation submitted in partial fulfillment of the requirements  
for the degree of Doctor of Philosophy  
in the College of Optics and Photonics  
at the University of Central Florida  
Orlando, Florida

Fall Term  
2012

Major Professor: Shin-Tson Wu

©2012 Yan Li

## ABSTRACT

Blue phase liquid crystals (BPLCs) have a delicate lattice structure existing between chiral nematic and isotropic phases, with a stable temperature range of about 2 K. But due to short coherent length, these self-assembled nano-structured BPLCs have a fast response time. In the past three decades, the application of BPLC has been rather limited because of its narrow temperature range. In 2002, Kikuchi et al. developed a polymer stabilization method to extend the blue-phase temperature range to more than 60 K. This opens a new gateway for display and photonic applications.

In this dissertation, I investigate the material properties of polymer-stabilized BPLCs. According to the Gerber's model, the Kerr constant of a BPLC is linearly proportional to the dielectric anisotropy of the LC host. Therefore, in the frequency domain, the relaxation of the Kerr constant follows the same trend as the dielectric relaxation of the host LC. I have carried out experiments to validate the theoretical predictions, and proposed a model called *extended Cole-Cole model* to describe the relaxation of the Kerr constant. On the other hand, because of the linear relationship, the Kerr constant should have the same sign as the dielectric anisotropy of the LC host; that is, a positive or negative Kerr constant results from positive ( $\Delta\varepsilon > 0$ ) or negative host LCs ( $\Delta\varepsilon < 0$ ), respectively. BPLCs with a positive Kerr constant have been studied extensively, but there has been no study on negative  $\Delta\varepsilon$  polymer-stabilized BPLCs. Therefore, I have prepared a BPLC mixture using a negative  $\Delta\varepsilon$  LC host and investigated its electro-optic properties. I have demonstrated that indeed the induced birefringence and Kerr constant are of negative sign.

Due to the fast response time of BPLCs, color sequential display is made possible

without color breakup. By removing the spatial color filters, the optical efficiency and resolution density are both tripled. With other advantages such as alignment free and wide viewing angle, polymer-stabilized BPLC is emerging as a promising candidate for next-generation displays.

However, the optical efficiency of the BPLC cell is relatively low and the operating voltage is quite high using conventional in-plane-switching electrodes. I have proposed several device structures for improving the optical efficiency of transmissive BPLC cells. Significant improvement in transmittance is achieved by using enhanced protrusion electrodes, and a 100% transmittance is achievable using complementary enhanced protrusion electrode structure.

For a conventional transmissive blue phase LCD, although it has superb performances indoor, when exposed to strong sunlight the displayed images could be washed out, leading to a degraded contrast ratio and readability. To overcome the sunlight readability problem, a common approach is to adaptively boost the backlight intensity, but the tradeoff is in the increased power consumption. Here, I have proposed a transflective blue phase LCD where the backlight is turned on in dark surroundings while ambient light is used to illuminate the displayed images in bright surroundings. Therefore, a good contrast ratio is preserved even for a strong ambient. I have proposed two transflective blue phase LCD structures, both of which have single cell gap, single gamma driving, reasonably wide view angle, low power consumption, and high optical efficiency.

Among all the 3D technologies, integral imaging is an attractive approach due to its high efficiency and real image depth. However, the optimum observation distance should be adjusted as the displayed image depth changes. This requires a fast focal length change of an adaptive lens array. BPLC adaptive lenses are a good candidate because of their intrinsic fast response time. I have proposed several BPLC lens structures which are polarization independent and exhibit a

parabolic phase profile in addition to fast response time.

To meet the low power consumption requirement set by Energy Star, high optical efficiency is among the top lists of next-generation LCDs. In this dissertation, I have demonstrated some new device structures for improving the optical efficiency of a polymer-stabilized BPLC transmissive display and proposed sunlight readable transfective blue-phase LCDs by utilizing ambient light to reduce the power consumption. Moreover, we have proposed several blue-phase LC adaptive lenses for high efficiency 3D displays.

## **ACKNOWLEDGMENTS**

I would like to express my gratitude to many people who have helped me: my advisor Shin-Tson Wu, his wife, all the professors in my committee, my group members, and my parents.

# TABLE OF CONTENTS

LIST OF FIGURES .....	x
CHAPTER 1: INTRODUCTION.....	1
1.1 Liquid Crystals .....	1
1.1.1 Nematic Phases .....	1
1.1.2 Chiral Phases.....	2
1.1.3 Blue Phases .....	4
1.1 Polymer Stabilized Blue Phase Liquid Crystals.....	10
1.1.1 Material Preparation.....	10
1.1.2 Electric Field Effects.....	11
1.1.3 Temperature Effects .....	12
1.1.4 Wavelength Effects .....	13
1.2 Liquid Crystal Displays (LCDs) .....	14
1.3 Polymer-Stabilized Blue-Phase Liquid Crystal Displays.....	16
CHAPTER 2: FREQUENCY EFFECTS OF BPLCS .....	19
2.1 Experiment .....	19
2.2 Theory and Results.....	20
2.3 Summary .....	26
CHAPTER 3: NEGATIVE KERR CONSTANT .....	27
3.1 Material Preparations .....	27



3.2	Electro-optical Properties .....	28
3.3	Summary .....	33
CHAPTER 4: HIGH-EFFICIENCY TRANSMISSIVE BPLCDS .....		34
4.1	Enhanced Protrusion Electrode Structure .....	34
4.1.1	Device Configuration .....	34
4.1.2	Simulation Results .....	36
4.2	Complementary Enhanced Protrusion Electrode Structure .....	37
4.2.1	Device Configuration .....	38
4.2.2	Simulation Results .....	39
CHAPTER 5: HIGH-EFFICIENCY TRANSFLECTIVE BPLCDS .....		41
5.1	A Transflective BPLCD Based on Protrusion Electrodes .....	42
5.1.1	Device Configuration .....	42
5.1.2	Simulation Results .....	44
5.1.3	Conclusion .....	48
5.2	A Transflective BPLCD Based on Enhanced Protrusion Electrodes .....	49
5.2.1	Device Configuration .....	49
5.2.2	Simulation Results .....	50
5.2.3	Conclusion .....	53
5.3	Summary .....	53
CHAPTER 6: HIGH-EFFICIENCY 3D DISPLAYS BASED ON BPLCS .....		54
6.1	Introduction to 3D Displays .....	54

6.1.1	Head Mounted 3D Displays .....	54
6.1.2	Anaglyph.....	55
6.1.3	Polarizing Glasses.....	56
6.1.4	Shutter Glasses.....	58
6.1.5	Autostereoscopy.....	59
6.1.6	Summary .....	61
6.2	Integral Imaging 3D Displays .....	62
6.3	BPLC Adaptive Lenses .....	65
6.3.1	BPLC Adaptive Lens with A Curved ITO Electrode .....	66
6.3.2	BPLC Adaptive Lens with Multiple Electrodes.....	76
6.3.3	BPLC Adaptive Lens with A Resistive Electrode.....	80
6.4	Summary .....	90
CHAPTER 7: SUMMARY.....		91
APPENDIX.....		<b>Error! Bookmark not defined.</b>
LIST OF REFERENCES .....		96

## LIST OF FIGURES

Fig. 1.1 Schematic representation of the phases of liquid crystal molecules. ....	1
Fig. 1.2 Chiral nematic phase, $p$ —pitch length. ....	3
Fig. 1.3 Schematic picture of the temperature region near the chiral nematic (CH)-isotropic (ISO) phase transition. ....	4
Fig. 1.4 Director field of a double-twist cylinder (Fig. from [4]). ....	5
Fig. 1.5 (a) Arrangement of double-twist cylinders of BPI in a unit cell; (b) three-dimensional arrangement of BP I; (c) arrangement of double-twist cylinders of BPII in a unit cell; (d) three-dimensional arrangement of BP II. (Figures from [5]). ....	6
Fig. 1.6 The frustration and disclination of BPI. ....	7
Fig. 1.7 Temperature dependence of Bragg reflections (Fig. from [9]). ....	8
Fig. 1.8 Platelet textures observed with a polarized optical microscope (POM) and Bragg reflection peaks for various chiral dopant concentrations. The upper optical images were obtained using a POM under reflection mode. Each Bragg reflection spectrum corresponds to the platelet texture above. (Fig. from [9]). ....	9
Fig. 1.9 Material preparation process of polymer-stabilized blue phase. ....	11
Fig. 1.10 Working principle of a twist-nematic LCD. ....	15
Fig. 1.11 Working principle of a BPLCD using IPS electrode structure. ....	17
Fig. 1.12 Working principle of a BPLCD using protruded IPS electrode structure. ....	18
Fig. 2.1 Experimental setup for measuring the VT curves of BPLCs. ....	20
Fig. 2.2 Measured VT curves of Cell 1 at different frequencies. ....	20
Fig. 2.3 Kerr constant and $\Delta\varepsilon$ versus frequency for BPLC in Cell 1. Black open circles are $\Delta\varepsilon$ ,	

green filled circles are Kerr constant obtained from VT curves, and pink solid line is the fitting of Kerr constant using Eq. (2-3) with $K_{\infty}=-0.189 \text{ nm/V}^2$ , $f_r=118 \text{ kHz}$ , and $\alpha=0.12$ .....	21
Fig. 2.4 Measured VT curves of Cell 2 at different frequencies.....	24
Fig. 2.5 Kerr constant versus frequency for the BPLC in Cell 2. Squares are Kerr constant obtained from VT curves, and solid line is the fitting of Kerr constant Eq.(2-3) with $K_{\infty}=0$ , $f_r=1280 \text{ Hz}$ , and $\alpha=0.13$ . ....	25
Fig. 2.6 Temperature increase of sample I and II at different frequencies.....	26
Fig. 3.1 (a) Microscopic image of Cell 1 under crossed polarizers at off state, (b) at $44 \text{ V}_{\text{rms}}$ , and (c) at $60 \text{ V}_{\text{rms}}$ ; (d) Experimental setup for measuring the electro-optical properties of the VFS cells. ....	29
Fig. 3.2 Measured VT curves of Cell 2 and Cell 3 using the experimental setup in Fig. 3.1(d) with a QW plate in front the VFS cells.....	31
Fig. 3.3 Measured VT curve of Cell 2 using the experimental setup in Fig. 3.1(d) without a QW plate in front the VFS cell.....	32
Fig. 4.1 (a) Side view of a conventional protrusion electrode structure, and (b) with enhanced protrusion electrode structure. ....	35
Fig. 4.2 VT curves of IPS electrode (red), conventional protrusion structures (blue and magenta) and new protrusion structures (black and green). ....	37
Fig. 4.3 Side-view of the complementary enhanced protrusion electrode structure.....	38
Fig. 4.4 VT curves for the proposed complementary enhanced protrusion electrode structure with different dimensions.....	39
Fig. 5.1 Device structure of the TR PS-BP LCD based on protrusion electrodes, P stands for pixel	

electrode and C for common electrode. ....	43
Fig. 5.2 Simulated VT and VR curves for the proposed TR BPLCD using protrusion electrodes. The red (solid) and black (dashed) lines represent simulated VT and VR curves, and the closed and open squares represent normalized transmittance and reflectance. ....	45
Fig. 5.3 Isocontrast contour plots for (a) T mode and (b) R mode of the proposed TR-LCD using protrusion electrodes. ....	47
Fig. 5.4 Device configuration of the TR BPLCD based on enhanced protrusion electrodes. ....	50
Fig. 5.5 VT and VR curves for the TR BPLCD using enhanced protrusion electrodes. The red and black lines represent simulated VT and VR curves, and the red dots and black dots represent normalized transmittance and reflectance. ....	51
Fig. 5.6 Isocontrast plots of the TR BPLCD based on enhanced protrusion electrodes: (a) T region and (b) R region. ....	52
Fig. 6.1 Working principle of head mounted 3D displays. ....	55
Fig. 6.2 Working principle of anaglyph 3D displays. ....	56
Fig. 6.3 Working principle of 3D displays based on two projectors and polarizing glasses. ....	57
Fig. 6.4 Working principle of 3D displays based on patterned retarders and polarizing glasses. ....	58
Fig. 6.5 Working principle of 3D displays based on shutter glasses. ....	59
Fig. 6.6 Working principle of autostereoscopic displays based on parallax barrier. ....	60
Fig. 6.7 Working principle of autostereoscopic displays based on lenticular lens array. ....	61
Fig. 6.8 The process of pickup. ....	62
Fig. 6.9 The process of image reconstruction (a) pseudoscopic image (b) orthoscopic image ....	63
Fig. 6.10 Side-view of the BPLC adaptive lens with a curved ITO electrode. ....	67

Fig. 6.11 Simulated phase profiles across the lens at $V=100 V_{\text{rms}}$ for $o$ - and $e$ - waves in the proposed microlens array (red and blue) and hole-patterned microlens array (green and black).....	70
Fig. 6.12 Effect of top substrate shape on the generated phase profile. (a), (b) and (c) are structures with different top ITO shapes. (d) The simulated phase profiles: black line for structure (a), green for structure (b), red line for structure (c), and blue dashed lines for an ideal parabolic shape. ....	73
Fig. 6.13 Simulated voltage dependent focal length of the proposed BPLC microlens. ....	75
Fig. 6.14 Device configuration of the BPLC adaptive lens with multiple electrodes. ....	76
Fig. 6.15 Phase profile of the BPLC adaptive lens with multiple electrodes when $V_1=65 V_{\text{rms}}$ , $V_2=38.2 V_{\text{rms}}$ , $V_3=22.3 V_{\text{rms}}$ , $V_4=11 V_{\text{rms}}$ , $V_5=1.05 V_{\text{rms}}$ and the bottom electrode is grounded. Blue— $o$ - wave, red— $e$ - wave and black—ideal parabolic shape. ....	78
Fig. 6.16 Focal length of the proposed BPLC lens at different voltages. ....	80
Fig. 6.17 Side view of the proposed cylindrical BPLC lens. ....	81
Fig. 6.18 Simulated phase profiles ( $\lambda=550 \text{ nm}$ ) across the lens for $o$ - wave (dotted lines) and $e$ - wave (solid curves) at $V_0=50 V_{\text{rms}}$ . The upper curve is for $d=25 \mu\text{m}$ lens and the lower one is for $d=8 \mu\text{m}$ . ....	84
Fig. 6.19 Simulated phase profiles ( $\lambda=550 \text{ nm}$ ) across the lens with a $13 \mu\text{m}$ cell gap at $30 V_{\text{rms}}$ and $50 V_{\text{rms}}$ . Red dotted curves are for $o$ - wave and black solid curves are for $e$ - wave, and green dashed curves are ideal parabolic curves. ....	87
Fig. 6.20 Electric field distribution across the BPLC cylindrical lens with $13 \mu\text{m}$ cell gap at $50 V_{\text{rms}}$ , (a) for $E_x$ , and (b) for $E_z$ . ....	88
Fig. 6.21 Simulated voltage dependent focal length of the proposed BPLC lens: black dotted	

curve is for  $o$ - wave, and red solid curve is for  $e$ - wave. .... 89

# CHAPTER 1: INTRODUCTION

## 1.1 Liquid Crystals

Liquid crystal was first discovered by Austrian botanist and chemist Friedrich Reinitzer and German physicist Otto Lehmann in 1988. As shown in Fig. 1.1, liquid crystal is a mesophase between isotropic liquid phase and solid crystalline phase [1]. If the temperature is too high, thermal motion will destroy the delicate cooperative ordering of the LC phase, and transit the material into an isotropic liquid phase. The transition temperature between liquid crystal phase and isotropic phase is called clearing temperature  $T_c$ . At too low temperature, most LC materials will transit to conventional crystal solids.

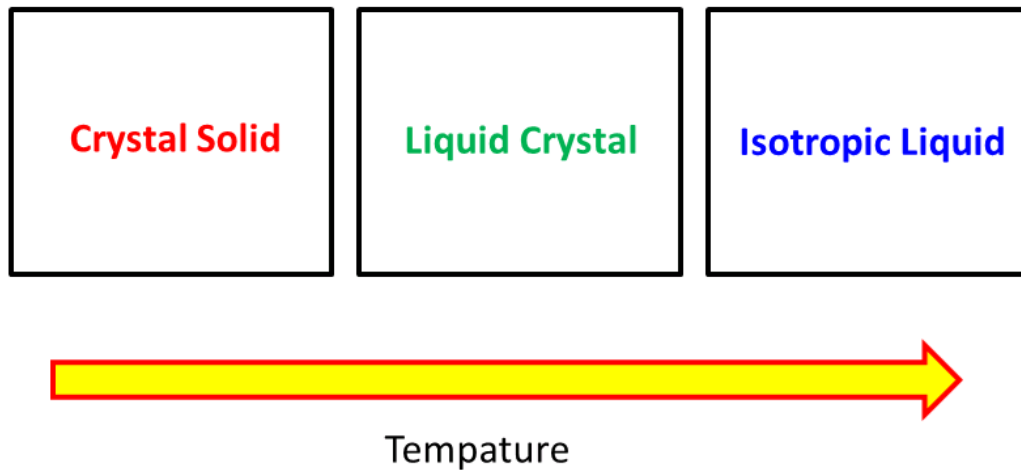


Fig. 1.1 Schematic representation of the phases of liquid crystal molecules.

### 1.1.1 Nematic Phases

Nematic phase is the most common liquid crystal phase. Nematic liquid crystals have the properties between liquids and solid crystals. The molecules in an isotropic state have neither



orientation order nor position order, so they could flow freely and appears optically isotropic. At crystalline phase, molecules have both orders. Therefore they exhibit optical birefringence while having the fixed positions in the crystalline structure. However, at nematic liquid crystal phase, molecules have the orientation order but no position order. So they could flow like liquid, and that's how they got the "liquid" part of name. On the other hand, they exhibit an optical birefringence like crystalline solids, and that's how they got the "crystal" part of name. Moreover, the orientation of the molecules can be aligned in certain directions using surface alignment technology, and can be changed by electric field or magnetic field. Nematic liquid crystals have been widely used for display and photonic applications because of their attractive properties, such as simple molecular alignment, low voltage, natural gray scale, and low power consumption.

### **1.1.2 Chiral Phases**

Chiral nematic phase exhibits chirality (handedness). Not only chiral molecules (i.e., those have no internal planes of symmetry) can give rise to such a phase, achiral liquid crystals mixed with chiral agents can also form chiral nematic phase. In such a phase, molecules twist perpendicular to the director, with the molecular axis parallel to the director as shown in Fig. 1.2. Molecules have position order in a layered structure, with a finite angle with respect to the layer normal.

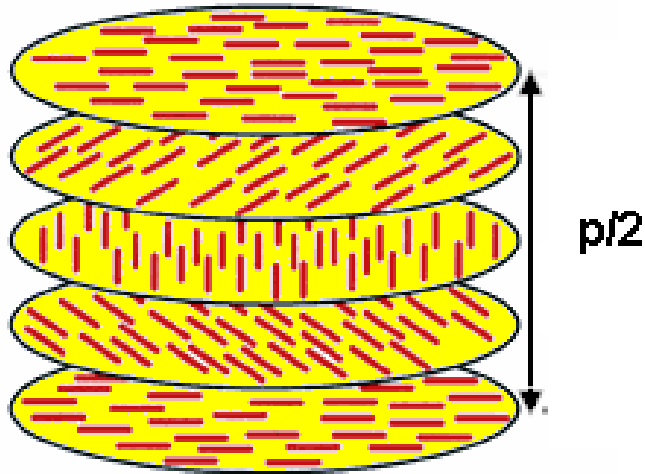


Fig. 1.2 Chiral nematic phase,  $p$ —pitch length.

The chiral pitch,  $p$ , is the distance over which the LC molecules undergo a full  $360^\circ$  twist. Since in this phase the LC directors at  $0^\circ$  and  $\pm 180^\circ$  are equivalent, every  $p/2$  distance, the orientation of liquid crystal repeats. Due to the one dimensional periodicity of structure, Bragg reflection occurs with high angular dependency. The center reflective wavelength  $\lambda_o$  is determined by the pitch length and refractive indices of the liquid crystal as:

$$\lambda_o = \frac{n_o + n_e}{2} p \quad (1-1)$$

where  $n_o$  is the ordinary refractive index and  $n_e$  the extraordinary refractive index of the liquid crystal, respectively. This phase also exhibits a unique property that they reflect circularly polarized light when light is incident along the helical axis.

### 1.1.3 Blue Phases

Blue phase is a state between isotropic and chiral nematic phases, which exists within a very narrow temperature range (1~2K) for certain liquid crystals with short helical pitch [2-4]. Though discovered as the first liquid crystal in history, blue phase was not identified to a new thermodynamically stable phase until mid-1970s.

So far, three types of lattice structures have been found: BPI, BPII, and BPIII. Fig. 1.3 shows the schematic picture of the temperature region near the chiral nematic (CH)-isotropic (ISO) phase transition [5].

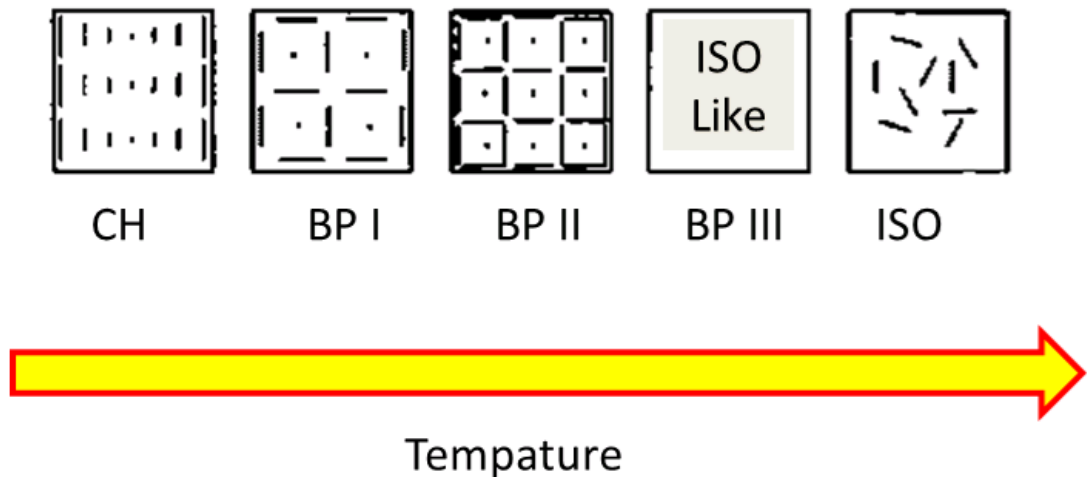


Fig. 1.3 Schematic picture of the temperature region near the chiral nematic (CH)-isotropic (ISO) phase transition.

In a blue phase system, the lowest energy director configuration is a double twist cylinder in which the directors rotate spatially about any radius of a cylinder in Fig. 1.4 [4,6].



Fig. 1.4 Director field of a double-twist cylinder (Fig. from [4]).

Such double-twist cylinders are further arranged in three directions perpendicular to each other, and form a lattice structure. The three dimensional lattice structures for BPI (body centered cubic) and BPII (simple cubic) are shown in Fig. 1.5. BPI and BPII are cubic; BP III has the same symmetry as the ISO phase.

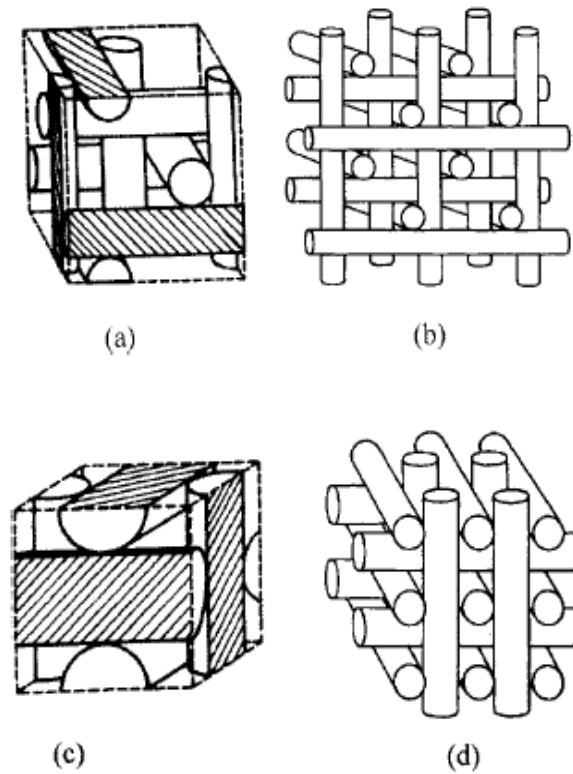


Fig. 1.5 (a) Arrangement of double-twist cylinders of BPI in a unit cell; (b) three-dimensional arrangement of BP I; (c) arrangement of double-twist cylinders of BPII in a unit cell; (d) three-dimensional arrangement of BP II. (Figures from [5]).

For the cubic structures, according to Landau theory, a tube of double-twist cylinder is only stable near the axis. If the local twist becomes as much as  $90^\circ$ , substantial bend distortion occurs and the energy advantage is lost. So the twist is limited to  $45^\circ$ . Therefore, in the intersections between double-twist cylinders, there would have incompatible directors, which in turn leads to frustration and disclinations. Disclinations are topological line singularities in liquid crystal directors as shown Fig. 1.6. Disclinations occur at the points where the cylinders are in contact.

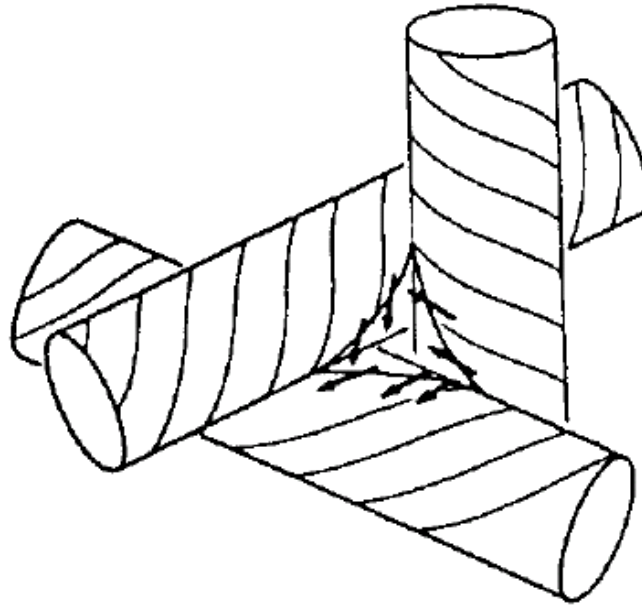


Fig. 1.6 The frustration and disclination of BPI.

As a result, blue phase state is a delicately balanced system of the crystalline and disclinations, which only exist within a very narrow temperature range.

Because of the periodical cubic structures of BPI and BPII, Bragg reflection occurs for wavelength that is close to the lattice dimension. The reflection wavelength of blue phase can be calculated as [7]:

$$\lambda = \frac{2na}{\sqrt{h^2 + k^2 + l^2}}, \quad (1-2)$$

where  $n$  and  $a$  denote average refractive index and lattice constant of blue phases, and  $h$ ,  $k$ , and  $l$  are the Miller indices. In BPI, the lattice constant is the same as one helical pitch length and diffraction peaks appear when  $h + k + l$  is an even number, such as (110), (200), and (211). In BPII, the lattice constant corresponds to half a pitch length and diffraction peaks appear with no

limitation on  $h + k + l$  [8]. Fig. 1.7 shows the reflection spectrum of a certain blue phase liquid crystal at different temperatures and Fig. 1.8 shows the textures of blue phase liquid crystal under polarized optical microscope with different pitch lengths (chiral concentration) [9].

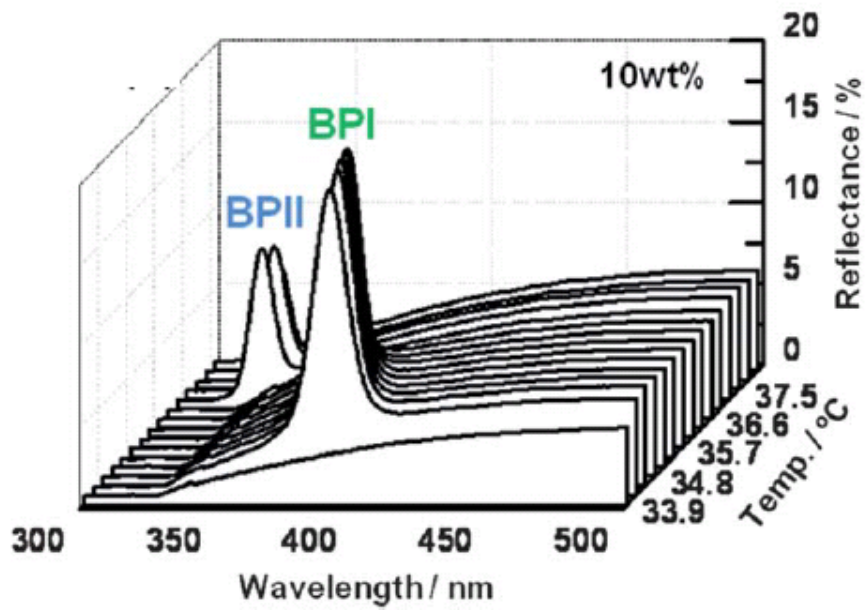


Fig. 1.7 Temperature dependence of Bragg reflections (Fig. from [9]).

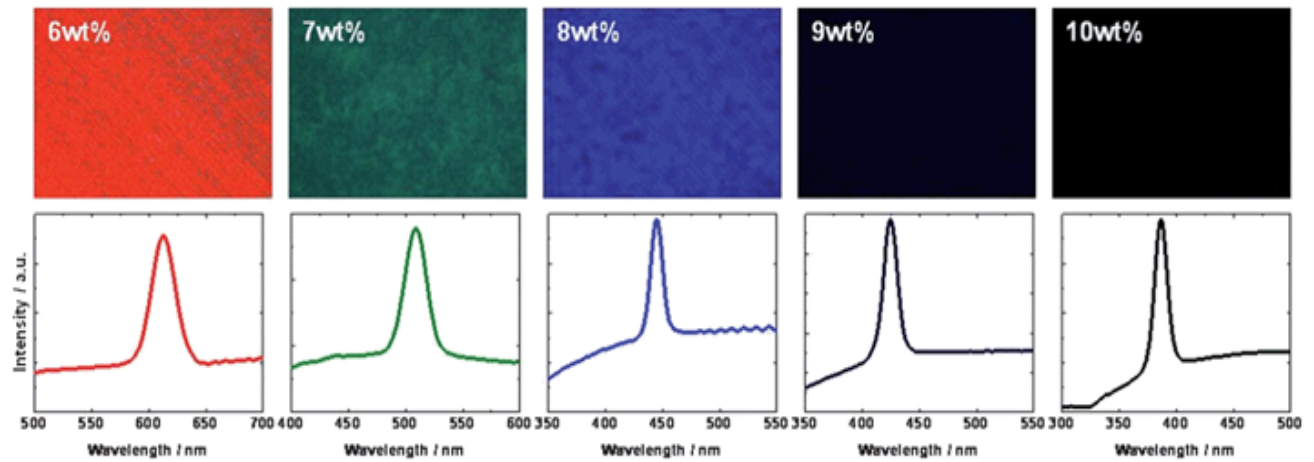


Fig. 1.8 Platelet textures observed with a polarized optical microscope (POM) and Bragg reflection peaks for various chiral dopant concentrations. The upper optical images were obtained using a POM under reflection mode. Each Bragg reflection spectrum corresponds to the platelet texture above. (Fig. from [9]).

For a wavelength much larger than the lattice dimension, because the cylinders are orientated in various directions, macroscopically blue phase appears optically isotropic.

When electric fields are applied to a blue phase liquid crystal, several effects can occur depending on the strength of  $E$  field [5]: local reorientation of the molecules, distortion of the lattice (electrostriction), and phase transition to lower symmetry phases. When  $E$  field is low, there is mainly local director reorientation within the cubic cell of the blue phase. The refractive index is elongated in the direction of  $E$  field, and shrinks in orthogonal directions. This  $E$  field induced birefringence is proportional to the square of  $E$  field. The local reorientation has a very fast response time at sub-millisecond level due. As  $E$  field increases, electrostriction process starts to occur and response time dramatically increases ( $\sim 10$ s). At an even higher  $E$  field, blue phase structure would be destructed and the phase transits into cholesteric phase.



## **1.1 Polymer Stabilized Blue Phase Liquid Crystals**

Although blue phase liquid crystals have much faster response time than nematics, in the past four decades they have been studied mainly for scientific interest due to the narrow temperature range. Through the years, a lot of efforts have been made to widen the temperature range of blue phases. In 2005, Coles et al created a new molecular structure with a rigid biphenyl core in both ends and a flexible alkyl chain in the middle, and obtained a wider temperature range from 16.5°C to 57.7°C [10]. But the dipole of this type of molecule is small and a high electric field is needed. Other approaches such as doping blue phase with gold nanoparticles [11] and surface-functionalized CdSe nanoparticles [12] have also obtained a wider temperature range. So far, the most promising approach to widen the blue phase temperature range is the polymer stabilization proposed by Kikuchi et al. in 2002 [13]. It is considered that the cross-linked polymer network is selectively concentrated in the disclination lines to stabilize the lattice structure of blue phases. As a result, the temperature range of BPLC has been extended to more than 60K, including room temperature (260-326K). Moreover, the polymer-stabilized blue phase maintains fast electro-optic switching property as pure blue phase liquid crystal. Therefore, the applications of blue phase liquid crystals have become possible and popular, such as BPLC displays, gratings, lenses and other photonic devices.

### **1.1.1 Material Preparation**

To make a polymer-stabilized blue phase liquid crystal, firstly, we need a blue phase mixture which usually consists of a nematic liquid crystal and certain percent of chiral dopant.

Secondly, a small fraction of monomers usually consisting of a mono-functional monomer and a di-functional monomer are added to the blue phase system. Finally, a very small fraction of photo initiator is added. Then we select a blue phase (I or II) and expose the sample with UV light for a certain dosage. After UV irradiation, monomers are polymerized to form polymer network which stabilizes the blue phase lattice structures. Fig. 1.9 shows the preparation process of polymer-stabilized blue phase.



Fig. 1.9 Material preparation process of polymer-stabilized blue phase.

### 1.1.2 Electric Field Effects

The electric field effects on polymer-stabilized blue phase are similar to that of pure BP. When a weak electric field is applied, liquid crystal molecules tend to align parallel with the electric field when the dielectric anisotropy  $\Delta\epsilon > 0$  (or perpendicular to the electric field if  $\Delta\epsilon < 0$ ). Macroscopically, birefringence is induced along the direction of electric field which follows Kerr effect as [14]:

$$\Delta n_{ind} = n_e(E) - n_o(E) = K\lambda E^2, \quad (1-3)$$

where  $\lambda$  is the wavelength of incident light and  $K$  is the Kerr constant. A higher electric field

could lead to lattice distortion (electrostriction effect). For a sufficiently high electric field, blue phase may transform to new phases, to chiral nematic phases, and ultimately to nematic phases [15,16]. The polymer network restricts the lattice structure so that phase transition will not easily occur, but lattice distortion cannot be avoided completely.

As we measured the induced refractive index versus voltage of a polymer stabilized blue phase, we have found that Kerr effect is only valid in the low field region [17]. As electric field further increases, induced birefringence gradually saturates. To better describe the saturation phenomenon, extended Kerr model was proposed [17] as following:

$$\Delta n_{ind} = \Delta n_s [1 - \exp(-\frac{E^2}{E_s^2})] , \quad (1-4)$$

where  $\Delta n_s$  is the saturated induced birefringence and  $E_s$  the saturation field. In the low field region ( $E \rightarrow 0$ ), it is reduced to Kerr effect, and the Kerr constant, as the slope in the low field region, now can be related to  $\Delta n_s$  and  $E_s$  :

$$K = \Delta n_s / \lambda E_s^2 . \quad (1-5)$$

Roughly speaking,  $\Delta n_s$  governs the optical property and  $E_s$  determines the electric property.

### 1.1.3 Temperature Effects

Although polymer network has significantly widened the temperature range of blue phase liquid crystal, the physical properties of a polymer-stabilized blue phase remain highly temperature dependent.

According to Gerber's theory [18], Kerr constant can be approximated by:

$$K \approx \Delta n \Delta \varepsilon \frac{p^2}{k \lambda (2\pi)^2} \quad (1-6)$$

where  $\Delta n$  is the birefringence,  $\Delta \varepsilon$  the dielectric anisotropy, and  $k$  the elastic constant of the host LC, respectively, and  $p$  is the pitch length.

For the host liquid crystal, we have:

$$\Delta n \sim \Delta n_o S, \quad (1-7)$$

$$\Delta \varepsilon \sim S/T, \quad (1-8)$$

$$\text{and } k \sim S^2, \quad (1-9)$$

where  $T$  is Kelvin temperature and  $S$  is the order parameter.

By combining Eqs. (1-6), (1-7), (1-8) and (1-9), the temperature dependent Kerr constant has following simple form [19]:

$$K \propto \frac{1}{T} - \frac{1}{T_c}, \quad (1-10)$$

where  $T_c$  is the clearing temperature of the LC. Therefore, Kerr constant decreases as the temperature increases and gradually vanishes as the temperature approaches  $T_c$ .

#### 1.1.4 Wavelength Effects

From Eq. (1-6), one should know that Kerr constant of polymer-stabilized blue phase is wavelength dependent, because  $\Delta n$  is. According to birefringence dispersion model [20]:

$$\Delta n = G \frac{\lambda^2 \lambda^{*2}}{\lambda^2 - \lambda^{*2}}, \quad (1-11)$$

where  $\lambda^*$  is the resonant wavelength of the LC composite and  $G$  is a proportionality constant.

According to Eq. (1-6), Kerr constant should have a relation with wavelength as:

$$K = G_K \frac{\lambda \lambda^{*2}}{\lambda^2 - \lambda^{*2}}, \quad (1-12)$$

where  $G_k$  is a proportionality constant.

## 1.2 Liquid Crystal Displays (LCDs)

The most common application of liquid crystals in our daily life is display, ranging from cell phones, portable video players, car navigators, notebook computers, desktop monitors, TVs, and data projectors. A LCD panel consists of a two-dimensional array of pixels. Each pixel can be driven independently by a thin film transistor (TFT). The liquid crystal (LC) cell is sandwiched between two crossed polarizers. The working principle of a twist-nematic (TN) LCD is shown as an example in Fig. 1.10. At voltage-off state, the LC directors are twisted  $90^\circ$  from the top to the bottom substrates. After passing through the polarizer, the linearly polarized light follows the twist of liquid crystal so that its polarization is rotated by  $90^\circ$ . Therefore, it could pass through the crossed analyzer, and a bright state is obtained. When a high voltage is applied between the indium tin oxide (ITO) electrodes on the inner side of two glass substrates, the LC directors tilt perpendicular to the substrates. As a result, the polarization state of the incident light is not changed by the LC cell, and the light is absorbed by the analyzer. This is the so-called

normally white mode. As the applied voltage varies, the LC directors are tilted at different angles, leading to different transmission (gray levels). In addition to TN, two other normally black modes are commonly used in display devices; they are in-plane-switching (IPS) and vertical alignment (VA).

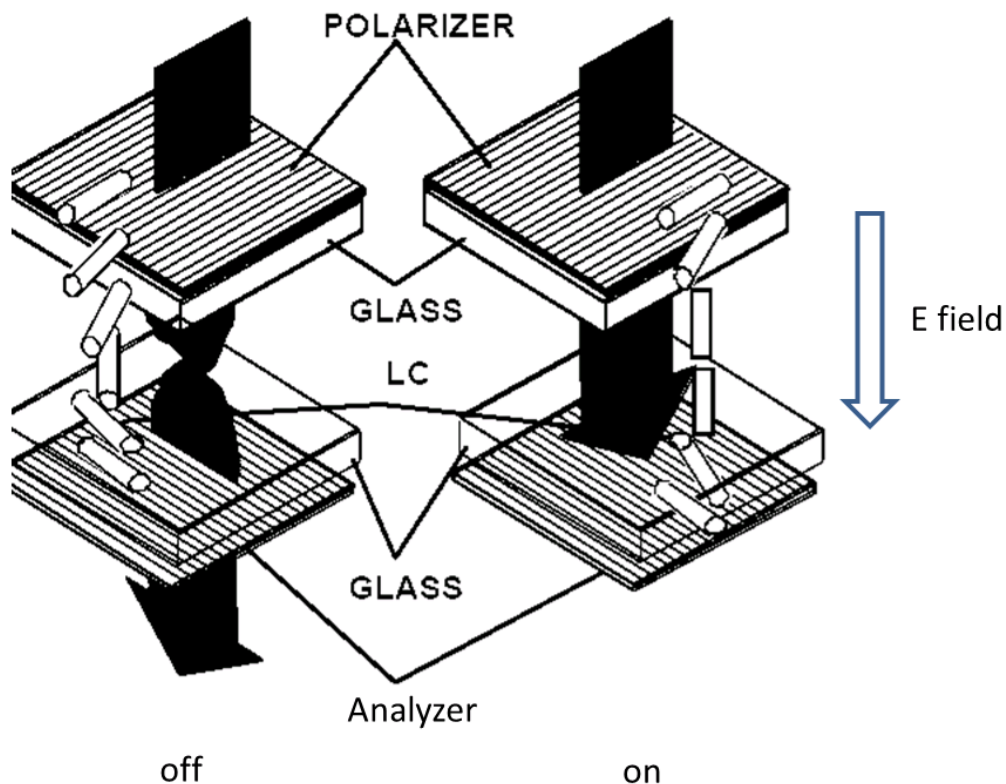


Fig. 1.10 Working principle of a twist-nematic LCD.

For conventional LCDs, color filters are fabricated on top of each pixel. By combining red (R), green (G) and blue (B) color filters with varied transmittance in each pixel, a full-color display can be obtained [21]. However, each color filter only allows less than 1/3 of the backlight to pass through, which dramatically decreases the optical efficiency of a LCD.

There is another kind of LCD---color sequential display, which does not use color filters.

In such a display, the RGB LED backlights are turned-on alternatively to form red, green, and blue frames in time sequence. The observer's eye will integrate the RGB frames to form a full color image. By eliminating the pigment color filters, both optical efficiency and resolution density are tripled. However, color breakup would occur at the edge of objects if the response is not fast enough.

### **1.3 Polymer-Stabilized Blue-Phase Liquid Crystal Displays**

Polymer-stabilized blue phase is promising for next-generation display because it exhibits following attractive features: optically isotropic dark state, no need for surface alignment layer, and submillisecond gray-to-gray response time [22]. Especially the fast response time would enable color sequential display as we mentioned in previous section, and realize high optical efficiency from the panel point of view.

The most commonly used electrode design for BPLCDs is IPS structure [23] as shown in Fig. 1.11. The pixel electrode (red) and common electrode (blue), usually several tens of nanometers thick, are coated on the bottom substrate. When no voltage is applied, BPLC is optically isotropic, therefore, a dark state is achieved under crossed polarizers. When a voltage is applied, the refractive index is elongated in the direction of electric field, following extended Kerr model [17]. Phase retardation is induced in the gap between pixel and common electrodes, and a bright transmittance is obtained in these regions. However, on top of the electrodes, because the electric fields are vertical, although birefringence is still induced in the vertical

direction, there is no optical phase retardation for normal incident light. These regions have almost no transmittance and are called dead zones.

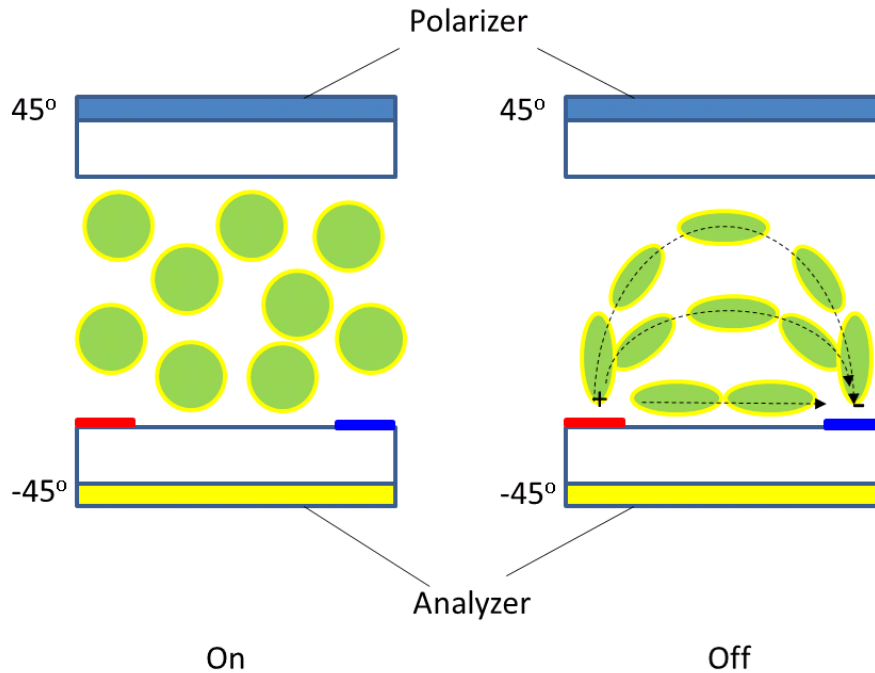


Fig. 1.11 Working principle of a BPLCD using IPS electrode structure.

In order to reduce dead zones for improving transmittance, the width of electrodes  $w$  should be small compared to the gap between electrodes  $l$ . The gap, however, could not be too large, because the operating voltage would increase as  $l$  increases. Moreover, due to the thin thickness of electrode, only the BPLCs near bottom substrate would be effectively utilized for accumulating phase retardation, while above certain depth, BPLCs do not contribute to transmittance. Therefore, in such a structure, when the cell gap is larger than the penetration depth of the electric field, it is cell gap insensitive.

For an IPS structure with  $w=10\ \mu\text{m}$  and  $l=10\ \mu\text{m}$ , using a large Kerr constant BPLC [24], the operating voltage is  $\sim 50\ \text{V}_{\text{rms}}$  and the transmittance of the cell is  $\sim 50\%$ .



Recently, a protruded IPS electrode structure was proposed to decrease the operating voltage [25]. With the increase of the electrode thickness (~several microns), strong and uniform electric fields are generated between pixel and common electrodes. Moreover, the electric field penetrates deeply into the LC bulk region, utilizing more BPLCs to contribute to transmittance. As a result, voltage is greatly reduced. For a structure with a protrusion bottom width  $w=2\ \mu\text{m}$ , top width  $w_2=1\ \mu\text{m}$ , height  $h=2\ \mu\text{m}$ , gap between electrode bottom  $l=4\ \mu\text{m}$ , a peak transmittance ~75% is achieved at  $17\ \text{V}_{\text{rms}}$ . As the gap further decreases to  $l=2\ \mu\text{m}$ , a lower operating voltage (~10  $\text{V}_{\text{rms}}$ ) is achieved, but the transmittance is also decreased to 63% due to smaller ratio of  $l/w$ . Although the protrusion structure could dramatically lower the operating voltage, it could hardly enhance the transmittance because the dead zones on top of the electrodes still exist. Therefore, how to enhance the optical efficiency of BPLCDs is an urgent technical challenge.

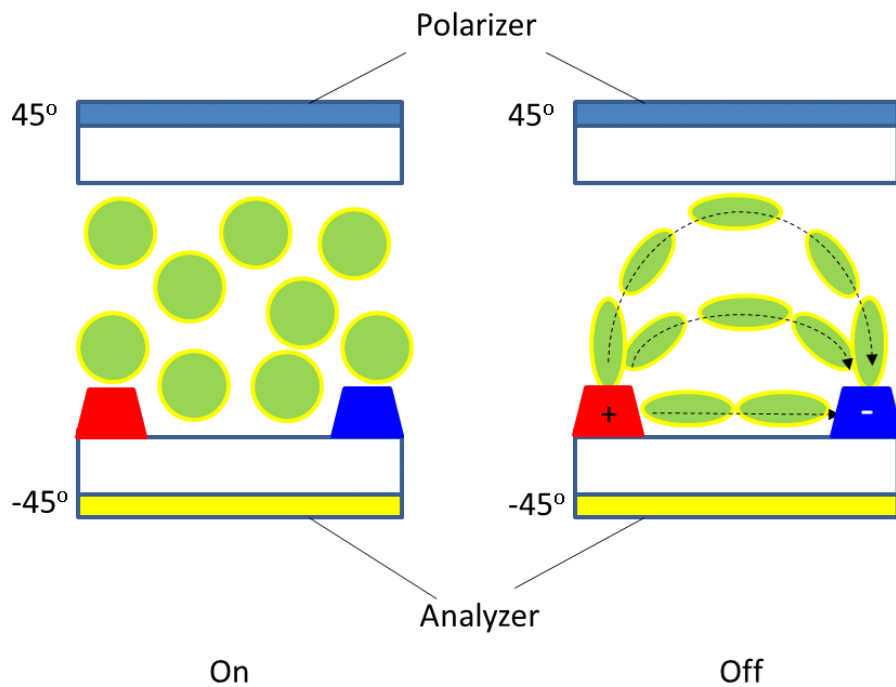


Fig. 1.12 Working principle of a BPLCD using protruded IPS electrode structure.

## CHAPTER 2: FREQUENCY EFFECTS OF BPLCS

Due to the fast response of BPLCs, color sequential display would be enabled with optical efficiency and resolution density tripled. However, the operating electric field frequency is also tripled since 3 RGB sub-frames replace one color frame. Therefore, there is a need to study the frequency effects on BPLCs [26].

### 2.1 Experiment

In our experiment, we prepared two IPS cells whose electrode width and electrode gap are both 10  $\mu\text{m}$ , and cell gap is 7.5  $\mu\text{m}$ . Cell 1 was filled with a BPLC mixture consisting of 76.2 wt% JM2069-043 nematic LC host (from ITRI), 13 wt% chiral dopants [8% ISO-(6OBA)<sub>2</sub> and 5% CB15 (Merck)], 10 wt% monomers [6% RM257 (Merck) and 4% TMPTA (1,1,1-Trimethylolpropane Triacrylate, Sigma Aldrich)], and ~0.8 wt% photoinitiator. The cell was cooled to BPI phase and the precursor was cured by a UV light with  $\lambda \sim 365$  nm and intensity  $\sim 2$  mW/cm<sup>2</sup> for 30 minutes. After UV curing, the polymer-stabilized BPLC composite was self-assembled, and the clearing temperature was measured to be  $T_c \sim 44$  °C. The relatively low  $T_c$  is attributed to the low melting point ( $\sim 4$  °C) of the chiral dopant CB-15. Cell 2 was filled with Chisso JC-BP01M precursor, in which chiral dopant and monomers were premixed. Then it was exposed by the same UV lamp with an intensity  $\sim 20$  mW/cm<sup>2</sup> for 1 minute. The  $T_c$  of sample 2 is  $\sim 70$  °C.

Next, we measured the voltage-dependent transmittance (VT) curves of these two cells using a He-Ne laser ( $\lambda = 633$  nm). The experimental setup is shown in Fig. 2.1. The cells were

placed in a temperature controller to have a constant temperature ( $\sim 22^\circ\text{C}$ ).

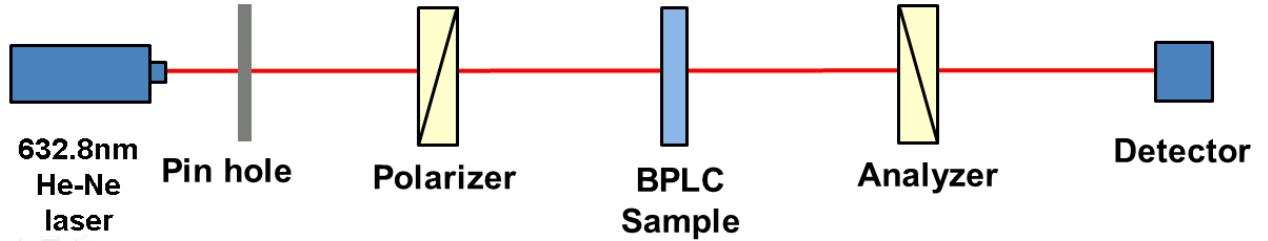


Fig. 2.1 Experimental setup for measuring the VT curves of BPLCs.

## 2.2 Theory and Results

Fig. 2.2 shows the normalized VT curves of Cell 1 at five frequencies: 100, 1k, 10k, 50k and 100k Hz. As frequency increases, the VT curve shifts rightward, indicating that the on-state voltage ( $V_{on}$ ) increases (i.e., Kerr constant decreases) with frequency.

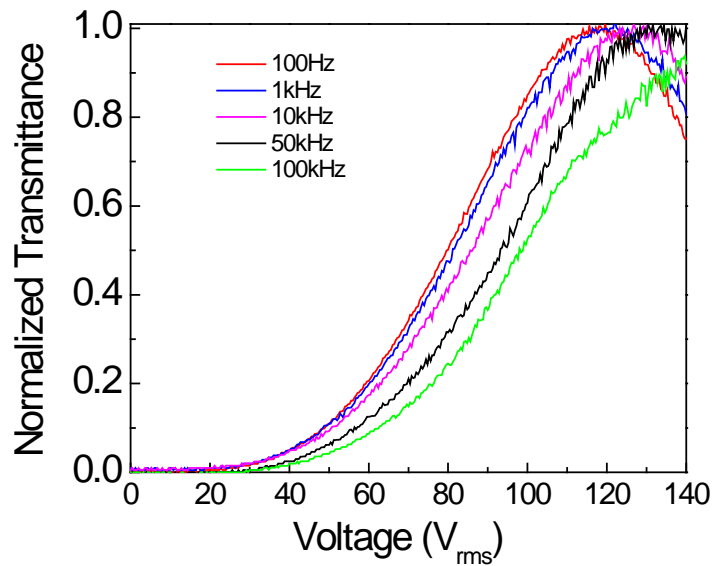


Fig. 2.2 Measured VT curves of Cell 1 at different frequencies.

We fitted the VT curves with extended Kerr model [17] at each frequency. In our experiment, we used the same probing wavelength but changed the electric field frequency. Thus during fittings we kept  $\Delta n_s=0.19$  and only changed  $E_s$  for different frequencies. Once  $\Delta n_s$  and  $E_s$  are obtained, we then calculate Kerr constant  $K=\Delta n_s/(\lambda E_s^2)$  thru extended Kerr model. In Fig. 2.3, we plot the obtained frequency dependent Kerr constant (green closed circles) at logarithmic scale. On the theory side, Gerber found that Kerr constant is proportional to  $\Delta n$ ,  $\Delta \epsilon$ , the square of pitch length  $p$ , and the reciprocal of the elastic constant  $k$  of the host LC as shown in Eq. (1-6). Among all the parameters, only  $\Delta \epsilon$  is related to the electric field frequency. Therefore, Kerr constant and  $\Delta \epsilon$  should have the same frequency dependency.

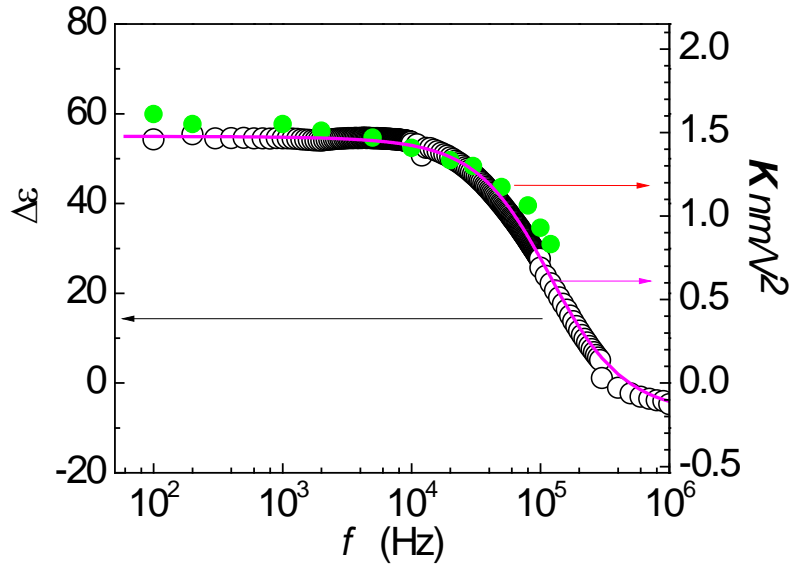


Fig. 2.3 Kerr constant and  $\Delta \epsilon$  versus frequency for BPLC in Cell 1. Black open circles are  $\Delta \epsilon$ , green filled circles are Kerr constant obtained from VT curves, and pink solid line is the fitting of Kerr constant using Eq. (2-3) with  $K_\infty=-0.189 \text{ nm/V}^2$ ,

$$f_r=118 \text{ kHz, and } \alpha=0.12.$$

To prove this, we also include the measured dielectric anisotropy of host LC (black open circles) in Fig. 2.3, but using a different scale. As expected, the frequency dependent  $K$  and  $\Delta\epsilon$  curves overlap quite well, indicating that  $K$  is indeed proportional to  $\Delta\epsilon$  as Eq. (1-6) predicts.

For a LC mixture, the frequency dependent dielectric constants  $\epsilon_{//}$  and  $\epsilon_{\perp}$  can be described by the following Cole-Cole equation [27]:

$$\epsilon^*(f) = \epsilon_{\infty} + \frac{\epsilon_s - \epsilon_{\infty}}{1 + (i \frac{f}{f_r})^{1-\alpha}}, \quad (2-1)$$

where  $\epsilon^* = \epsilon' + i\epsilon''$  is the complex dielectric constant at frequency  $f$ ,  $\epsilon_s$  and  $\epsilon_{\infty}$  are the dielectric constants at static and high frequencies, respectively,  $f_r$  is the relaxation frequency,  $i$  is the imaginary unit, and  $\alpha$  is a value between 0 and 1, which allows to describe different spectral shapes. The real part of the complex dielectric constant ( $\epsilon'$ ) is the one we commonly measure ( $\epsilon_{//}$  and  $\epsilon_{\perp}$ ), and the imaginary part ( $\epsilon''$ ) is responsible for the dielectric heating.

For a rod-like compound,  $\epsilon_{\perp}$  has a much higher relaxation frequency than  $\epsilon_{//}$  due to its shorter dipole length in the direction perpendicular to molecular axis [28]. Thus in the low frequency region, the relaxation of  $\epsilon_{//}$  as described by the real part of Cole-Cole equation is noticeable, while  $\epsilon_{\perp}$  remains unchanged ( $\epsilon_{\perp} = \epsilon_{\perp s}$ ). As a result, dielectric anisotropy ( $\Delta\epsilon = \epsilon_{//} - \epsilon_{\perp}$ ) also follows the real part of Cole-Cole equation, i.e., it has the same relaxation frequency as  $\epsilon_{//}$ :

$$\Delta\epsilon(f) = \Delta\epsilon_{\infty} + (\Delta\epsilon_s - \Delta\epsilon_{\infty}) \frac{1 + (\frac{f}{f_r})^{1-\alpha} \sin \frac{1}{2} \alpha \pi}{1 + 2(\frac{f}{f_r})^{1-\alpha} \sin \frac{1}{2} \alpha \pi + (\frac{f}{f_r})^{2(1-\alpha)}}, \quad (2-2)$$

where  $f_r = f_{r//}$ ,  $\Delta\epsilon_{\infty} = \epsilon_{//\infty} - \epsilon_{\perp s}$ ,  $\Delta\epsilon_s = \epsilon_{//s} - \epsilon_{\perp s}$ ,  $\Delta\epsilon_s$  is the static dielectric anisotropy, and  $\Delta\epsilon_{\infty}$  is the

dielectric anisotropy in the high frequency region. Similarly, the average dielectric constant  $[(2\varepsilon_{\perp} + \varepsilon_{\parallel})/3]$  should have the same relaxation frequency as well.

Since Kerr constant is linearly proportional to  $\Delta\varepsilon$  as Eq. (1-6) shows, we can modify Eq. (2-2) to describe the frequency dependent Kerr constant as:

$$K(f) = K_{\infty} + (K_s - K_{\infty}) \frac{1 + \left(\frac{f}{f_r}\right)^{1-\alpha} \sin \frac{1}{2} \alpha \pi}{1 + 2\left(\frac{f}{f_r}\right)^{1-\alpha} \sin \frac{1}{2} \alpha \pi + \left(\frac{f}{f_r}\right)^{2(1-\alpha)}}, \quad (2-3)$$

where  $K_s$  and  $K_{\infty}$  stand for the Kerr constant at static and high frequency, respectively. For convenience, we call Eq. (2-3) as extended Cole-Cole equation.

We use Eq. (2-3) to fit the measured frequency dependent  $\Delta\varepsilon$  and Kerr constant and results of sample 1 are plotted in Fig. 2.3. Eq. (2-3) has four unknowns:  $K_{\infty}$ ,  $K_s$ ,  $f_r$  and  $\alpha$ . However, in the low frequency region,  $K_s$  ( $\sim 1.48 \text{ nm/V}^2$  for sample 1) is insensitive to frequency and can be treated as a constant. Through fittings, we find  $f_r = 118 \text{ kHz}$ ,  $\alpha = 0.12$ , and  $K_{\infty} = -0.189 \text{ nm/V}^2$  for sample 1. The negative Kerr constant means the induced birefringence is negative, i.e.,  $n_e(E) < n_o(E)$ . This is because the refractive index along the  $E$  field direction  $n_e(E)$  decreases, while in perpendicular directions  $n_o(E)$  increases. As Fig. 2.3 shows, the fitted curve (pink solid line) agrees very well with experimental data. According to Cole-Cole equation, the imaginary part of dielectric constant  $\varepsilon''$  should reach its maximum value when  $f = f_r$ . Therefore, we also measured frequency dependent  $\varepsilon''$  and found that it indeed had an absorption peak at  $\sim 118 \text{ kHz}$ , same as our fitting result.

For sample 2 (Chisso JC-BP01M), we also measured its VT curves at different

frequencies. Results are plotted in Fig. 2.4 where the VT curves gradually shift to the right side and  $V_{on}$  increases as frequency increases. At 5 kHz, the transmittance at 60  $V_{rms}$  is only ~10% of that of the peak transmittance. These results indicate that frequency has a tremendous impact on the electro-optic properties of this BPLC cell.

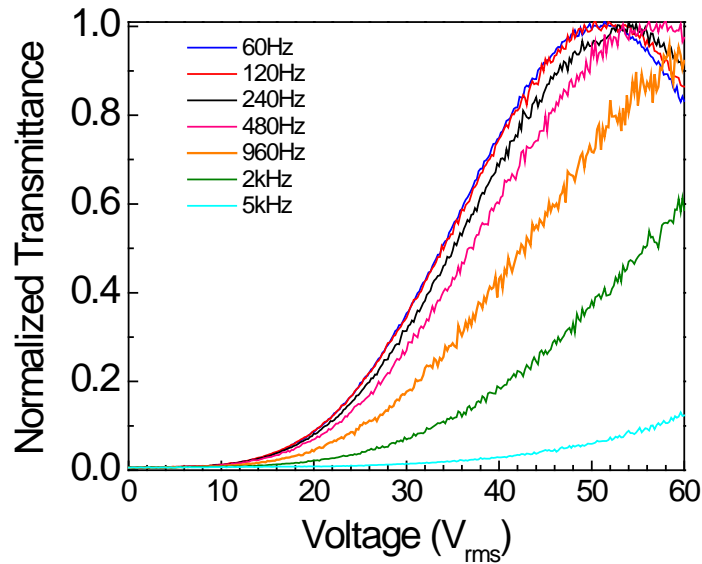


Fig. 2.4 Measured VT curves of Cell 2 at different frequencies.

We used similar procedures to fit the measured VT curves (Fig. 2.4) with extended Kerr model. Here the saturation birefringence  $\Delta n_s=0.15$  and  $K_s=10.4 \text{ nm}/V^2$ . Fig. 2.5 shows the frequency dependent Kerr constant of Chisso JCBP01M; the squares are experimental data and solid line denotes fitting using Eq. (2-3) with  $K_\infty=0$ ,  $f_r=1300 \text{ Hz}$ , and  $\alpha=0.13$ . The agreement is quite good.

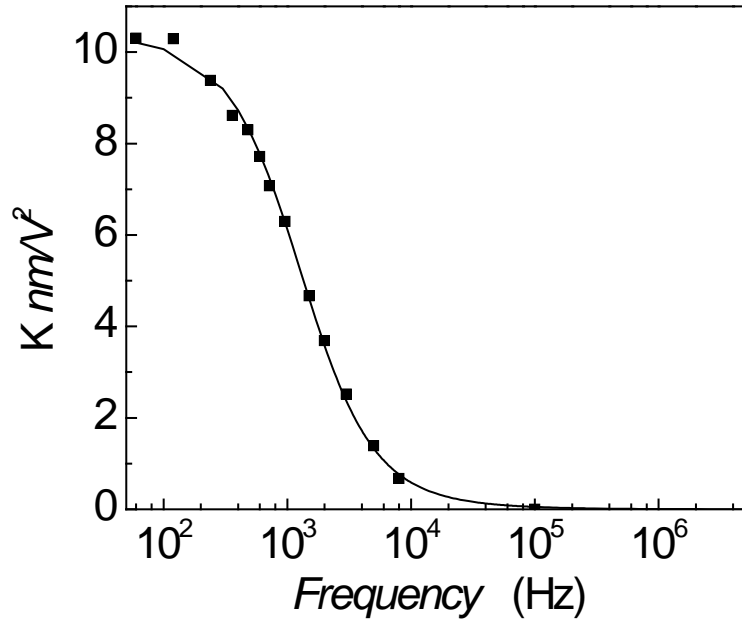


Fig. 2.5 Kerr constant versus frequency for the BPLC in Cell 2. Squares are Kerr constant obtained from VT curves, and solid line is the fitting of Kerr constant Eq.(2-3) with  $K_{\infty}=0$ ,  $f_r=1280$  Hz, and  $\alpha=0.13$ .

We also measured the temperature increase of these two IPS cells at different frequencies by attaching a thermal coupler to the glass substrate. For easy comparison, we applied a constant voltage for all frequencies: 120 V<sub>rms</sub> for sample 1 and 50 V<sub>rms</sub> for sample 2. The temperature was read after about an hour when each LC cell had reached its thermal equilibrium with the ambient. In general, as the frequency increases the cell's temperature increases. As long as  $f < 2$  kHz the temperature increase of both cells is below 5 degrees as shown in Fig. 2.6, which is acceptable for display applications.



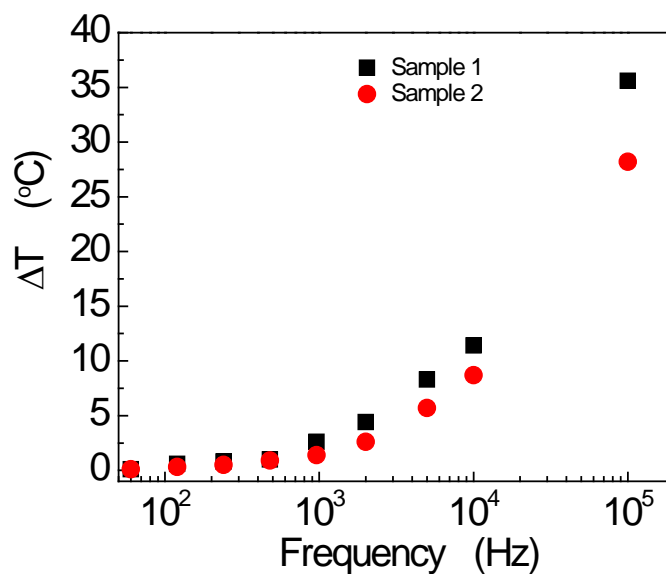


Fig. 2.6 Temperature increase of sample 1 and 2 at different frequencies.

### 2.3 Summary

In this chapter, we have experimentally investigated the frequency effects on the Kerr constants of two polymer-stabilized BPLCs. As frequency increases, Kerr constant decreases gradually. This phenomenon can be described well by the extended Cole-Cole equation. We have also investigated the dielectric heating of these two IPS cells, and found that the temperature increase for both cells is below 12 °C when the electric field frequency is below 10 kHz.

## CHAPTER 3: NEGATIVE KERR CONSTANT

As discussed in Chapter 2, since Kerr constant of a BPLC is proportional to  $\Delta\varepsilon$  of the host LC,  $K$  becomes negative when  $\Delta\varepsilon < 0$  at high frequency. Therefore, for a BPLC employing a negative host LC ( $\Delta\varepsilon < 0$ ), Kerr constant should be negative as well. The positive Kerr effect has been studied extensively however no experimental investigation on negative polymer-stabilized BPLCs has been done. In this chapter, we report for the first time a polymer-stabilized BPLC with a negative Kerr constant.

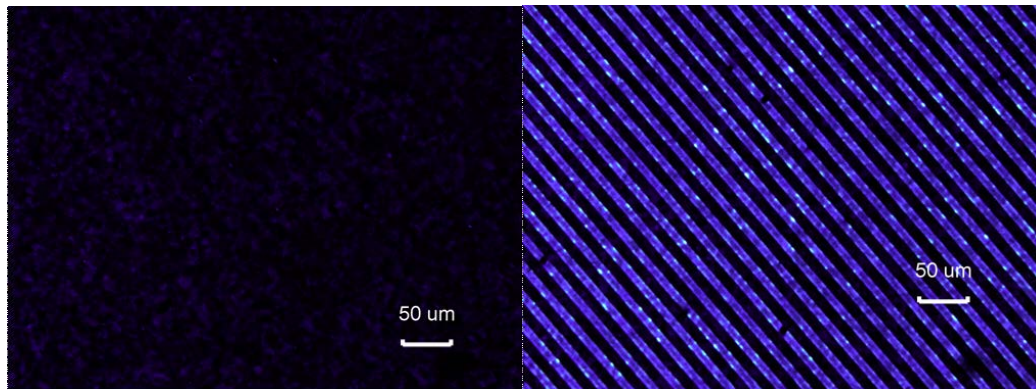
### 3.1 Material Preparations

In experiment, we fabricated polymer-stabilized BPLC composites using a large negative  $\Delta\varepsilon$  nematic LC host SLC-10V513-200 (from SLICHEM, China). Its physical properties are listed as follows:  $\Delta\varepsilon = -10.9$  at  $f = 100$  Hz, birefringence  $\Delta n = 0.147$  at  $\lambda = 633$  nm and room temperature ( $\sim 22$  °C), and clearing temperature  $T_c = 93$  °C. We mixed 84.3 wt % of the host LC, 5 wt % chiral dopant R5011 (HCCH, China) and 10.7 wt % monomers (4.7 wt % C12A and 6 wt % RM257) to form the precursor. Here, both chiral dopant and monomers are all nonpolar so that their dielectric anisotropy is negligible. The precursor was then filled into two cells. Cell 1 has IPS electrodes on the bottom substrate. The ITO (indium tin oxide) electrode width and gap are both 10  $\mu\text{m}$ , and cell gap is 7.5  $\mu\text{m}$ . Cell 2 is a VFS cell consisting of two ITO glass substrates (but without polyimide alignment layer) and has a cell gap of 10  $\mu\text{m}$ . Blue phase was observed from 61.9 °C to 70 °C during heating process and from 68.2 °C to 57.8 °C during cooling process. Both cells were cured at 61.2 °C during cooling by a UV light with  $\lambda \sim 365$  nm and intensity  $\sim 2$

mW/cm<sup>2</sup> for 30 minutes. After UV exposure, the blue phase was stabilized with a clearing temperature  $T_c \sim 82.6$  °C. For benchmarking, we made another VFS cell (Cell 3) filled with JNC JC-BP01M whose host LC has a very large positive dielectric anisotropy ( $\Delta\epsilon \sim 94$ ) [24].

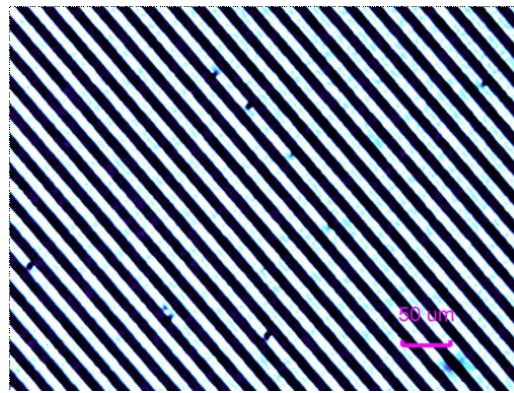
### 3.2 Electro-optical Properties

We observed Cell 1 (IPS) under a polarizing optical microscope with crossed polarizers. The electrode direction was oriented at 45° with respect to the transmission axes of polarizers. Fig. 3.1 shows the microscopic textures. From Fig. 3.1(a), at voltage-off state ( $V=0$ ) the PSBP appears dark with some purple platelets, because the central wavelength of Bragg reflection is at around 390 nm. Fig. 3.1(b) and 1(c) are with a voltage, 44 V<sub>rms</sub> and 60 V<sub>rms</sub>, respectively. In the region between electrodes, the brightness is dramatically increased, while it remains dark on the electrodes. The increased transmittance between crossed polarizers indicates that some birefringence is induced in the horizontal direction. As the voltage increases, transmittance gradually increases. The phenomenon is similar to that of an IPS polymer-stabilized BPLC cell with a positive  $\Delta\epsilon$  LC host, but it is difficult to tell whether the induced birefringence is positive or negative. We also examined Cell 2 (VFS) under the same microscope stage and observed very similar textures at  $V=0$ . However, as we applied a similar voltage no noticeable brightness change was observed. This is because the induced birefringence is along the longitudinal direction and the incident light experiences no phase retardation and is blocked by the crossed analyzer.

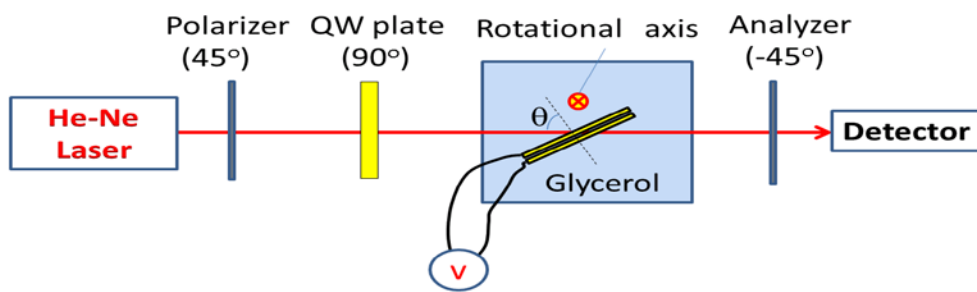


(a)

(b)



(c)



(d)

Fig. 3.1 (a) Microscopic image of Cell 1 under crossed polarizers at off state, (b) at  $44 V_{\text{rms}}$ , and (c) at  $60 V_{\text{rms}}$ ; (d) Experimental setup for measuring the electro-

optical properties of the VFS cells.

To further investigate the electro-optic properties of this PS-BPLC, we used a similar measurement method as reported in Ref. [21]. The setup is shown in Fig. 3.1 (d). A He-Ne laser beam ( $\lambda=632.8$  nm) was used as a probing light source. The VFS cell was immersed in a glass container with glycerol ( $n=1.47$ ) so that the laser beam could enter the cell at a large angle due to matched refractive index. Otherwise, the incident angle would be limited by Snell's law. The cell was sitting on a rotary stage so that the incident angle ( $\theta$ ) could be controlled easily. The transmission axes of polarizer and analyzer were set at  $45^\circ$  and  $-45^\circ$  with respect to the rotational axis of the cell, so that the ordinary ( $o$ -) wave and extraordinary ( $e$ -) wave would have the same amplitude, and the phase retardation could be extracted by the measured transmittance. A quarter-wave (QW) plate was placed after the polarizer but before the VFS cell, with its optical axis oriented at  $90^\circ$  to the VFS cell's rotational axis. Therefore, the total phase retardation after passing the QW plate and VFS cell would be  $\delta=\pi/2+\delta_{\text{VFS}}$ , where  $\delta_{\text{VFS}}=[n_{\text{eff}}(E)-n_o(E)]d/\sin\theta$ ,  $n_{\text{eff}}(E)=[(1+\text{tg}^2\theta)/(1/n_o(E)^2+\text{tg}^2\theta/n_e(E)^2)]^{1/2}$  and  $d$  is the cell gap. For a BPLC with a positive induced birefringence (i.e., positive Kerr constant),  $n_e(E)>n_{\text{eff}}(E)>n_o(E)$  and  $\delta_{\text{VFS}}$  increases with voltage, so the total phase  $\delta=\pi/2+\delta_{\text{VFS}}$  increases with a starting point of  $\pi/2$ . As a result, the transmittance  $\sin^2\delta/2$  under crossed polarizers should first increase with applied voltage in the low field region ( $0<\delta_{\text{VFS}}<\pi/2$  and  $\pi/2<\delta<\pi$ ). On the other hand, for a BPLC with a negative induced birefringence (i.e., negative Kerr constant),  $n_e(E)<n_{\text{eff}}(E)<n_o(E)$  and  $\delta_{\text{VFS}}$  is a negative value which decreases with voltage, so  $\delta=\pi/2+\delta_{\text{VFS}}$  should decrease as voltage increases. Therefore, we should observe a decreased transmittance in the low field region ( $-\pi/2 < \delta_{\text{VFS}} < 0$  and  $0 < \delta < \pi/2$ ).

To validate our assumption, we measured the voltage-dependent-transmittance curves of Cell 2 and Cell 3, and the results are shown in Fig. 3.2.

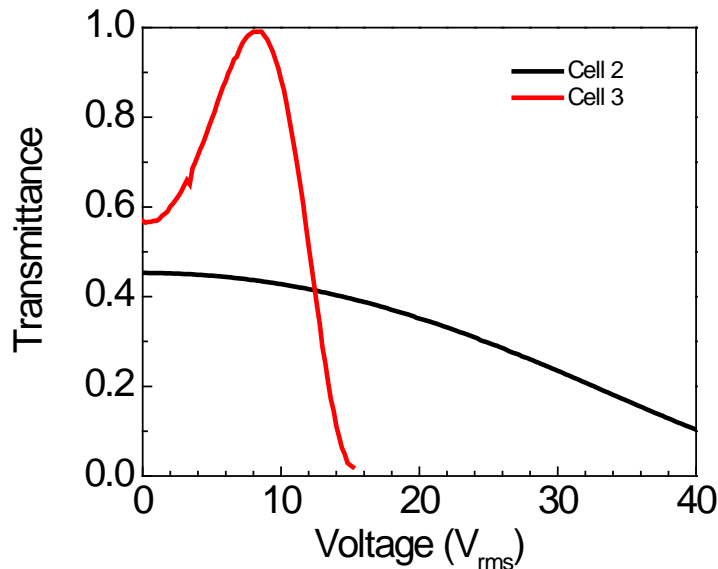


Fig. 3.2 Measured VT curves of Cell 2 and Cell 3 using the experimental setup in Fig. 3.1(d) with a QW plate in front the VFS cells.

Since the BPLC has a relatively small negative Kerr constant, we chose a large incident angle  $\theta=80^\circ$  in a VFS cell in order to accumulate sufficient phase retardation. The electric field frequency is 100 Hz. As expected, Cell 2 and Cell 3 exhibit opposite trends of transmittance change in the low field region, indicating their Kerr constants are indeed of opposite signs. The transmittance of Cell 3 (positive  $\Delta\epsilon$  PSBP) increases with voltage until 8  $V_{rms}$  and then decreases as voltage further increases. This is because the positive PSBP in Cell 3 has a large Kerr constant, and the phase retardation  $\delta_{VFS}$  reaches  $\pi/2$  ( $\delta = \pi/2 + \delta_{VFS} = \pi$ ) at  $V=8V_{rms}$ , where peak transmittance occurs. On the contrary, the transmittance of Cell 2 (negative  $\Delta\epsilon$  PSBP) decreases as voltage increases and does not reach a minimum due to its relatively small Kerr constant.

Ideally, at  $V=0$  both cells should be at 50% transmittance. But as Fig. 3.2 shows, there is a small displacement. There are two possible explanations: 1) The transmittance  $\sin^2\delta/2$  has the largest slope near  $\delta= \pi/2$ , therefore, even a small phase retardation deviation will be magnified. 2) In our VFS cell, the incident angle is quite large ( $80^\circ$ ). A small residual birefringence could lead to small phase retardation.

Next we removed the QW plate, and measured the VT curve of Cell 2 again. As shown in Fig. 3.3, the transmittance peak occurs at 80  $V_{\text{rms}}$  and the hysteresis [29]  $\Delta V/V$  is quite small  $\sim 1\%$ . The dark state of the VFS is not very good due to the large incident angle  $80^\circ$ . We used extended Kerr model [17] to fit the VT curve, and got Kerr constant  $K=-0.16 \text{ nm}/V^2$ . The small Kerr constant is mainly due to the small dielectric anisotropy  $\sim -10.1$  of the host LC.

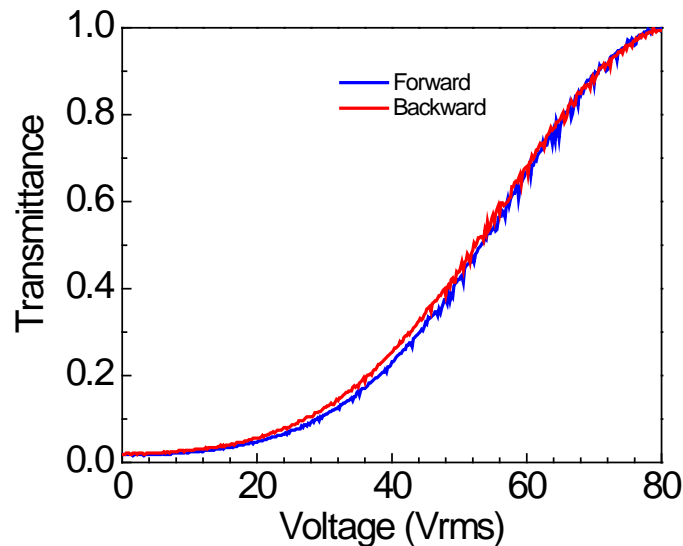


Fig. 3.3 Measured VT curve of Cell 2 using the experimental setup in Fig. 3.1(d)

without a QW plate in front the VFS cell.

We also measured the response time (between off state and peak-transmittance on state)

of Cell 2. The rise and decay time is  $\sim 1$  ms. As temperature increases, the response time decreases sharply.

### 3.3 Summary

In this chapter, a negative BPLC is stabilized, and its electro-optic properties investigated. We have experimentally proven that it has a negative induced birefringence ( $n_e < n_o$ ) and Kerr constant. The value of Kerr constant is relatively small compared to most positive polymer-stabilized BPLCs mainly due to the small  $|\Delta\epsilon|$  of the host. It has a small hysteresis  $\sim 1\%$ , and fast response  $\sim 1$  ms.



## CHAPTER 4: HIGH-EFFICIENCY TRANSMISSIVE BPLCDS

Recently, polymer-stabilized blue phase is becoming a promising candidate for next generation LCD. Because it is a self-assembled system, it does not require an alignment layer for surface treatment. Because of short coherent length, it has submillisecond response time, which could triple the optical efficiency of a LCD with color sequential mode [30]. Because it is optically isotropic for off-resonance wavelength, it would provide a good dark state and wide viewing angle for displays. In this chapter, we focus on the transmissive BPLCD, which uses a backlight to illuminate the displayed images.

### 4.1 Enhanced Protrusion Electrode Structure

In this section, we propose an enhanced protrusion electrode structure for enhancing the optical efficiency of a BPLCD [31]. In a conventional protruded IPS structure [25], the entire protrusions are covered with one type of electrode. However, in the proposed enhanced protrusion electrode, two different electrodes are coated on each side of a protrusion. The dead zones are eliminated by the in-plane switching (IPS)-like electric field distribution on the top of protrusions. As a result, the average transmittance is increased, while the operating voltage remains low.

#### 4.1.1 Device Configuration

Fig. 4.1(a) shows the conventional protrusion electrode structure [25] where the trapezoid protrusion electrode has a substantial height  $h$ . The bottom width of each electrode is  $w$ , the top width is  $w_2$ , and the gap between neighboring electrodes is  $l$ . In the gap between protrusions, electric fields

with rich horizontal components are generated and penetrating deeply into the LC bulk, resulting in a lower operating voltage. However, on the top of the protrusion, electric fields are basically vertical and do not contribute to transmittance, resulting in dead zones. Thus, the average transmittance is low.

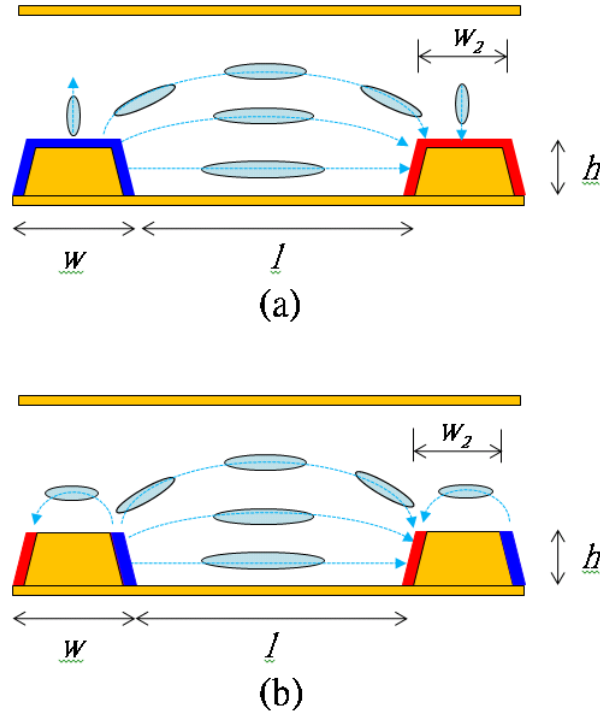


Fig. 4.1 (a) Side view of a conventional protrusion electrode structure, and (b) with enhanced protrusion electrode structure.

Fig. 4.1(b) shows the enhanced protrusion electrode structure where one side-wall of a protrusion is coated with pixel electrode (red), and the other is with common electrode (blue). In the gap between protrusions, the electric field distribution is similar to that in conventional protruded structure, so that the low operating voltage feature is still maintained. However, on the top of protrusions, there is no longer dead zone. Instead, it is like IPS structure, generating horizontal fields and inducing transmittance. Therefore, the average transmittance is increased.

### 4.1.2 Simulation Results

To validate the concept, we carried out the electro-optical simulation as in Ref [23]: First we used commercial software DIMOS (AUTRONIC-MELCHERS GmbH) to obtain the electric field potential distribution, then use 2x2 extended Jones Matrix method [32,33] to finish the optical calculation. The Kerr constant here used is  $12.68 \text{ nm/V}^2$  and the saturation birefringence of the BPLC mixture is assumed to be 0.2.

Fig. 4.2 compares the voltage-dependent transmittance (VT) curves of the conventional and enhanced protrusion structures. The red curve denotes the VT for a traditional IPS structure with electrode height  $\sim 50 \text{ nm}$ . The IPS structure with an electrode width  $w=2 \text{ }\mu\text{m}$ , gap  $l=4 \text{ }\mu\text{m}$  and cell gap  $10 \text{ }\mu\text{m}$ , has a 67% transmittance at  $\sim 40 \text{ V}_{\text{rms}}$ . The blue curve is for a conventional protrusion structure with  $w=2 \text{ }\mu\text{m}$ ,  $w_2=1 \text{ }\mu\text{m}$ ,  $l=4 \text{ }\mu\text{m}$  and height  $h=2 \text{ }\mu\text{m}$ . The on-state voltage is reduced to  $\sim 17 \text{ V}_{\text{rms}}$  while the peak transmittance is boosted to  $\sim 75\%$ . The black curve is for the corresponding enhanced protrusion structure with the same parameters. The peak transmittance is increased to  $\sim 85\%$ , although the peak-transmittance voltage is slightly higher. The magenta curve is for a conventional protrusion with  $w=2 \text{ }\mu\text{m}$ ,  $w_2=1 \text{ }\mu\text{m}$ ,  $l=2 \text{ }\mu\text{m}$  and height  $h=2 \text{ }\mu\text{m}$ . With a smaller gap  $l$ , the operating voltage is further reduced to  $10 \text{ V}_{\text{rms}}$ , but the transmittance is somewhat lower ( $\sim 63\%$ ). On the other hand, the corresponding enhanced protrusion structure (green curve) has a higher transmittance ( $\sim 69\%$ ) with almost the same operating voltage.

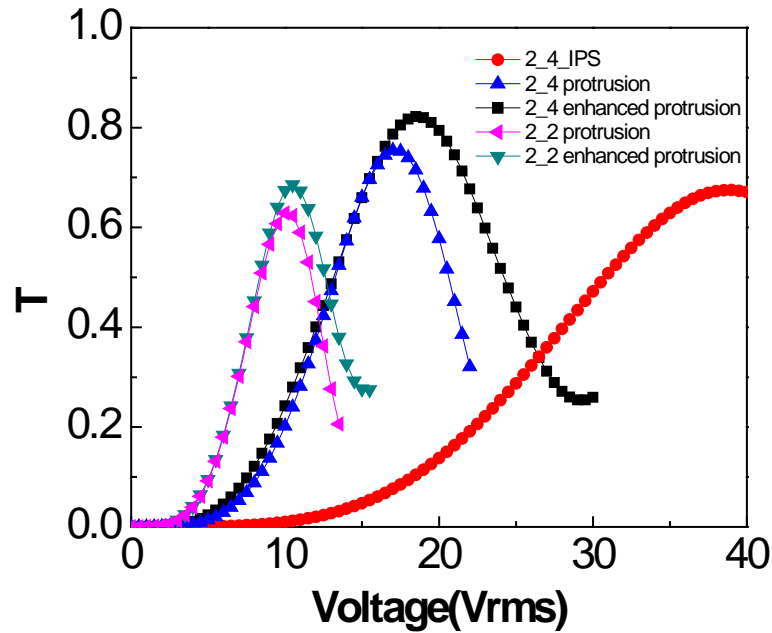


Fig. 4.2 VT curves of IPS electrode (red), conventional protrusion structures (blue and magenta) and new protrusion structures (black and green).

#### 4.2 Complementary Enhanced Protrusion Electrode Structure

In the previous section, by removing the dead zones we have improved the transmittance by more than 10%. The optical efficiency is reasonably high compared to most BP LCDs. However, compared to nematic LCDs such as fringe field switching (FFS) displays (Transmittance >90%), the optical efficiency of the proposed enhanced protrusion structure in the previous section is still low.

In this section, we propose another electrode design based on the previous enhanced protrusion electrode structure, which could improve the optical transmittance to 100%.

### 4.2.1 Device Configuration

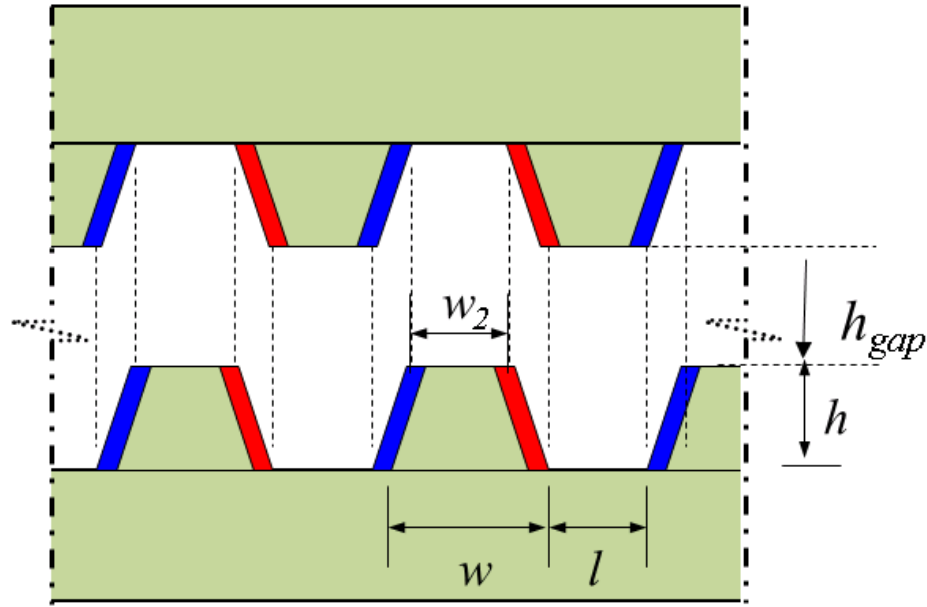


Fig. 4.3 Side-view of the complementary enhanced protrusion electrode structure.

Fig. 4.3 shows the side-view of the proposed complementary enhanced protrusion electrode structure. On both top and bottom glass substrates, enhanced protrusion structures are formed, with one side of each protrusion coated with pixel electrode (red) and the other coated with common electrode (blue). The top and bottom protrusion electrodes are complementarily arranged. The gap between two top protrusions is aligned with the bottom protrusions; the top pixel electrodes are aligned with bottom pixel electrodes, and the top common electrodes are aligned with bottom common electrodes. The height of protrusions is  $h$ , the vertical gap between top and bottom protrusions is  $h_{gap}$ , the width of each protrusion is  $w$ , and the gap between adjacent protrusions is  $l$ . When voltage is applied, horizontal electric fields are generated in the gap between protrusions. According to Kerr effect, birefringence is induced and so is phase

retardation. The region between protrusions is the effective area which mainly contribute to transmittance, and in the location of protrusions, there is small transmittance. Since the top and bottom structures are complementarily aligned, the top effective area is aligned with the bottom protrusions, and the bottom effective area is aligned with the top protrusions. As a result, the superimposed transmittance from top layer and bottom layer is uniform across the pixel, and high average transmittance can be achieved.

Besides, the height of the protrusions provides a low operating voltage for the BPLCD, similar to the case in last section.

### 4.2.2 Simulation Results

Fig. 4.4 shows the voltage-dependent transmittance for the display devices of the enhanced protrusion electrodes.

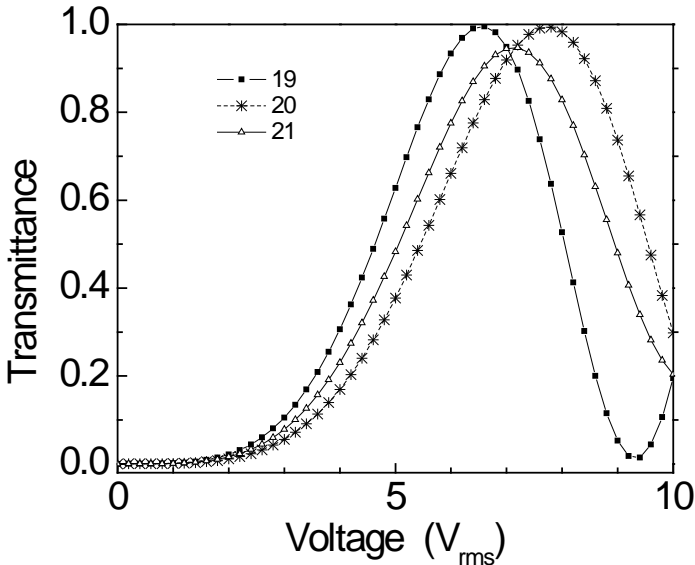


Fig. 4.4 VT curves for the proposed complementary enhanced protrusion electrode structure with different dimensions.

Curve 19 is the VT curve for the structure with  $w=2\ \mu\text{m}$ ,  $w_2=2\ \mu\text{m}$ ,  $l=2\ \mu\text{m}$ ,  $h=3\ \mu\text{m}$  and  $h_{gap}=1\ \mu\text{m}$ ; and curve 20 is for the structure with  $w=2\ \mu\text{m}$ ,  $w_2=2\ \mu\text{m}$ ,  $l=2\ \mu\text{m}$ ,  $h=2\ \mu\text{m}$  and  $h_{gap}=1\ \mu\text{m}$ . As shown in Fig. 4.4, both curve 19 and 20 have more than 99% peak transmittance. The high transmittance is a result of uniform distributed transmittance profile in the horizontal direction, which is due to three main reasons. First, the pixel and common electrodes are formed on the steep sides of the rectangular protrusions, so that the electric fields induced between them are uniform. These areas are called effective regions. Second, the top and bottom substrates are aligned in such a way that the top and bottom effective regions could just compensate each other. Third, the width of the top and bottom protrusions is equal to the gap between the adjacent protrusions, so that the phase retardation remains uniform after superimposition. If  $w>l$ , there would be some regions where the top and bottom protrusions overlap and create dead zones. On the other hand, if  $w<l$ , some regions accumulate phase retardation from both top and bottom effective regions, while the other regions only accumulate from one effective region. In neither case, peak transmittance could be obtained at different locations simultaneously, and the non-uniform transmittance distribution leads to a lower average transmittance. Curve 19 has a lower operating voltage than curve 20 due to a larger protrusion height  $h$ . Curve 21 represents the VT curve for a structure with  $w=2\ \mu\text{m}$ ,  $w_2=1\ \mu\text{m}$ ,  $l=2\ \mu\text{m}$ ,  $h=3\ \mu\text{m}$  and  $h_{gap}=1\ \mu\text{m}$ . This structure has trapezoid protrusion shape which is more likely to form in the real fabrication. However, the uniformity of phase retardation is deteriorated and the peak transmittance decreased to ~95%, which is still high.

## **CHAPTER 5: HIGH-EFFICIENCY TRANSFLECTIVE BPLCDS**

In chapter 4, we have improved the optical efficiency of a transmissive blue phase LCD which has superb performances indoor. However, when such a display is exposed to strong sunlight the displayed images could be washed out, leading to a degraded contrast ratio and readability. To overcome sunlight readability problem, a common approach is to adaptively boost the backlight intensity, but the tradeoff is on the increased power consumption. In this chapter, we propose a transflective blue phase LCD [31,34] where backlight is turned on during dark ambient and ambient light is used to illuminate the displayed images under bright ambient. Therefore, a good contrast ratio is preserved while the power consumption is reduced.

Low power and wide-view transflective liquid crystal displays (TR-LCDs) are attractive for mobile applications because of their good sunlight readability and long battery life [35,36]. A major technical challenge of TR-LCDs is to balance the optical path-length disparity between the transmissive (T) and reflective (R) pixels. In T mode the backlight passes through the LC layer once, while in R mode the ambient light traverses the LC layer twice. To achieve the same phase retardation for T and R regions, both double-cell-gap and single-cell-gap TR-LCDs have been developed [36]. Each approach has its own pros and cons. To reduce power consumption, a TR-LCD using color-sequential LED backlight for T mode has been proposed [37]. By eliminating spatial RGB color filters, the optical efficiency and resolution density are all tripled. However, to suppress color breakup [30,38] due to sequential colors the LC response time has to be less than ~1 ms which imposes a big challenge to nematic LCs. Therefore, transflective BPLCD, with submillisecond response time, is a good candidate.



## 5.1 A Transflective BPLCD Based on Protrusion Electrodes

In this section, we propose a low power, wide view, and single-cell-gap TR-LCD using a polymer-stabilized BPLC [34]. To reduce operating voltage, we use protrusion electrodes so that the electric fields penetrate deeply into the bulk LC layers. To balance the optical phase retardation and obtain well-matched voltage-dependent transmittance (VT) and reflectance (VR) curves, we design the T and R regions to have different electrode gaps. The wider electrode gap in the R region generates a weaker electric field in order to accommodate the double pass of the ambient light. To obtain wide viewing angle, we employ two broadband wide-view circular polarizers and biaxial films.

### 5.1.1 Device Configuration

Fig. 5.1 depicts the device structure of the proposed transflective BP LCD. The cell is sandwiched between two crossed circular polarizers. Each pixel is divided into T and R regions. In both regions, trapezoid protrusion electrodes are formed to lower the operating voltage [25]. The dimensions of the protrusions are defined as follows:  $w_2$  is the top width,  $w$  is the bottom width,  $h$  is the protrusion height,  $l_T$  and  $l_R$  are the space between common (C) and pixel (P) electrodes in T and R regions, respectively. If the protrusion height is less than  $2\ \mu\text{m}$ , then the transmittance and reflectance are insensitive to cell gap as long as it exceeds  $\sim 5\ \mu\text{m}$ . Thus, we choose the cell gap in both regions to be  $10\ \mu\text{m}$ . However, the gap  $l_T$  is intentionally made smaller than  $l_R$  so that the R region exhibits a weaker fringing field which, in turn, generates a smaller induced birefringence. This plays a key role to balance the phase retardation between the T and R modes. In a TR-LCD, the backlight passes the T region once, but the ambient light

traverses the R region twice. The weaker induced birefringence in the R region compensates the double pass of the ambient light. The matched VT and VR curves will allow the single gamma curve driving, which simplifies the electronic circuits. Moreover, in a polymer-stabilized BPLC cell, there is no need for an alignment layer. Therefore, the fabrication is much simpler.

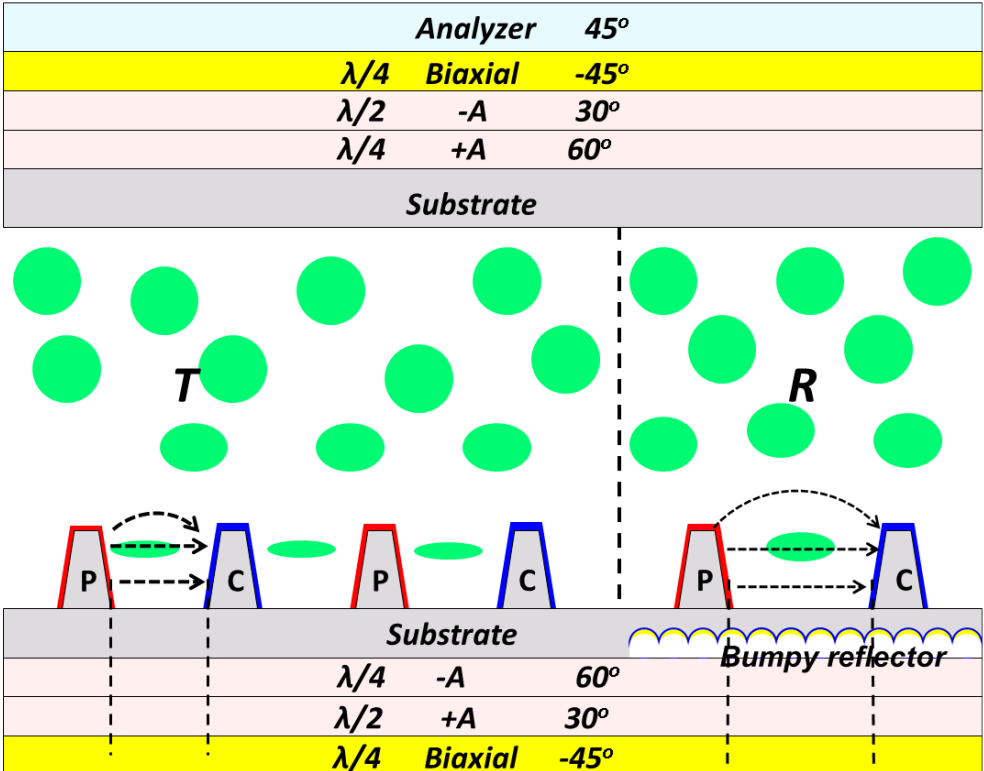


Fig. 5.1 Device structure of the TR PS-BP LCD based on protrusion electrodes, P stands for pixel electrode and C for common electrode.

To obtain normally black mode for both T and R regions, we use two broadband and wide-view circular polarizers [39] consisting of positive and negative A-plates as Fig. 5.1 shows. The combination of positive and negative A-plates results in a much better viewing angle because they compensate well to each other over a large viewing zone. The BPLC is optically isotropic in the voltage-off state. Thus, the proposed crossed circular polarizer configuration

works equally well for both T and R modes. This is another major advantage for using BPLC in transfective displays because it does not require any negative C-plate [40] or in-cell phase retarder [41]. These components are generally required for TR-LCDs employing a nematic LC.

To achieve an even better contrast ratio over wide viewing angles, two biaxial  $\lambda/4$  plates are placed below the top linear polarizer and above the bottom linear polarizer, as Fig. 5.1 shows. A conventional  $\lambda/2$  biaxial compensation film would assure a good viewing angle for the T region, but could not improve the R region significantly at the same time. However in our configuration, when the ambient light passes through the biaxial  $\lambda/4$  plates twice in the R region, it is equivalent to experience a  $\lambda/2$  retardation as in the T region. As a result, the compensation effect in the T and R regions are similar which leads to wide viewing angle in both T and R regions.

### 5.1.2 Simulation Results

To validate the device concept, we simulated the electro-optic characteristics of this transfective BP LCD. We first used commercial software DIMOS to calculate the electric potential and electric field ( $E$ ) distributions. The induced birefringence  $\Delta n_{ind}$  is then calculated from Kerr effect [14]. The Kerr constant used here is  $12.7 \text{ nm/V}^2$ .

After we have obtained the birefringence distribution, we apply extended Jones matrix methods to calculate the electro-optical properties [23]. In order to achieve low operating voltage and high transmittance, the parameters of the protrusion electrode are optimized at:  $w_2=0.5 \text{ }\mu\text{m}$ ,  $w=1 \text{ }\mu\text{m}$ ,  $h=2 \text{ }\mu\text{m}$ ,  $l_T=2 \text{ }\mu\text{m}$ , and  $l_R=3 \text{ }\mu\text{m}$ . And the optimized biaxial film:  $N_z=(n_x-n_y)/(n_x-n_z)=0.5$ .

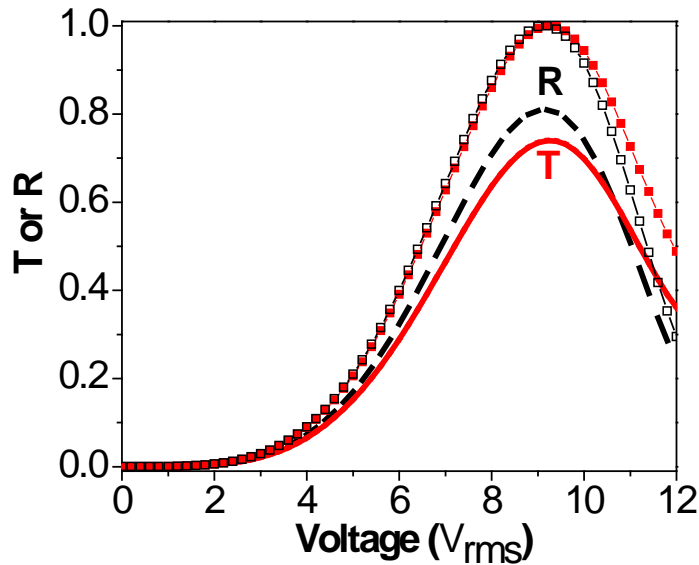


Fig. 5.2 Simulated VT and VR curves for the proposed TR BPLCD using protrusion electrodes. The red (solid) and black (dashed) lines represent simulated VT and VR curves, and the closed and open squares represent normalized transmittance and reflectance.

Fig. 5.2 shows the simulated VT and VR curves at  $\lambda=550$  nm, both of which are normalized to the transmittance of two parallel polarizers (34.83%). Red curve (solid line) represents the transmittance, with a peak of  $\sim 74\%$ , and black curve (dashed lines) represents the reflectance with a peak of  $\sim 81\%$ . Both T and R modes have a reasonably high optical efficiency. The on-state voltage for both regions occurs at  $\sim 9.2$   $V_{\text{rms}}$ , thus this device can be addressed by amorphous-silicon thin film transistors (a-Si TFTs). The closed and open squares represent the normalized transmittance and reflectance, respectively. They overlap with each other quite well, which enables a single gamma curve driving.

Fig. 5.3 (a) and (b) depict the simulated isocontrast contour plots of the T and R regions,

respectively. To take the color dispersion into account, in our isocontrast simulation, we assume the white light spectrum contains 60% green ( $\lambda=550$  nm), 30% red ( $\lambda=650$  nm), and 10% blue ( $\lambda=450$  nm). From Fig. 5.3, the averaged contrast ratio in the T region remains quite good: the 1000:1 contrast ratio (CR) is over  $45^\circ$  viewing cone and 100:1 is over the entire viewing cone. In the R region, CR=10:1 is over  $50^\circ$ . These wide-view characteristics originate from the optically isotropic property of the BPLC.

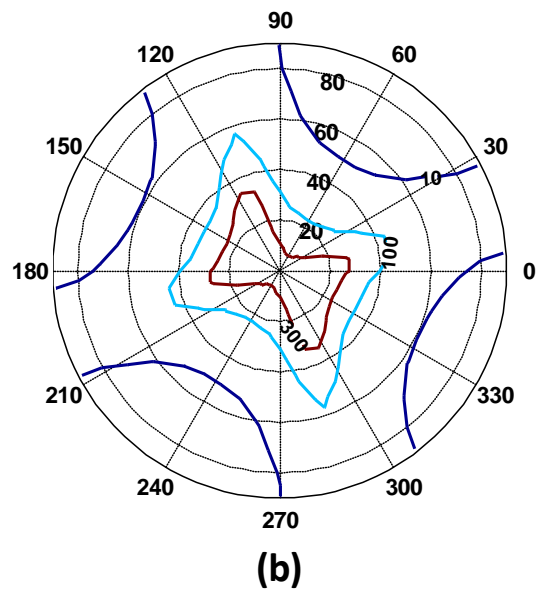
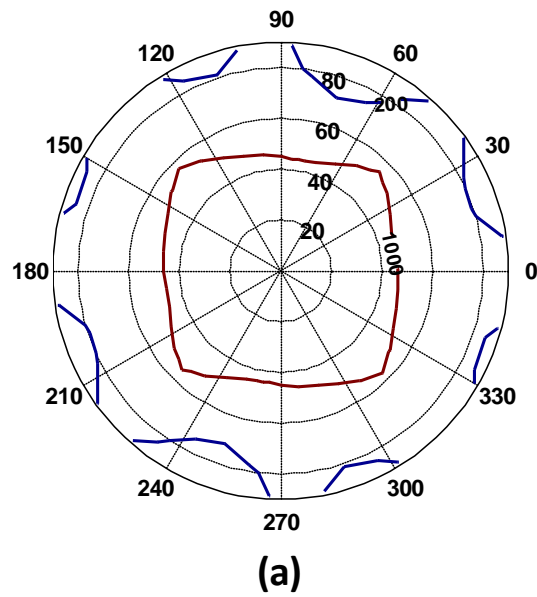


Fig. 5.3 Isocontrast contour plots for (a) T mode and (b) R mode of the proposed TR-LCD using protrusion electrodes.

For BPLC devices, the operating voltage remains relatively high as compared to

conventional nematic LCDs in which the operating voltage is lower than  $7 V_{\text{rms}}$ . Two approaches have been commonly taken to lower the operating voltage of BPLC devices: employing a large Kerr constant material, and optimizing the electrode configuration. As the nano-imprinting technology advances, the fabrication of small dimension protrusion electrodes will no longer be a hurdle. Thus, the operating voltage could be further reduced, which is highly desirable for mobile display devices.

### 5.1.3 Conclusion

In this section, we proposed a low power, wide view, and single-cell-gap transfective display based on blue-phase LC. Its submillisecond response time would undoubtedly reduce the image blurs no matter whether spatial color filters are used or not. If we decide to remove color filters and employ RGB LED backlight for sequential color operation in T region, its optical efficiency and resolution density are both tripled. However, the R mode is in black and white. Both T and R regions of this TR-LCD exhibit a reasonably high optical efficiency, and the operating voltage is below  $10V_{\text{rms}}$  which can be addressed by a-Si TFTs. The viewing angle for T mode is very good, and for R mode is also adequate. This is because the BPLC has an optically isotropic dark state. Moreover, the VT and VR curves match quite well which enables a single gamma curve driving. As the nano-imprinting technology advances, the fabrication of protrusion electrodes will become easier. As a result, the proposed transfective BP LCD has great potential for mobile display applications.

## **5.2 A Transflective BPLCD Based on Enhanced Protrusion Electrodes**

In Section 4.1, we have introduced enhanced protrusion structure for transmissive displays. Such a structure could also be used for transflective displays [31]. In this section, we present a transflective blue phase LCD using enhanced protrusion electrodes.

### **5.2.1 Device Configuration**

As shown in Fig. 5.4, the BPLC cell is sandwiched between two crossed circular polarizers. A non-metal bumpy reflector is formed on the top of each protrusion and these regions work as reflective (R) mode; and the rest of the pixel works as transmissive (T) mode. In the T region, the substantial height of the protrusion enables electric fields to penetrate deeply into the BPLC layer, resulting in large phase retardation. In the R region, the IPS-like electric field distribution has a shallow penetration so that the accumulated phase retardation is relatively small. However, the ambient light traverses the R region twice and the phase retardation is doubled. As a result, the transmittance and reflectance could be matched by properly designing the structure. Moreover, the electric fields generated by IPS electrodes in the T and R regions have a limited penetration depth. As long as the cell gap exceeds the electric field penetration depth, the VT and VR curves are insensitive to the cell gap. That means, both T and R regions could have the same cell gap, which makes the fabrication much easier.



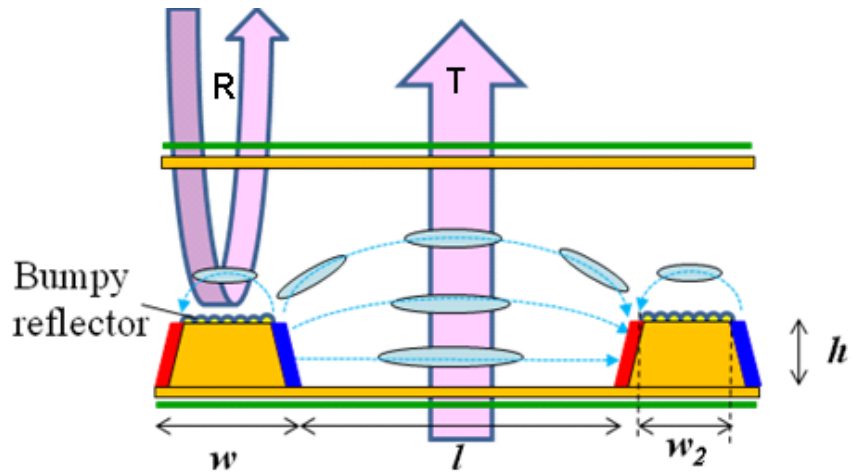


Fig. 5.4 Device configuration of the TR BPLCD based on enhanced protrusion electrodes.

### 5.2.2 Simulation Results

For an optimized structure, where  $w = 3\mu\text{m}$ ,  $w_2 = 2\mu\text{m}$ ,  $h = 2\mu\text{m}$ ,  $l = 3.3\mu\text{m}$  and cell gap =  $10\mu\text{m}$ , we plot the VT and VR curves at  $\lambda = 550\text{ nm}$  in Fig. 5.5. The red and black solid lines represent the VT and VR curves for the T and R regions, respectively; both are normalized to the transmittance of two parallel polarizers. At  $16.4 V_{\text{rms}}$ , the transmittance reaches 84.4% while reflectance reaches  $\sim 80\%$ . The dotted curves denote the normalized VT and VR curves to their individual transmittance and reflectance at  $16.4 V_{\text{rms}}$  respectively. We obtain well-matched VT (red dots) and VR (black dots) curves to enable single gamma driving.

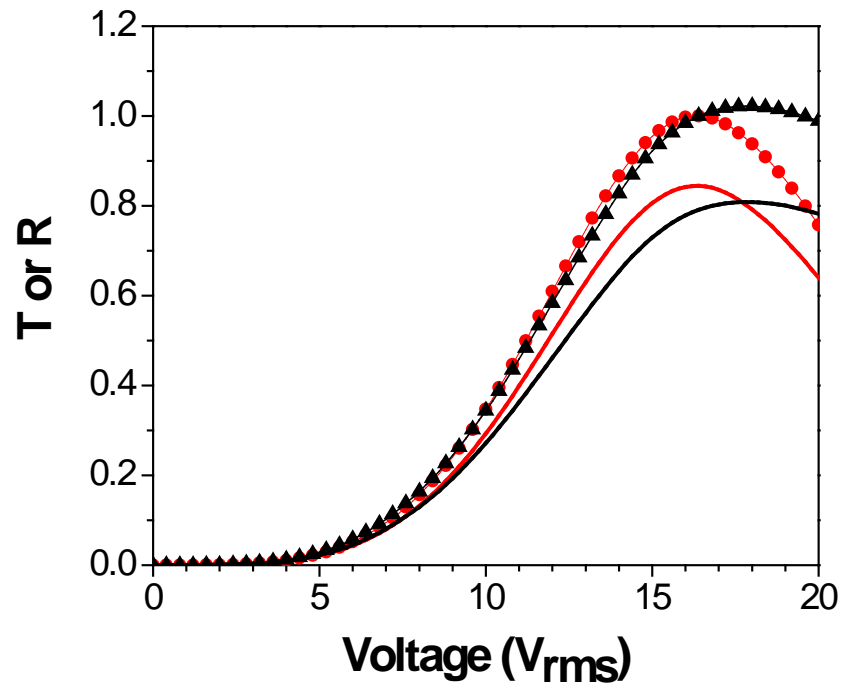


Fig. 5.5 VT and VR curves for the TR BPLCD using enhanced protrusion electrodes. The red and black lines represent simulated VT and VR curves, and the red dots and black dots represent normalized transmittance and reflectance.

By using the broadband wide-view circular polarizers [39], we obtain a very wide view in the T region and reasonably wide view in the R region. The isocontrast plots are shown in Fig. 5.6. BP LCDs have inherently wide view due to its optically isotropic dark state.

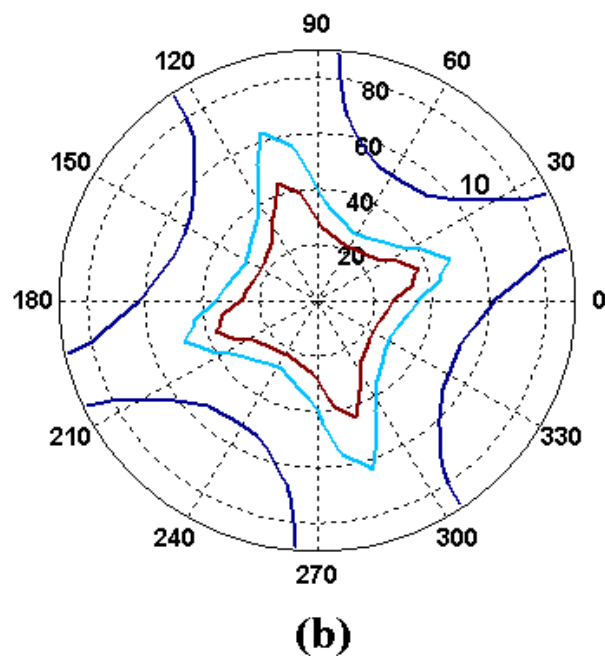
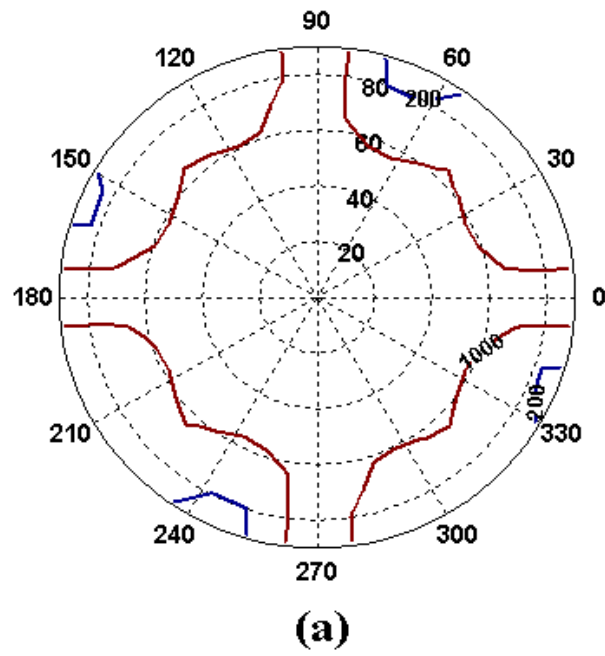


Fig. 5.6 Isocontrast plots of the TR BPLCD based on enhanced protrusion electrodes: (a) T region and (b) R region.

### **5.2.3 Conclusion**

We have proposed a single-cell-gap transflective BP-LCD based on enhanced protrusion design, both T and R regions could achieve a reasonably high transmittance (~84.4%) and reflectance (80%). Moreover, the well-matched normalized VT and VR curves enable a single gamma driving.

### **5.3 Summary**

In this chapter, we have proposed two transflective blue phase LCDs. Both of them could achieve wide viewing angle, single cell gap, single gamma driving, and high optical efficiency. By using the ambient light to readout the displayed images, our transflective blue phase LCDs could significantly reduce the power consumption while maintaining high contrast ratio. If the T region further adopts color sequential operating mode, which is made possible by the submillisecond response time of polymer-stabilized BPLCs, the optical efficiency could be further improved. These high-efficiency transflective LCDs would be attractive for mobile devices.

## **CHAPTER 6: HIGH-EFFICIENCY 3D DISPLAYS BASED ON BPLCS**

### **6.1 Introduction to 3D Displays**

Conventional display gives the image in two dimensions. In recent years, there has been an increased interest to develop three-dimensional (3D) displays [42-46] for various applications such as entertainment, medical sciences, robotics, manufacturing, and defense. A 3D display is a display device capable of conveying depth perception to the viewer.

Most practical 3D displays are stereoscopic. The basic principle is to present offset images to the left and right eyes. And human brain would give the perception of 3D depth based on the 2D offset images. The more offset the two 2D images appear, the shorter the distance between the object and viewer interpreted. There are various ways of realizing stereoscopic displays.

#### **6.1.1 Head Mounted 3D Displays**

Head mounted 3D display is the simplest way of realizing 3D perception. The viewer wears the head mounted display which consists of two screens. The left eye only sees the image from the left screen and the right eye only sees from the right screen. The two screens display two offset images respectively as shown in Fig. 6.1, and human brain extracts the depth information.

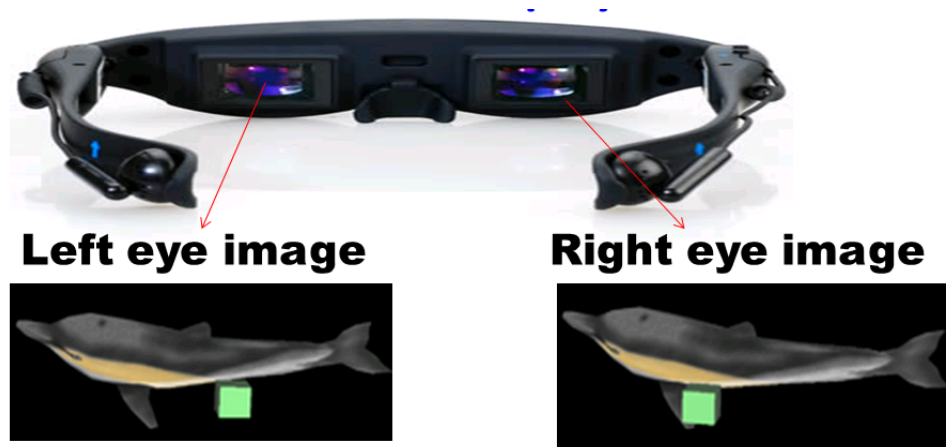


Fig. 6.1 Working principle of head mounted 3D displays.

Such displays could only be used for a single viewer. It is usually heavy and inconvenient, and thus not the mainstream of 3D displays.

### 6.1.2 Anaglyph

A pair of glasses consists of two complementary color filters for left and right eyes, respectively. The two color filters could be red and cyan, or any other complementary colors. As shown in Fig. 6.2, two images are superimposed in an additive light setting through two filters. Glasses with colored filters in each eye separate the appropriate images by canceling the filter color out and rendering the complementary color black. The glasses are simple and cheap, but such displays could not display full-color images.

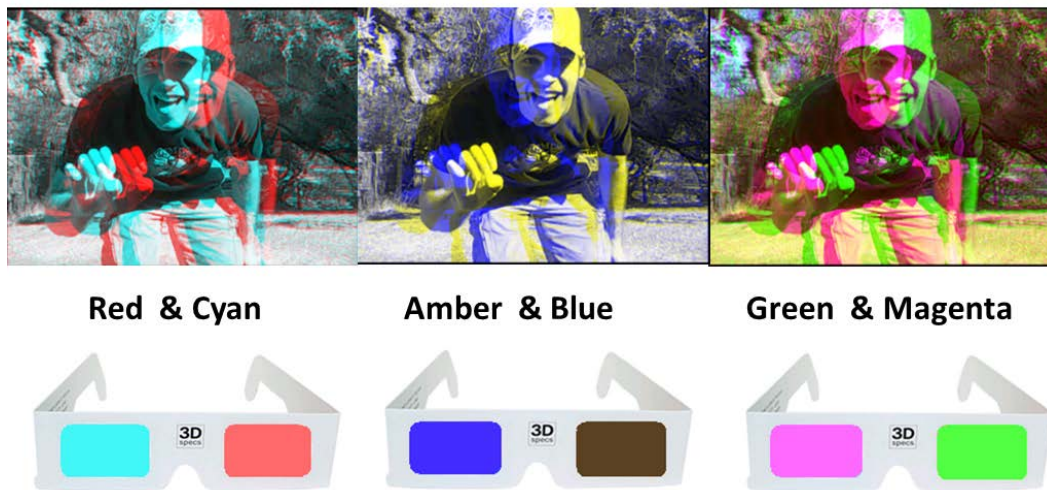


Fig. 6.2 Working principle of anaglyph 3D displays.

### 6.1.3 Polarizing Glasses

The 3D imaging technology based on polarizing glasses is commonly used in cinemas for 3D movies. To present a stereoscopic picture, two images are projected to the same polarization preserving screen through different polarizing filters. The viewer wears a pair of eyeglasses which also contain a pair of polarizing filters which allow orthogonal polarized light to pass through. Each polarizer filter on the eyeglasses passes only the light which is similarly polarized and blocks the light polarized differently, therefore each eye sees a different image. The two polarizing filters could be two linear polarizers with transmissive axis perpendicular to each other (e.g., IMAX), or one right-handed circular polarizer and the other left-handed circular polarizer (e.g., RealD). The circular polarizing glasses allow the viewer to tilt their head sideways, while linear polarizing glasses would have severe crosstalk when the viewer's eyes are not aligned with the screen. But circular polarizing glasses have limited viewing angle, consequently, for very large screens, linear polarizing glasses work better.

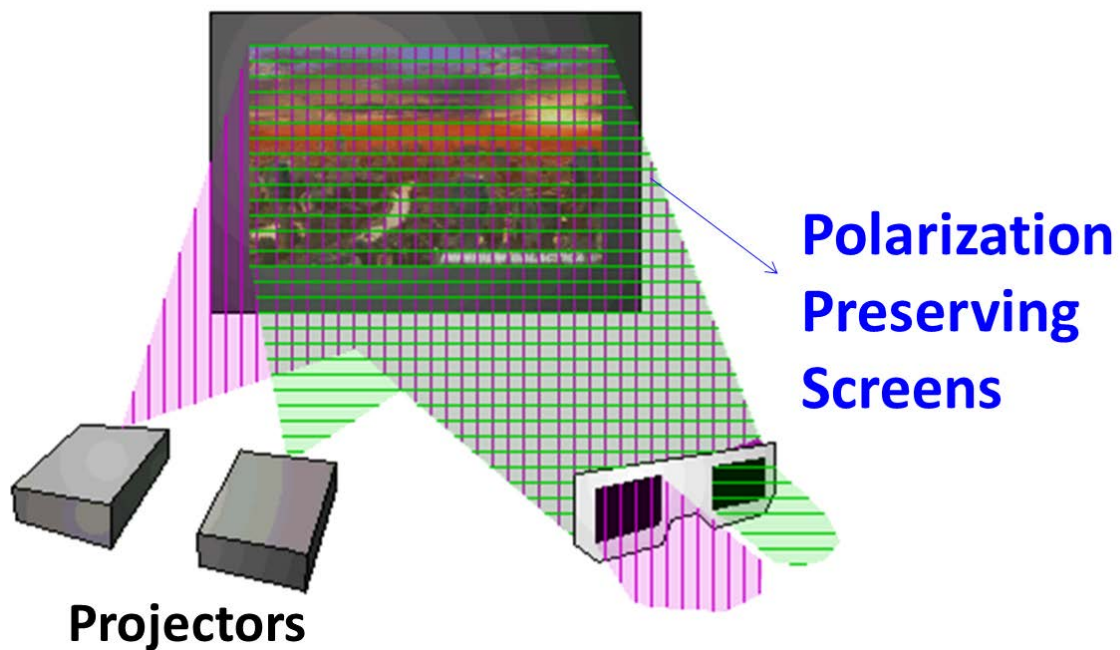


Fig. 6.3 Working principle of 3D displays based on two projectors and polarizing glasses.

Besides using projectors, we can also generate two offset orthogonal-polarized images by using patterned retarders [47] on display panels. As shown in Fig. 6.4, left-eye and right-eye pixels are arranged alternatively. Due to the patterned retarder, light from all the left-eye pixels is polarized in  $-45^\circ$  direction while that from all the right-eye pixels in  $45^\circ$  direction. With a pair of matching polarizing glasses, the left eye only sees the image formed by the left-eye pixels, and the right eye only sees the image formed by the right-eye pixels. In such displays, the spatial resolution is reduced to half. There are some similar technologies such as using active patterned retarder, which would maintain the same resolution as 2D display but requires fast switching time.



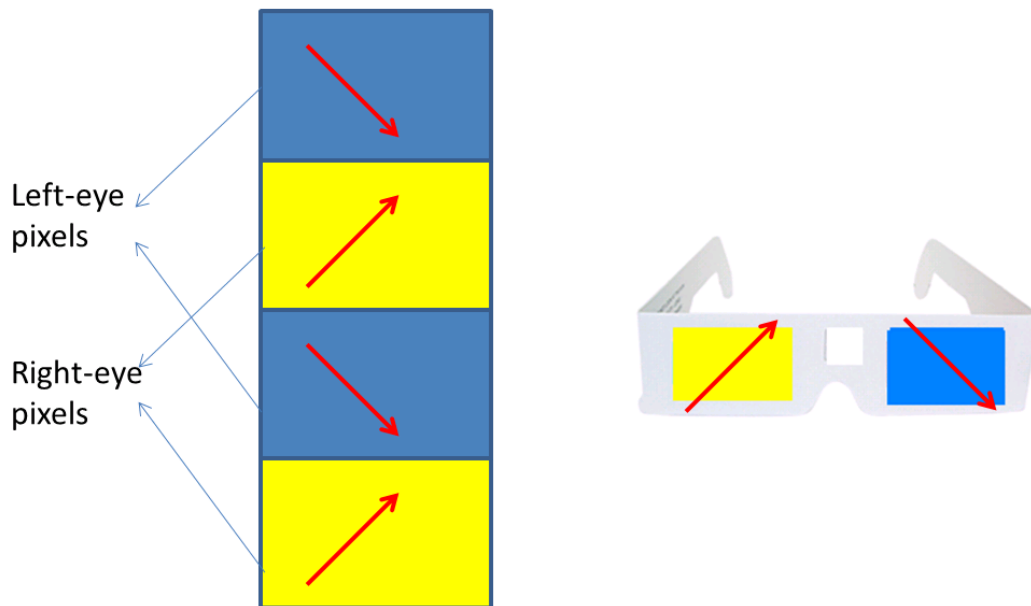


Fig. 6.4 Working principle of 3D displays based on patterned retarders and polarizing glasses.

Regardless of the method for generating two polarized offset images, due to the use of polarizing glasses, always half of the light is absorbed, and the optical efficiency is relatively low.

#### 6.1.4 Shutter Glasses

Fig. 6.5 shows the working principle of 3D displays based on shutter glasses. The left and right shutters close and open alternatively at a very high speed (e.g., 120 Hz). For instance, at odd frames, the display shows the image of left offset image. The shutter glasses are synchronized with the display, blocking the right eye and allowing light only to enter the left eye. Therefore, this frame only goes to the left eye. On the other hand, at even frames images only go

to the right eye. The human brain would integrate 3D images based on the time-sequence offset images. The crosstalk of such 3D displays is usually low. But the glasses are heavy, require a power supply and need synchronization with display panels. At each frame, only half of the light is seen by one eye, half is absorbed by the shutter, so the optical efficiency is not high.

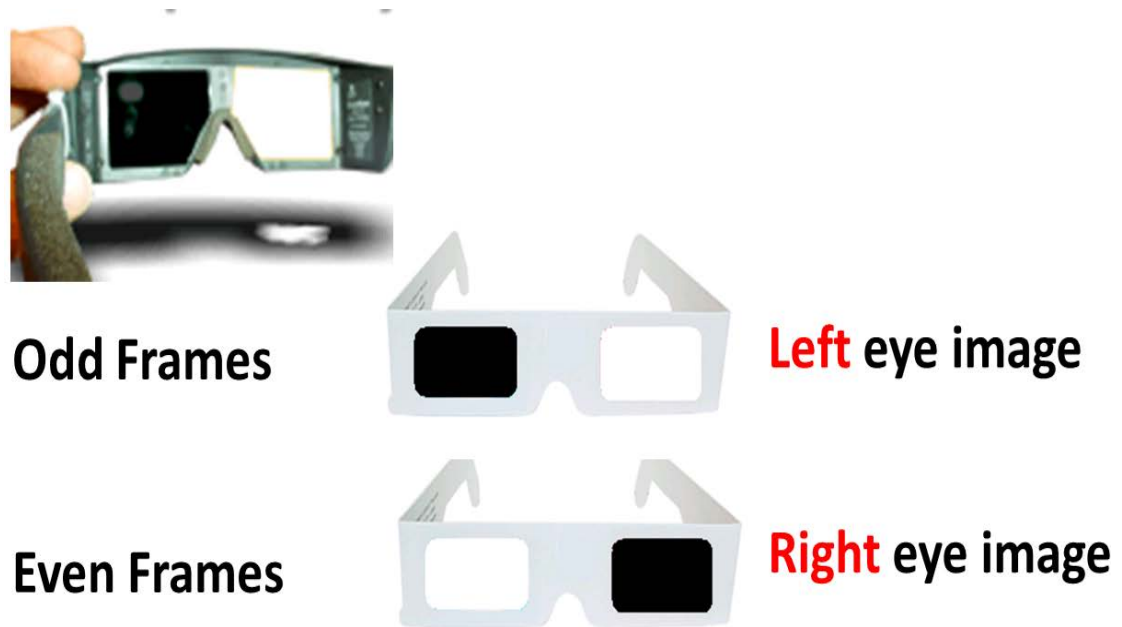


Fig. 6.5 Working principle of 3D displays based on shutter glasses.

### 6.1.5 Autostereoscopy

Autostereoscopy is a method of generating stereoscopic images without using any glasses. There are two methods (lenticular lenses or parallax barriers) that redirect incoming imagery to several viewing regions. When the viewer's eyes are located in a certain position, a left-eye image is seen with the left eye, and a right-eye image seen by the right eye, giving a convincing illusion of 3D. However, there are some viewing zones, where only 2D image or inverse image (right image seen by the left eye and left image seen by the right eye) would be seen. Such

displays can have multiple viewing zones allowing multiple users to view the 3D image at the same time.

The working principle of autostereoscopic displays based on parallax barrier is shown in Fig. 6.6. The parallax barrier is kept at a distance from the display pixels. Consequently, the left and right pixels are redirected to different viewing zones and seen by left and right eyes respectively. Because the barrier blocks a lot of light, the crosstalk is usually low. However, the optical efficiency is very low.

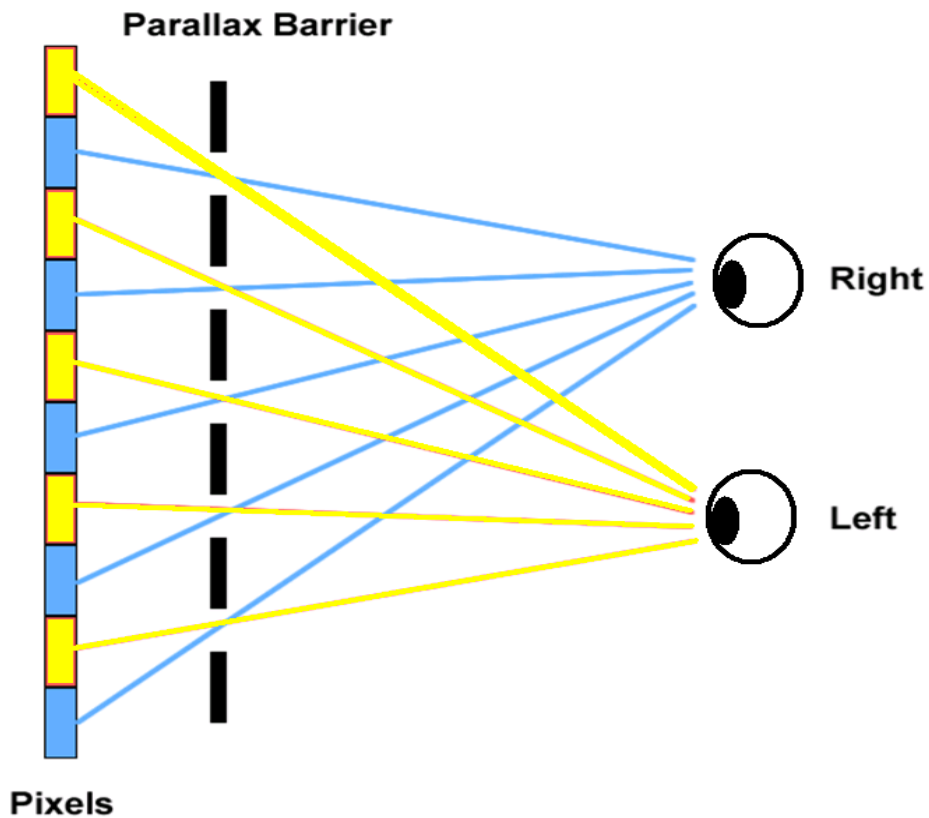


Fig. 6.6 Working principle of autostereoscopic displays based on parallax barrier.

The working principle of autostereoscopic displays based on lenticular lens array is shown in Fig. 6.7. Similar to parallax barrier, lenticular lenses redirect the light from the left and

right pixels. Since no light is absorbed, the optical efficiency is greatly enhanced.

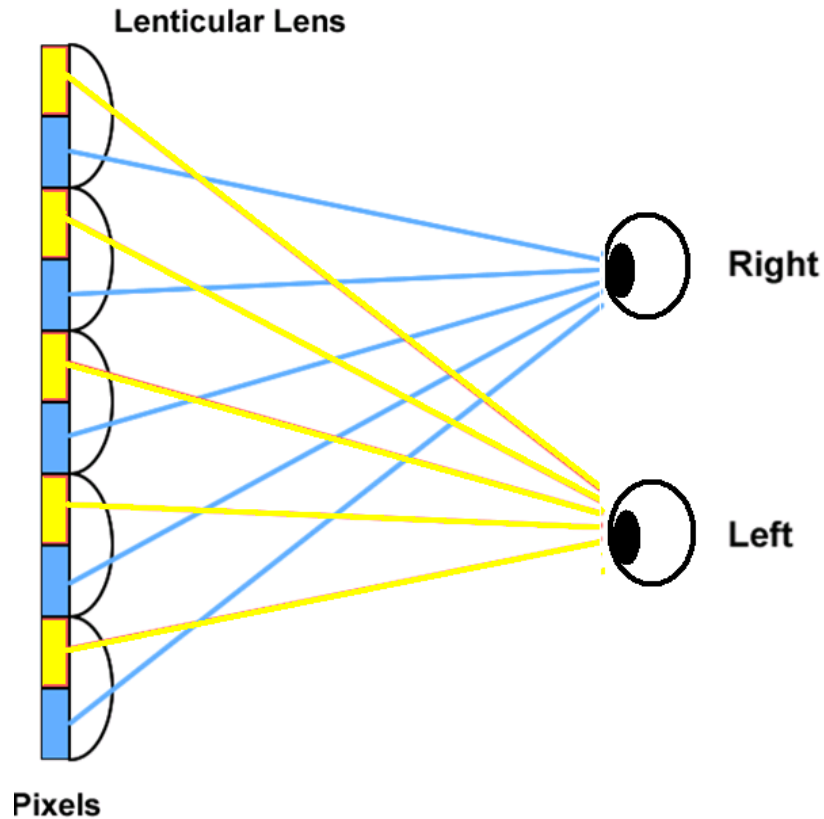


Fig. 6.7 Working principle of autostereoscopic displays based on lenticular lens array.

### 6.1.6 Summary

Among all the stereoscopic 3D technologies mentioned above, the mainstream for glass type displays are those based on polarizing glasses and shutter glasses. Besides the inconvenience of wearing a pair of glasses, both of them have low optical efficiency compared to 2D displays (~50%). For glasses-free 3D technologies, the parallax barrier structure also dramatically reduces the optical efficiency. The autostereoscopic display based on lenticular lens could realize glasses-free 3D image display without any sacrifice of light intensity, thus is most promising for next-generation high-efficiency 3D displays.

## 6.2 Integral Imaging 3D Displays

Integral imaging is an autostereoscopic 3D display [48]. But different from the stereoscopic 3D technologies mentioned above, integral imaging is a real 3D display. Real or virtual images are formed in front of the display. There are two separate processes for acquisition and visualization of the objects: pickup and image reconstruction.

As shown in Fig. 6.8, a 3D object is placed in front of the image sensor and lens array. Each lens transforms the light from the object in a unique way, and projects it onto a certain area of the image sensor. The projected image from each lens is a 2D elemental image and is a function of the lens's focal length and position. With the multipoint pickup configuration, both intensity and direction of rays from the 3D object can be recorded on the image sensor.

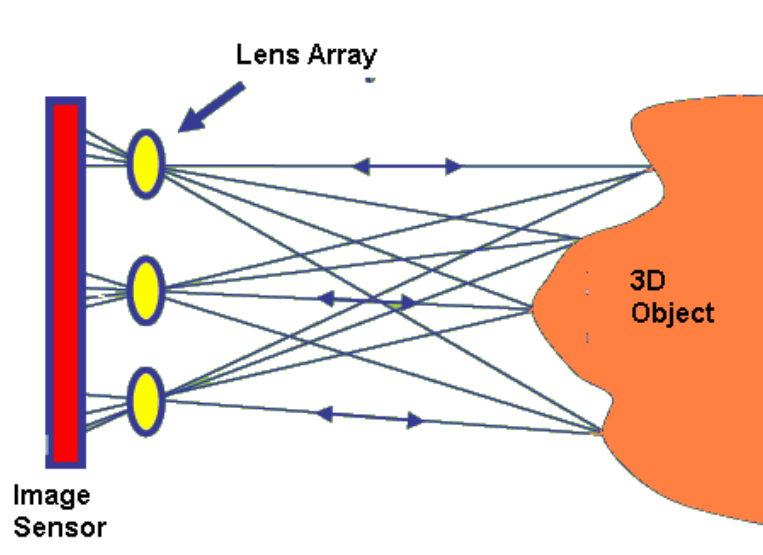
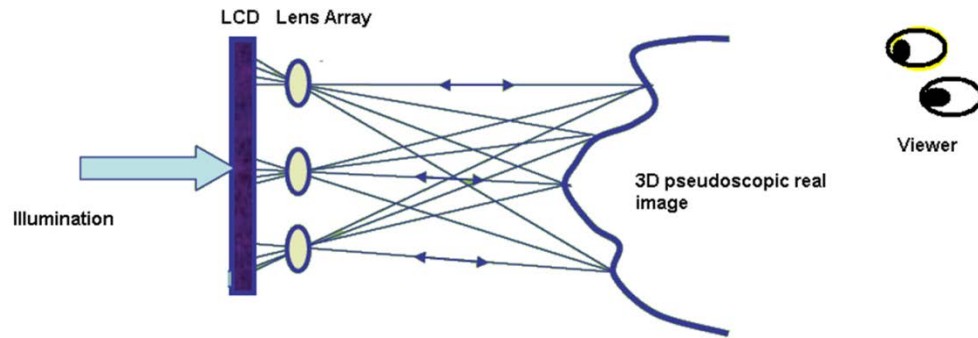


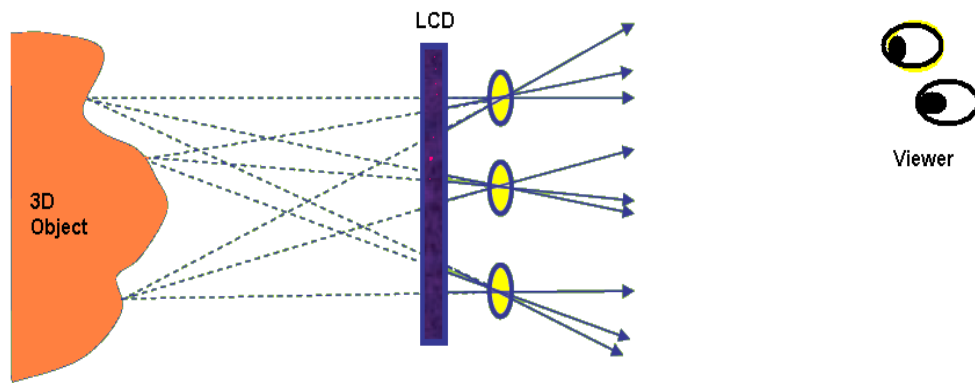
Fig. 6.8 The process of pickup.

Fig. 6.9 shows the process of image reconstruction. In Fig. 6.9(a), a 2D LCD displays the recorded image onto the focal plane of the lens array. Each elemental image is optically relayed by its corresponding lens back into a 3D real image. However, to the viewer the depth

information is inverted as Fig. 6.9(a) shows. A conversion is required where each elemental image is rotated by  $180^\circ$  around its center point. In this way, a virtual image with correct depth information is formed behind the panel as shown in Fig. 6.9(b).



(a)



(b)

Fig. 6.9 The process of image reconstruction (a) pseudoscopic image (b)

orthoscopic image

For conventional integral imaging system where the focal length of the lens array is fixed, there is a tradeoff between the viewing angle and the depth range of the displayed 3D images.

The viewing angle is determined by the angular range of the ray reconstruction, which is inversely proportional to the  $f$ -number of the individual lens in the array. On the contrary, the depth range is determined by the depth of focus of the reconstructed ray and is proportional to the  $f$ -number. As a result, it is not possible to achieve both wide view and large depth range simultaneously.

In order to increase the depth range beyond the limitation, several methods have been proposed. In one approach [49], the focal plane of the lens array is located at infinity so that the depth range is enlarged, but the resolution is decreased significantly. Another method varies the gap between the lens array and the display panel dynamically to change the location of the central-depth plane continuously [50], but it requires rapid mechanical movement of the lens array and causes air resistance and noises. Another method involving a multilayered display device has been reported [51]. By overlaying multiple display panels or electrically controllable screens with a projection system, multiple central-depth planes are generated for depth range enhancement. However, the quality of the displayed 3D image deteriorates quickly as the number of elemental image layers increases.

Recently, an integral imaging system [52] based on variable focus lens array has been proposed. By controlling the focal length of each individual lens, the system could be optimized for multiple objects at the same time. As a result, high resolution images with large image depth range could be achieved. However, when the objects change quickly as in a 3D video, the lenses need to be adapted rapidly at video rate to form the correct central depth plane for each frame. Therefore, fast switching lens array is needed.

### 6.3 BPLC Adaptive Lenses

Adaptive liquid crystal lens is attractive because of its lightweight, compactness and low power consumption. The basic operation principle of an LC lens is to generate gradient refractive index profile across the LC layer [53-57]. However, for a conventional nematic LC lens the response is very slow due to its large coherent length. Moreover, most adaptive LC lenses are polarization dependent, which only works for the extraordinary wave and does not work for the ordinary wave. For a self-emissive display (e.g., OLED or plasma) in which the emitted light is randomly polarized, a polarizer is required to be placed between the display panel and the lens array. As a result, 50% of the optical energy is lost.

BPLC has an intrinsic fast response time due to its short coherent length, therefore, is very promising for the high-efficiency and fast-switching adaptive lenses to satisfy the requirement of integral imaging. Moreover, it is possible to make the BPLC lens polarization independent, which would double the optical efficiency for a randomly polarized emissive display panel. Also because the BPLC does not require any molecular alignment layer, the shape of lens could be more freely designed.

A hole-patterned microlens using a polymer-stabilized BPLC has been recently demonstrated experimentally [58]. It offers several attractive features, such as fast response time and no need for a polarizer. In the voltage-off state ( $V=0$ ), macroscopically, the BPLC appears optically isotropic so that the refractive index is uniform, resulting in zero optical power. When a voltage is applied across the top aluminum electrode (with a hole in the center as the aperture) and the bottom planar ITO (indium tin oxide) electrode, inhomogeneous electric fields are generated along the lens radius. Because the LC refractive index is spatially modulated by the



electric fields, a lens profile is obtained. However, the performance of this lens could still be improved. For instance, this lens has a compromised image quality due to non-ideal shape of the refractive index profile, and the two orthogonal polarizations ( $o$ - and  $e$ - waves) will have a slightly different focal length because of the strong horizontal electric fields near the edge of the hole.

In this section, we propose several adaptive microlens structures using a polymer-stabilized BPLC. The lenses are polarization independent, have good image quality and fast response time.

### **6.3.1 BPLC Adaptive Lens with A Curved ITO Electrode**

#### **6.3.1.1 Device Configuration**

Fig. 6.10 shows the side-view ( $x$ - $z$  plane) of the proposed microlens array[59]. It consists of two glass substrates. The top glass substrate has microlens array structure, which could be concave or convex. A transparent ITO electrode is coated on the inner surface of the top substrate and then flattened by a polymer layer. The bottom substrate has a planar ITO electrode on the inner side. Sandwiched between these two substrates is a polymer-stabilized BPLC with a thickness of  $d_{LC}$ . The thickness of the polymer layer at the center of the lens is  $d_1$ , and that at the edge is  $d_2$ ; and the aperture radius of each individual microlens in the  $x$ - $y$  plane is  $R$ .

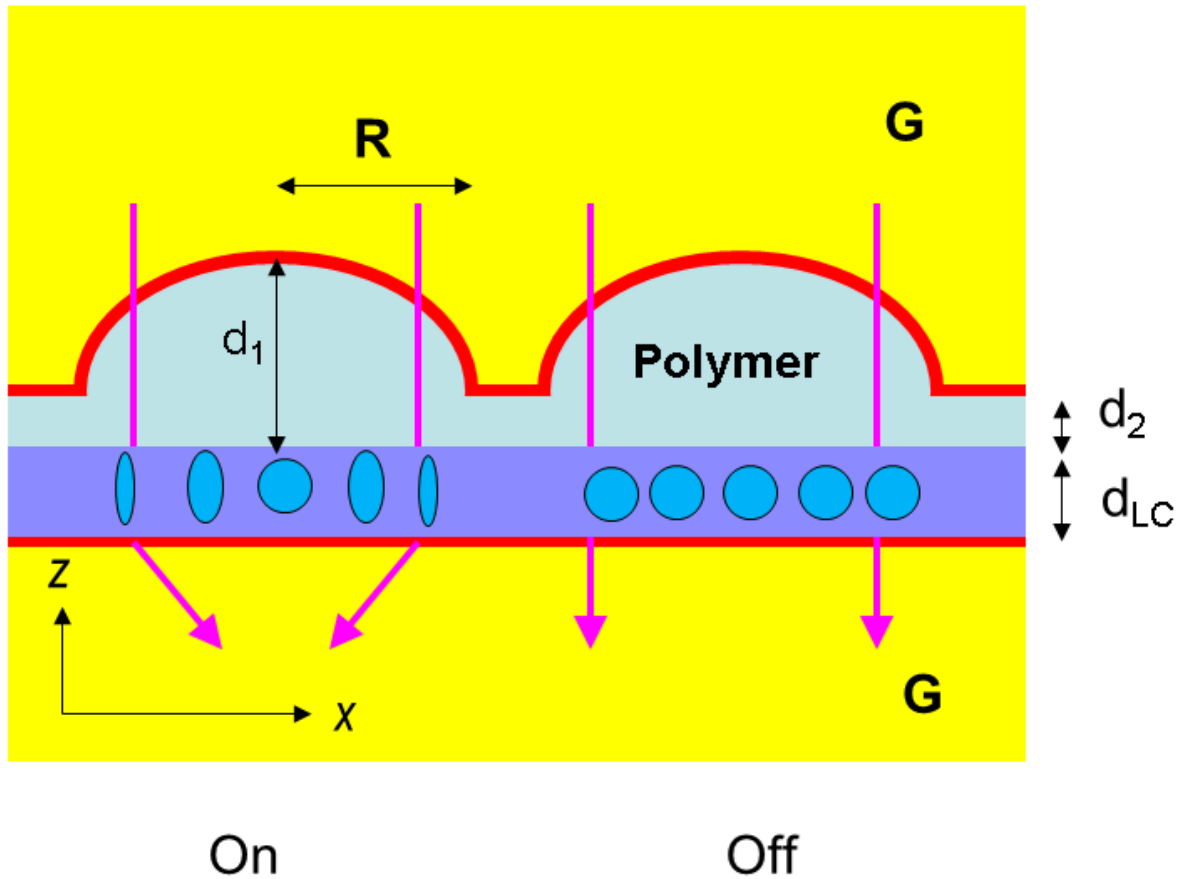


Fig. 6.10 Side-view of the BPLC adaptive lens with a curved ITO electrode.

The pink lines in Fig. 6.10 denote the generic beam path, in which the refraction between the top glass and polymer interface is neglected. At  $V=0$ , the BPLC is optically isotropic and does not contribute to the optical power. As the applied voltage increases, vertical electric fields are generated in the BPLC layer and birefringence induced.

If the electric fields are perfectly vertical, the normally incident light only experiences an ordinary refractive index which depends on  $E$  as

$$n_o(E) \approx n_i - \Delta n_{ind}(E) / 3, \quad (6-1)$$

regardless of polarization. A structure with concave top glass substrate as Fig. 6.10 shows, the electric field in the lens center is weaker than that near the edges because of the longer distance between top and bottom electrodes. As a result, the induced birefringence  $\Delta n_{\text{ind}}$  is smaller (i.e.,  $n_o$  is larger) in the center than that in the edges. So the phase profile over the aperture is like a positive lens. On the other hand, if the top glass substrate is convex, a tunable negative focal length could be achieved. By varying the voltage, the focal length of the LC layer could be tuned continuously. The focal length can be expressed as [58]:

$$f_{LC} = R^2 / 2\delta n(E)d_{LC}, \quad (6-2)$$

where  $\delta n(E)$  is the index difference between the lens' center and edge. If the indices of polymer ( $n_p$ ) and glass ( $n_g$ ) do not match, there will be an initial focal length:

$$f_{in} = r_C / (n_p - n_g), \quad (6-3)$$

where  $r_C$  is the radius of curvature in the center of the lens. This  $f_{in}$  could be positive or negative depending on the index difference and the shape of top ITO [57]. Therefore, the total focal length ( $f_t$ ) which can be found from:

$$1/f_t = 1/f_{in} + 1/f_{LC}. \quad (6-4)$$

So  $f_t$  would change sign as  $f_{LC}$  is tuned. This BPLC lens, similar to other nematic LC lenses, still has chromatic aberration because of the LC refractive index dispersion [60]. But, with the additional polymer layer, the chromatic aberration could be reduced by choosing LC, polymer, and glass to have similar dispersive properties.

### 6.3.1.2 Simulation results

We assume the BPLC has a saturated birefringence  $\Delta n_s \sim 0.2$  (at  $\lambda = 633$  nm), saturation electric field  $E_s \sim 5.6$  V/ $\mu\text{m}$ , and Kerr constant  $K \approx \Delta n_s / \lambda E_s^2 = 10$  nm/V<sup>2</sup> [17]. In our design,  $R = 225$   $\mu\text{m}$ ,  $d_1 = 76$   $\mu\text{m}$ ,  $d_2 = 2$   $\mu\text{m}$ , and  $d_{LC} = 17$   $\mu\text{m}$ . For simplicity we assume the index between the glass and polymer is matched, and therefore  $f_i = f_{LC}$ . In reality, the  $E$  fields are not perfectly vertical due to the potential gradient, so  $o$ -wave sees  $n_o$ , and  $e$ -wave sees  $n_{eff}$ . Since the vertical  $E$  field component dominates,  $n_{eff}$  is also very close to  $n_o$ . The performances of two different polarizations would be discussed later.

For the structure where the top substrate is spherical and concave as in Fig. 6.10, we calculate the phase profile across the lens for  $o$ - and  $e$ - waves. For comparison purpose, a similar structure using hole-patterned electrode [58] is also calculated with  $d_{LC} = 17$   $\mu\text{m}$  and aperture radius  $R = 225$   $\mu\text{m}$ . Fig. 6.11 depicts the relative phase profiles of both structures at  $V = 100$  V<sub>rms</sub>. The phase at the center of each microlens is offset to be zero for easy reading. The blue solid curve and red dashed curve represent  $o$ - and  $e$ - polarization in the proposed microlens array respectively, while the black and green curves represent  $o$ - and  $e$ - for the hole-patterned microlens array respectively.

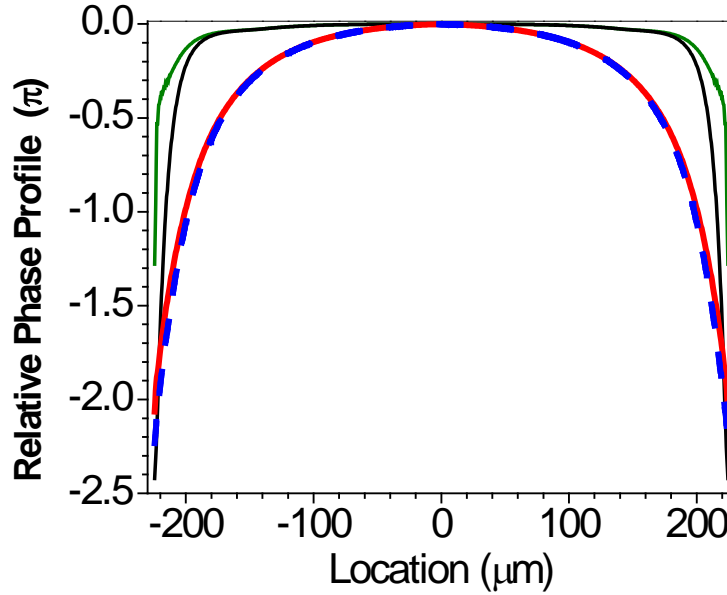


Fig. 6.11 Simulated phase profiles across the lens at  $V=100 V_{\text{rms}}$  for  $o$ - and  $e$ - waves in the proposed microlens array (red and blue) and hole-patterned microlens array (green and black).

In comparison to the hole-patterned microlens structure, our design exhibits following advantages:

1. For a given voltage (say,  $100 V_{\text{rms}}$ ), our microlens array has a larger relative phase, resulting in a shorter focal length. This is because in the hole-patterned design, the aperture area has no top electrode and the electric fields decrease very quickly as the radius decreases. For instance, the relative phase at the radius of  $150 \mu\text{m}$  is only about 1/10 of that at the edge of the lens. However, in our design the electric fields are generated between top and bottom ITO electrodes across the whole aperture, and the intensity of fields is utilized effectively. This indicates that our design has a lower operating voltage to achieve the same

phase change than the hole-patterned structure.

2. In the hole-patterned structure, *o*- and *e*- polarizations make a noticeable difference near the edge. This undesirable polarization dependence is due to the strong horizontal field components near the edge of top aluminum electrode. The horizontal electric field component would generate birefringence in the horizontal direction. Thus, one polarization would experience an increased refractive index  $n_e(E) \approx n_i + 2\Delta n_{ind}(E)/3$ , while the other a decreased index  $n_o(E) \approx n_i - \Delta n_{ind}(E)/3$ . As a result, the *o*- wave will have a larger phase change, i.e., shorter focal length than the *e*- wave. In our design, although curved electric fields still exist near the top ITO electrode due to its curved shape, the polymer layer shields most of the horizontal components. With the electric fields almost vertical in the BPLC layer, both *o*- and *e*- polarizations experience a very similar index  $n_o(E) \approx n_i - \Delta n_{ind}(E)/3$ , and the polarization dependency is suppressed substantially.
3. Last but not least, the shape of the phase profile could be precisely controlled in our design by the shape of the top ITO. Fig. 6.12(a), (b) and (c) depict three structures with different ITO shapes; and Fig. 6.12(d) compares their phase profiles at 100 V<sub>rms</sub> with a perfect parabolic shape (blue curve). Fig. 6.12(a) shows a structure with spherical top ITO as we discussed previously; Fig. 6.12(b) depicts a structure with a cone-shape (or triangle from side view) top ITO electrode; and Fig. 6.12(c) has an Eiffel-Tower-like top ITO electrode. The center polymer thickness  $d_1$ , edge polymer thickness  $d_2$ , LC cell gap  $d_{LC}$  and aperture radius  $R$  are all kept the same as in the previous calculations ( $R=225 \mu\text{m}$ ,  $d_1=76 \mu\text{m}$ ,  $d_2=2 \mu\text{m}$ , and  $d_{LC}=17 \mu\text{m}$ ). Since the device is polarization independent, we only plot one polarization in Fig. 6.12 Effect of top substrate shape on the generated phase profile. (a), (b)

and (c) are structures with different top ITO shapes. (d) The simulated phase profiles: black line for structure (a), green for structure (b), red line for structure (c), and blue dashed lines for an ideal parabolic shape. (d) for easy reading. As shown in Fig. 6.12(d), the structure in Fig. 6.12(c) has more desirable phase profile than the other two, because a parabolic phase profile is helpful for suppressing spherical aberration which in turn improves the image quality.

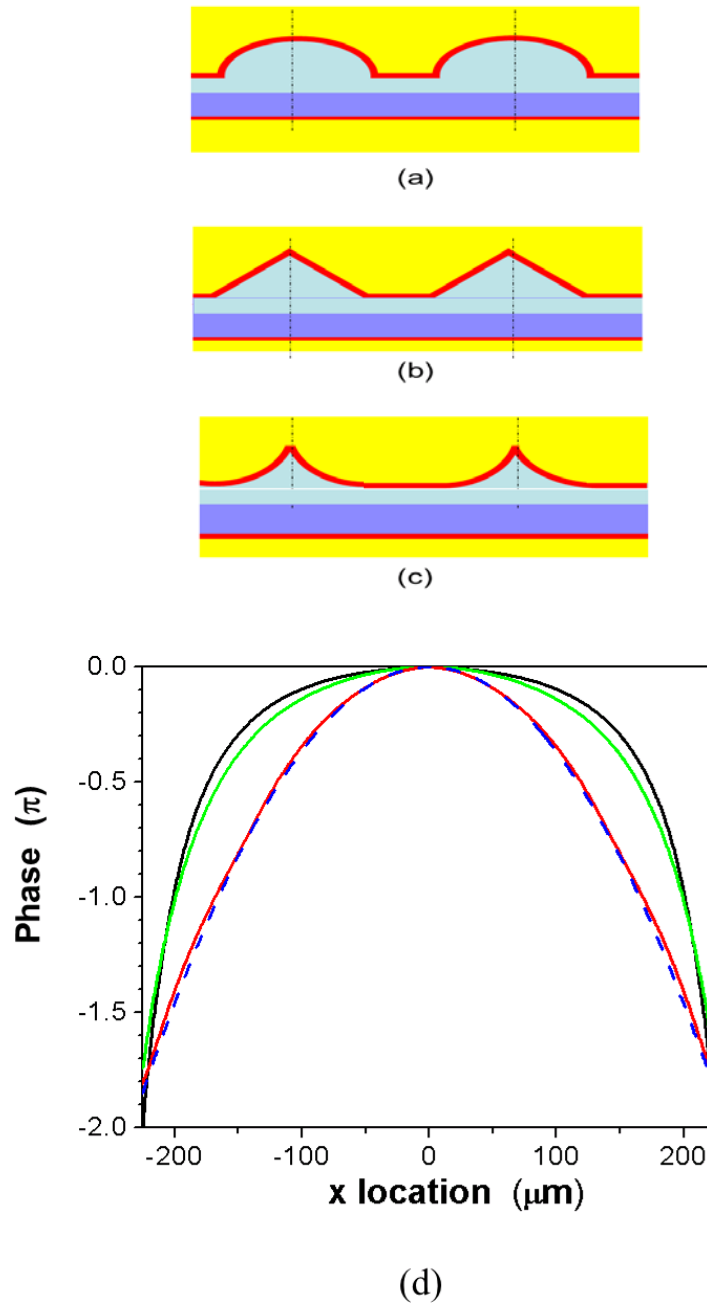


Fig. 6.12 Effect of top substrate shape on the generated phase profile. (a), (b) and (c) are structures with different top ITO shapes. (d) The simulated phase profiles: black line for structure (a), green for structure (b), red line for structure (c), and blue dashed lines for an ideal parabolic shape.



Here, we briefly describe the procedures how we obtain the device structure shown in Fig. 6.12(c). In the low field region, extended Kerr Effect is reduced to Kerr Effect as Eq. (1-3).

In order to have a parabolic phase profile along the radius, the refractive index difference  $\delta n(r)$  should be proportional to  $r^2$ , where  $r$  is the distance to the center of the lens. Under such a circumstance, we can write

$$\delta n(r) = \rho r^2 = n_i(r) - n_o(r) \approx \Delta n_{ind}(E) / 3 = \lambda K V^2 / 3 d^2(r), \quad (6-5)$$

where  $\rho$  is a scaling parameter, and each  $\rho$  corresponds to a certain focal length,  $V$  is the applied voltage across the electrodes, and  $d(r)$  is the vertical distance between top and bottom electrode at a specific radius  $r$ . From Eq. (6-5), we find

$$d(r) = \sqrt{\lambda K / 3 \rho} (V / r). \quad (6-6)$$

And accordingly, the shape of the top ITO is obtained. When high fields are involved, the calculation is more complicated. But for each operating voltage, the ITO shape could always be calculated. By optimizing our design at 100 V<sub>rms</sub>, we have kept the phase profile almost parabolic from 12 V<sub>rms</sub> to 100 V<sub>rms</sub>. However, for such a structure it is preferred that polymer and glass have the same refractive index. Otherwise, aberrations and total internal reflection might be introduced by the curved polymer-glass interface.

Fig. 6.13 is a plot of the voltage-dependent focal length for the structure in Fig. 6.12(c). The blue curve is for *o*-polarization, and the red one is for *e*-polarization. As the voltage varies, the focal length of *o*- and *e*-polarization keeps the same, which further proves that this design is indeed polarization independent. As expected, the focal length gets shorter as the voltage increases. At 100 V<sub>rms</sub>, a 4-cm focal length is obtained. In the low voltage region, the change of

focal length is more dramatic, while in the high voltage region the slope becomes flatter. The primary reason is that the focal length  $f$  is inversely proportional to the phase change as described in Eq. (6-2), and the secondary reason is that the induced birefringence gradually saturates at high fields.

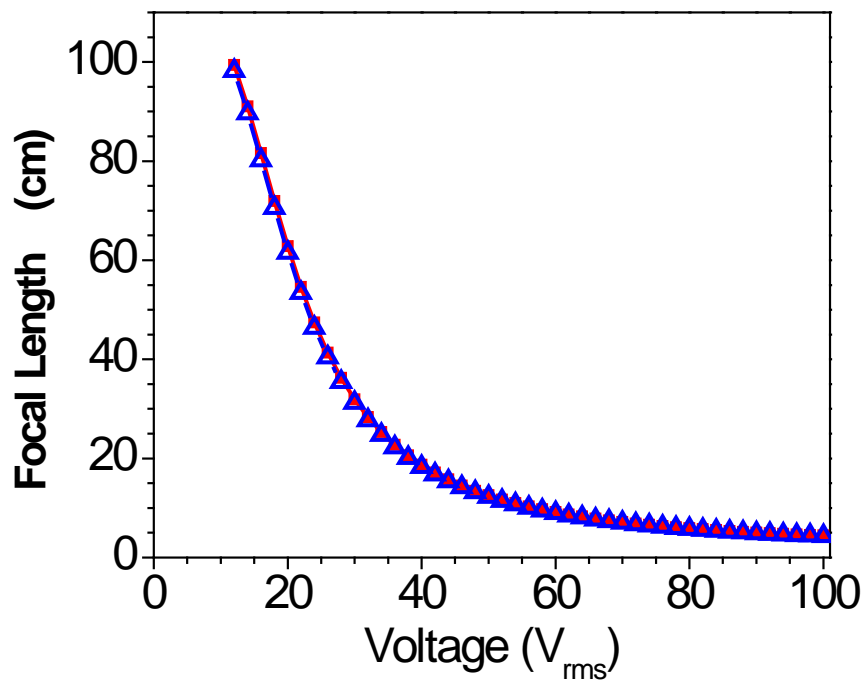


Fig. 6.13 Simulated voltage dependent focal length of the proposed BPLC microlens.

### 6.3.1.3 Conclusion

We have proposed a fast-response and polarization-independent microlens array using a polymer-stabilized BPLC. By varying the applied voltage from 0 to 100  $V_{rms}$ , the focal length of the LC layer could be continuously tuned from  $\infty$  to 4 cm. If there is index mismatch between the employed polymer and glass, an initial optical power would exist, and the focal length of the

whole system could be tuned from negative to positive (or from positive to negative). By optimizing the shape of top ITO electrode, a parabolic phase profile is obtained, which is desirable for achieving high image quality. Simulation results show that our device is indeed polarization independent, and has a lower operating voltage and better profile shape than the previously reported hole-patterned structure. Such a device would be very attractive for display and photonics applications.

### 6.3.2 BPLC Adaptive Lens with Multiple Electrodes

Although the previous BPLC lens has achieved superb performances, such as fast response, polarization independency and good image quality, the fabrication of the curved ITO electrode is difficult. In this section we proposed a second BPLC lens using planar electrodes, which greatly simplified the fabrication process [61].

#### 6.3.2.1 Device configuration

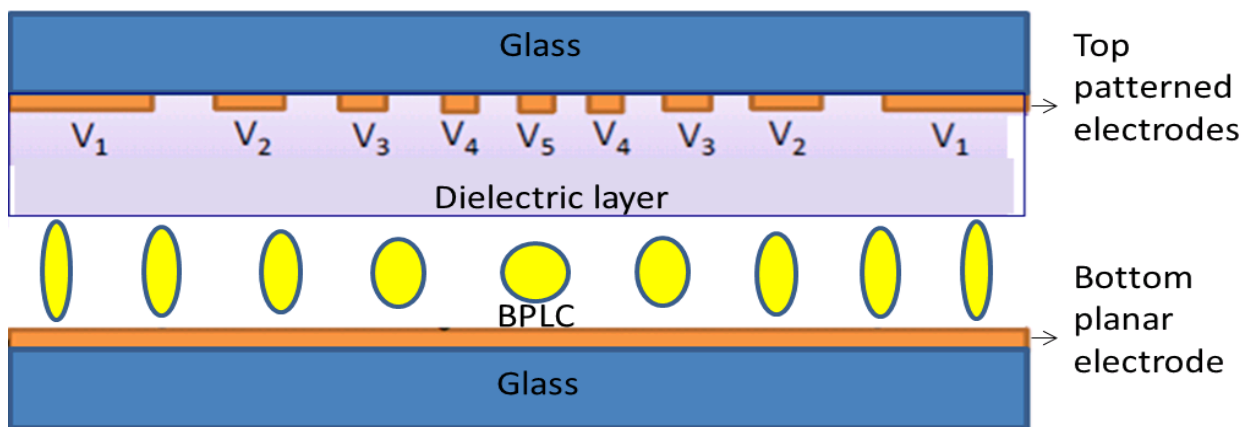


Fig. 6.14 Device configuration of the BPLC adaptive lens with multiple electrodes.

Fig. 6.14 shows the device configuration of the BPLC. On the inner surface of top glass substrate, there are several patterned ITO electrodes with different width. The electrodes would further be flattened by a dielectric layer. On the inner surface of the bottom glass, there is a planar ITO electrode. Different voltages would be applied to the top patterned electrodes, therefore, non-uniform electric fields are generated across the lens. By varying the voltage of top ITO electrodes, the induced birefringence and phase distribution can be precisely controlled. The purpose of the dielectric layer is to smooth the phase profile. But we have to use a large dielectric constant ( $\epsilon=120$ ) layer to suppress voltage shielding.

#### 6.3.2.2 Simulation Results

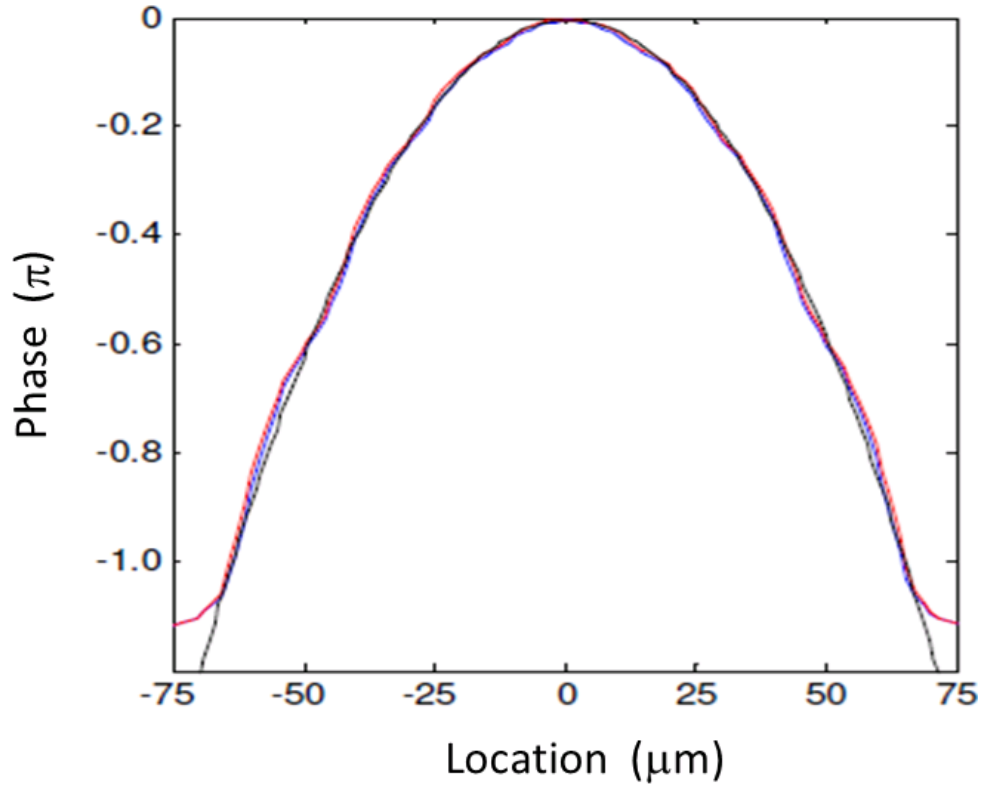


Fig. 6.15 Phase profile of the BPLC adaptive lens with multiple electrodes when  $V_1=65 V_{\text{rms}}$ ,  $V_2=38.2 V_{\text{rms}}$ ,  $V_3=22.3 V_{\text{rms}}$ ,  $V_4=11 V_{\text{rms}}$ ,  $V_5=1.05 V_{\text{rms}}$  and the bottom electrode is grounded. Blue—*o*- wave, red—*e*- wave and black—ideal parabolic shape.

We use commercial software Techwiz (Sanayi, Korea) to compute the electric potential distribution and then calculate the optical properties. We assume the BPLC has  $\Delta n_s \sim 0.2$  (at  $\lambda = 550 \text{ nm}$ ),  $E_s \sim 5.6 \text{ V}/\mu\text{m}$ , and Kerr constant  $K \approx \Delta n_s / \lambda E_s^2 = 11.5 \text{ nm}/\text{V}^2$ . Fig. 6.15 shows the phase profile of the lens with  $V_1=65 V_{\text{rms}}$ ,  $V_2=38.2 V_{\text{rms}}$ ,  $V_3=22.3 V_{\text{rms}}$ ,  $V_4=11 V_{\text{rms}}$ ,  $V_5=1.05 V_{\text{rms}}$  and bottom electrode grounded. The cell gap of BPLC is  $6 \mu\text{m}$ , the thickness of dielectric layer  $9 \mu\text{m}$ , and the aperture diameter of the lens  $180 \mu\text{m}$ . The blue line represents the phase profile for *o*-

wave, red one for the  $e$ - wave and black one for the ideal parabolic shape. You can see that about  $1\pi$  phase difference is achieved between the center and the edge of the lens. Due to the potential gradient, the electric field is not perfectly vertical so that the  $o$ -wave and  $e$ -wave have a very small difference in their phase profiles. As shown in Fig. 6.15,  $o$ - (blue curve) and  $e$ - (red curve) overlap very well, which means it is polarization independent. Both polarizations match very well with the ideal parabolic shape (black curve), within  $\pm 10\%$  tolerance.

By varying the voltages on the top patterned ITO electrodes, we can always control the phase profile to be approximately parabolic. Fig. 6.16 show the focal length of the lens at different voltages, as you can see it can reach  $\sim 10\text{mm}$  when the highest voltage on the top electrodes is  $65\text{ V}_{\text{rms}}$ .

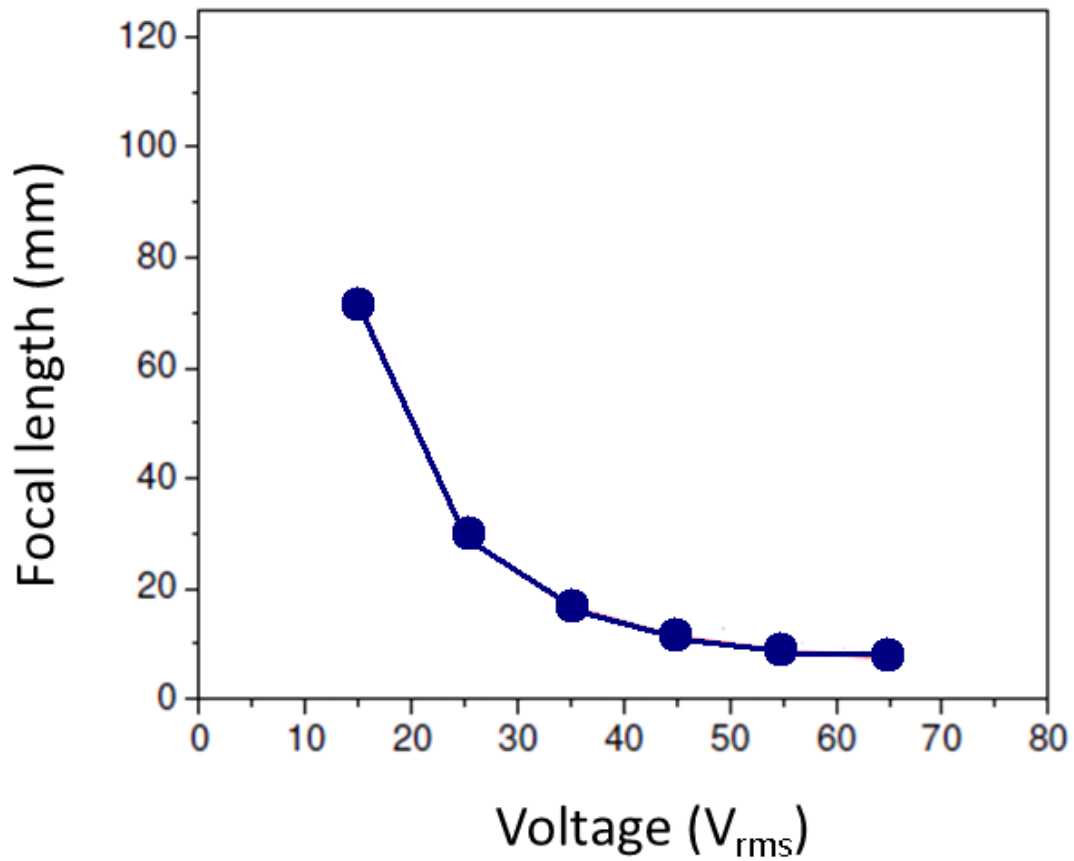


Fig. 6.16 Focal length of the proposed BPLC lens at different voltages.

### 6.3.3 BPLC Adaptive Lens with A Resistive Electrode

In this section, we propose a new cylindrical microlens using a polymer-stabilized BPLC [62]. It has a simple structure consisting of a planar resistive electrode on the top substrate and a planar ITO electrode on the bottom substrate. A parabolic phase profile is obtained in low field region due to the linear Kerr effect in the BPLC layer with only one data addressing. This design has a larger optical power compared to the two BPLC lenses mentioned previously in this chapter, because there is no shielding effect from any dielectric layer. Simulation results show that this simple device is polarization independent and it has parabolic-like phase profile in a

large tuning range.

### 6.3.3.1 Device Configuration

Fig. 6.17 shows the side view of our proposed cylindrical BPLC lens. On the inner surface of top substrate, there is a center ITO electrode strip at the center of the lens, and two ITO electrode strips on the two edges respectively. The aperture of the lens is further coated with a thin transparent high-resistive film. On the inner surface of the bottom substrate, a planar ITO electrode is coated. The radius of aperture is  $R$ , and the cell gap of BPLC layer is  $d_{LC}$ .

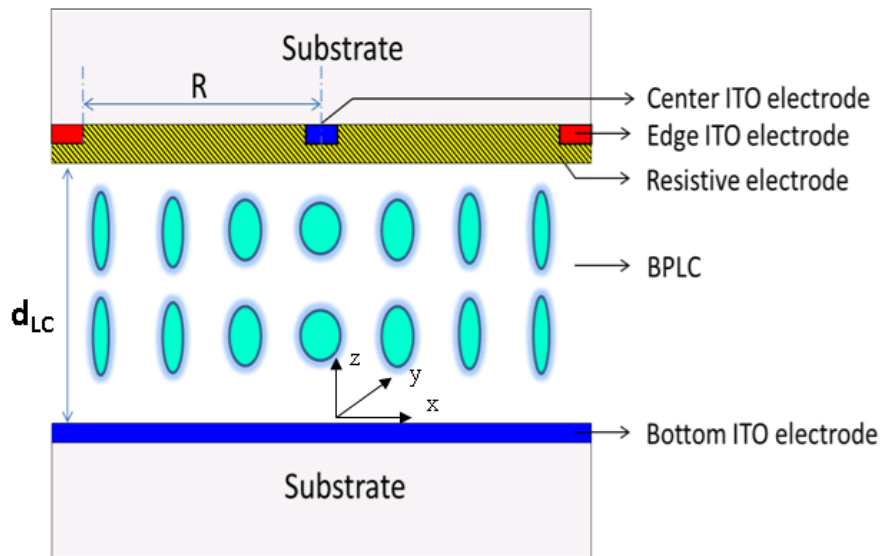


Fig. 6.17 Side view of the proposed cylindrical BPLC lens.

In our design, we ground the center ITO strip ( $x \approx 0$ ) and bottom ITO electrode, but vary the voltage ( $V_0$ ) on the edge ITO strip ( $x \approx R$ ). When  $V_0=0$ , there is no electric field and the BPLC remains optically isotropic. For the normally incident light, any polarization experiences  $n_{iso}$  at any radius. Thus, there is no optical power.



When  $V_0 > 0$ , we could obtain a differential equation for the potential distribution on the resistive film [63]:

$$\nabla^2 V = \frac{\rho_R \omega \varepsilon' j}{d_R d_{LC}} V + \frac{\rho_R \omega \varepsilon''}{d_R d_{LC}} V, \quad (6-7)$$

where  $\rho_R$  is the resistivity of the resistive film,  $d_R$  and  $d_{LC}$  are the thicknesses of the resistive film and LC, respectively,  $\omega$  is the AC frequency, and  $\varepsilon'$  and  $\varepsilon''$  are the real and imaginary parts of LC dielectric constants. Since the aperture dimension is much larger than the resistive film thickness, and it is a cylindrical lens, the electric field in  $x$  direction is much larger than those in other two directions within the resistive film. Combining the boundary condition  $V|_{x=0} = 0$ , Eq. (6-7) has an approximate solution:

$$V = a [\exp(\sqrt{c} \exp((\frac{\pi}{4} - \frac{\theta}{2})j)x) - \exp(-\sqrt{c} \exp((\frac{\pi}{4} - \frac{\theta}{2})j)x)], \quad (6-8)$$

where  $a$  is a positive real constant,  $\frac{\rho_R \omega |\varepsilon^*|}{d_R d_{LC}}$ ,  $\varepsilon^* = \varepsilon' - \varepsilon'' j = |\varepsilon^*| \exp(-j\theta)$  and  $\theta$  the phase delay between  $\varepsilon''$  and  $\varepsilon'$ .

When  $\sqrt{c} |x| \ll 1$ , using Taylor expansion, the amplitude of potential distribution can be approximated as:

$$V \approx 2a\sqrt{c} |x|, \quad (6-9)$$

here we have  $\rho_R = 0.01 \Omega \cdot m$  (a typical value of Poly (3,4-ethylenedioxythiophene) resistive film),  $\omega = 200\pi \text{ rad/s}$ ,  $d_R \sim 30 \text{ nm}$ ,  $d_{LC} \sim 10 \mu\text{m}$ ,  $\varepsilon' = 53 \varepsilon_0$ ,  $\varepsilon'' = 3.18 \varepsilon_0$ ,  $\varepsilon_0 = 8.85 \times 10^{-12}$ , and  $|x| \leq R = 100 \mu\text{m}$ . Then  $\sqrt{c} |x| \leq 0.0087 \ll 1$ , and linear potential distribution condition is fulfilled, and the potential

could be expressed as:

$$V = \frac{|x|}{R} V_0. \quad (6-10)$$

As a result, vertical electric fields with gradient intensity are generated across the lens and so is induced birefringence  $\Delta n_{\text{ind}}$ . For a normally incident light, *o*- wave and *e*- wave see a very similar refractive index  $n_o = n_{\text{iso}} - \Delta n_{\text{ind}}/3$  [21], which is also radius dependent. Near the center of the lens, the electric fields are weaker due to smaller voltage difference between top and bottom electrodes, thus the induced birefringence  $\Delta n_{\text{ind}}$  is smaller and  $n_o$  is larger. On the other hand, near the edge of the lens, the induced birefringence is larger and  $n_o$  is smaller. Therefore, a phase profile with positive lens is formed.

At low field region, the induced birefringence follows Kerr effect as described by Eq. (1-3) [14]. At radius  $r$ , considering the linear potential distribution in Eq. (6-10), the induced birefringence could be further expressed as:

$$\Delta n_{\text{ind}} = \lambda K E^2 = \lambda K \frac{V^2}{d_{LC}^2} = \lambda K \frac{V_0^2}{d_{LC}^2 R^2} x^2. \quad (6-11)$$

Eq. (6-11) is a parabolic function with respect to location  $x$ . Consequently, the phase  $\Phi(x) = 2\pi d_{LC} n_o / \lambda = 2\pi d_{LC} [(n_{\text{iso}} - \Delta n_{\text{ind}} / 3)] / \lambda$  would also have a parabolic shape. With such a simple structure we could obtain parabolic phase profile easily.

However, as the electric field further increases, the induced birefringence would gradually saturate according to the extended Kerr effect [17]. Therefore, the phase profile would deviate from the ideal parabolic shape in the high field region.

### 6.3.3.2 Simulation Results

In order to validate the device concept, we carried out simulations using finite-difference frequency-domain method. We use the linear gradient potential on the resistive film as the boundary condition for BPLC cell. We first calculated the electric field distribution in the LC layer and then get the induced birefringence based on extended Kerr model as shown in Eq. (1-4) and finally the phase for the  $o$ - and  $e$ - waves. The BPLC we used is Chisso JC-BP01M [21]. It has  $E_s \approx 5.4 \text{ V}/\mu\text{m}$  and  $\Delta n_s \approx 0.14$  at  $\lambda = 633 \text{ nm}$  and room temperature. For practical applications, we are more interested in  $\lambda = 550 \text{ nm}$ . Thus, we extrapolated the  $\Delta n_s$  to  $\lambda = 550 \text{ nm}$  based on the wavelength dispersion model [64] and found  $\Delta n_s \approx 0.1487$ . Since  $E_s$  does not depend on the wavelength, it remains the same.

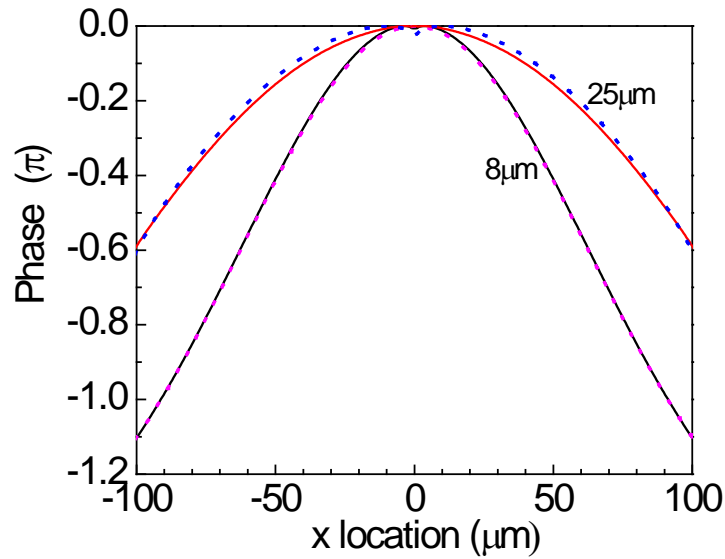


Fig. 6.18 Simulated phase profiles ( $\lambda = 550 \text{ nm}$ ) across the lens for  $o$ - wave (dotted lines) and  $e$ - wave (solid curves) at  $V_o = 50 \text{ V}_{\text{rms}}$ . The upper curve is for  $d = 25 \mu\text{m}$  lens and the lower one is for  $d = 8 \mu\text{m}$ .

Fig. 6.18 shows the simulated phase profiles of the proposed lens structure with different cell gaps at 50 V<sub>rms</sub> operating voltage and  $\lambda=550$  nm. The widths of center and edge ITO strips are both 2  $\mu\text{m}$ , and the aperture radius is 100  $\mu\text{m}$ . The magenta dotted curve and black solid curve represent the phase profiles of *o*- and *e*- waves, respectively, in a structure with  $d=8$   $\mu\text{m}$ ; and the blue dotted curve and red solid curve represent the phase profiles of *o*- and *e*- waves, respectively in a structure with  $d=25$   $\mu\text{m}$ . First of all, at the same applied voltage 50 V<sub>rms</sub>, the 8  $\mu\text{m}$  structure has more than  $1\pi$  phase difference from center to edge, while the 25  $\mu\text{m}$  structure has only  $\approx 0.6\pi$ . Although the 25  $\mu\text{m}$  LC layer would potentially have much larger phase difference at higher voltage, at this specific voltage, its phase is smaller due to the much weaker electric fields. Meanwhile, inside the 8  $\mu\text{m}$  structure, electric fields are so strong that the induced birefringence deviates from the Kerr relation. As a result, the phase profile also deviates from the ideal parabolic shape. In the 25  $\mu\text{m}$  lens cell, the deviation is much smaller so that phase profile is nearly parabolic. For our BPLC lens structure, there is a critical electric field instead of critical voltage, beyond which, the deviation from Kerr effect is so much that the phase profile could not be regarded approximately as parabolic anymore. This critical field is determined by the liquid crystal material. Obviously, a larger cell-gap structure promises a better phase profile at the same voltage.

Secondly, the 8  $\mu\text{m}$  structure has a better overlap between *o*- and *e*- waves. The thinner the cell gap is, the stronger the vertical components of electric fields are, and, relatively, the smaller the horizontal components are. As discussed in 6.3.1, horizontal electric field components are the causes of polarization dependency, since *o*- wave would see a decreased refractive index, while *e*- wave sees an increased one. With a relatively smaller horizontal

component, smaller cell gap is more advantageous for polarization independency. Similarly, a larger aperture would result in a better overlap of the two waves.

So we have chosen an optimized structure with  $d=13 \mu\text{m}$  and  $R=100 \mu\text{m}$ , to have a large optical path length difference, good phase profile shape and polarization independency at the same time. As shown in Fig. 6.19, at  $50 V_{\text{rms}}$  a phase change  $\sim\pi$  is achieved. *O*-wave (red dotted curve) and *e*- wave (black solid curve) overlap with each other very well, indicating the optimized structure is indeed polarization independent. Moreover, they fit with the ideal parabolic shape (green dashed curve) well. Thus, a good image quality could be obtained. Obviously, the lower the operating voltage, the more parabolic-like shape it would form, as shown by the  $30 V_{\text{rms}}$  curves, because the induced birefringence follows Kerr effect better in the low field region.

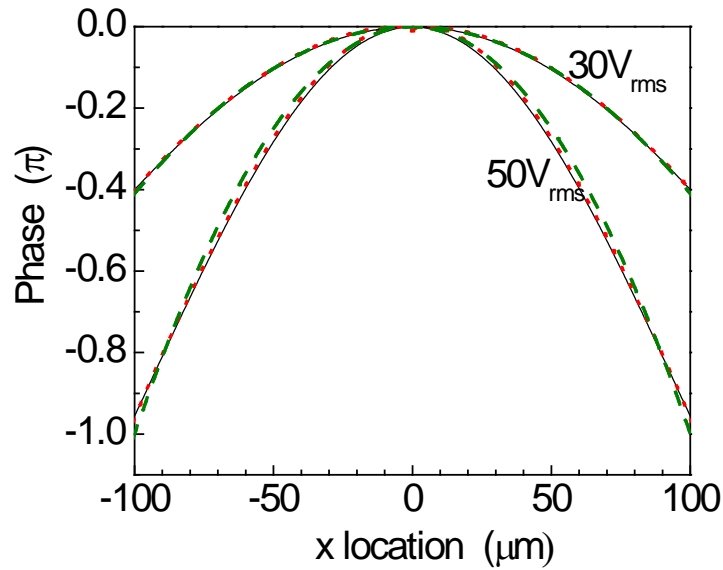
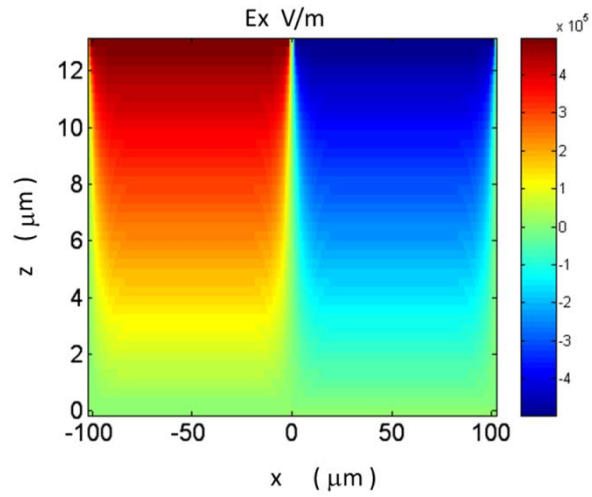
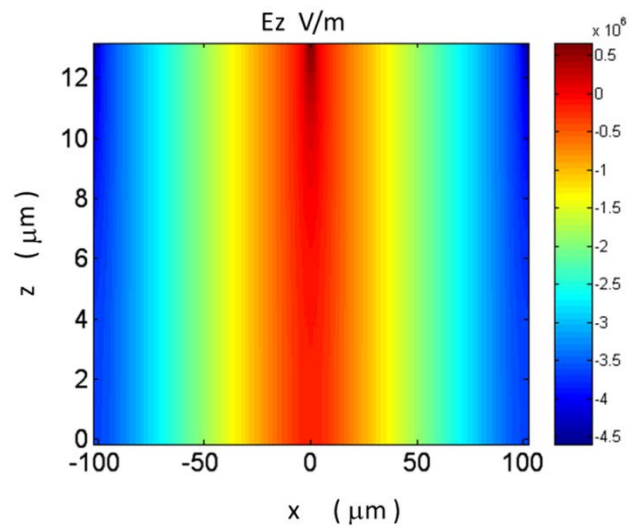


Fig. 6.19 Simulated phase profiles ( $\lambda=550$  nm) across the lens with a  $13 \mu\text{m}$  cell gap at  $30 V_{\text{rms}}$  and  $50 V_{\text{rms}}$ . Red dotted curves are for  $o$ - wave and black solid curves are for  $e$ - wave, and green dashed curves are ideal parabolic curves.

Fig. 6.20 shows electric field distribution across the BPLC lens where  $|E_z|$  is much larger than  $|E_x|$ . That's why the device is polarization independent [59]. To further suppress the difference between the phase profiles of the two polarizations, one could add a dielectric layer beneath the resistive film to shield those horizontal electric fields. From Fig. 6.20, we could see electric fields are below the saturation electric field  $E_s$ . Therefore, it follows Kerr model very well, and consequently the phase profile has a nice parabolic shape.



(a)



(b)

Fig. 6.20 Electric field distribution across the BPLC cylindrical lens with  $13\ \mu\text{m}$  cell gap at  $50\ \text{V}_{\text{rms}}$ , (a) for  $E_x$ , and (b) for  $E_z$ .

Fig. 6.21 shows the simulated voltage dependent focal length for the abovementioned optimized structure. The focal length is calculated using Eq. (6-2).

The black dotted curve is the focal length for  $o$ - wave, and the red solid curve is for  $e$ - wave. As shown in Fig. 6.21, the two waves have the same focal length, which further proves the lens is polarization independent. As voltage increases, the focal length decreases. At 50  $V_{\text{rms}}$ , the simulated focal length is about 18 mm.

A possible extension of present lens structure is to have the edge electrode and bottom electrode grounded, while varying the voltage on the center electrode. Then a negative lens is formed, but the shape of the lens will not be as good as the positive lens.

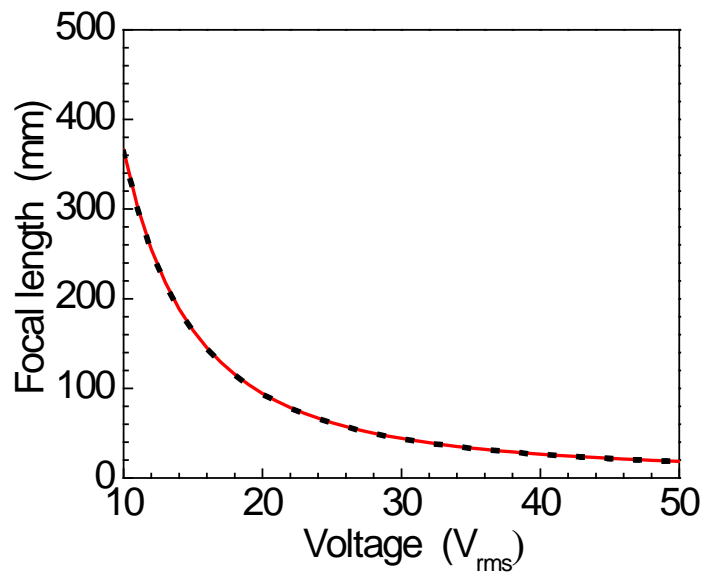


Fig. 6.21 Simulated voltage dependent focal length of the proposed BPLC lens:

black dotted curve is for  $o$ - wave, and red solid curve is for  $e$ - wave.

### 6.3.3.3 Conclusion

We proposed a new polymer-stabilized blue phase lens using a resistive electrode. At low fields, when the induced birefringence follows Kerr effect a parabolic phase profile is formed without any pixelated electrodes. For an optimized structure with cell gap 13  $\mu\text{m}$  and aperture



radius 100  $\mu\text{m}$ , as the applied voltage  $V_o$  is varied from 0 to 50  $V_{\text{rms}}$ , focal length could be continuously tuned from  $\infty$  to 18 mm. And through the whole focal length range, the lens could maintain polarization independent and parabolic shape. Such a device, with only single cell gap, planar electrodes, and single data addressing, is easy to fabricate and would be very attractive for a wide range of applications that need miniaturized autofocus.

#### **6.4 Summary**

In this chapter, we proposed several BPLC adaptive lenses for integral imaging 3D displays. From curved ITO electrode to multi-planar electrode, from multi-planar electrode to simple resistive film electrode, the structure of the BPLC lens is getting simpler and simpler, while all of them have maintained the following attractive features: 1) polarization independency which doubles the optical efficiency of a 3D system using unpolarized display panels; 2) parabolic phase profile, which reduces crosstalk; and 3) fast switching time which provides real time accommodation for 3D videos.

## CHAPTER 7: SUMMARY

In order to alleviate energy crisis, a lot of efforts have been made to explore new energies such as solar energy and wind energy. As a matter of fact, it is equally important to reduce the power consumption of the display devices. Today, LCDs have been widely used in almost every household, occupying a more than 100-billion-dollar market all over the world. Unfortunately, the conventional LCDs' optical efficiency is very low ~5%. Therefore, there is urgent need to improve the efficiency of LCDs.

In this dissertation, we have proposed high-efficiency blue phase LCDs for next generation displays. They have following features: submillisecond response time, alignment layer free, and wide viewing angle.

From Chapter 2 to Chapter 3, we have investigated the material properties of polymer-stabilized BPLC, searching the optimum operating condition and most appropriate material for display applications. In the frequency domain, we have found that increasing electric field frequency would decrease the Kerr constant and increase the operating voltage. A model called *extended Cole-Cole* model is proposed to describe the phenomenon. Therefore, a polymer-stabilized BPLC with a large Kerr constant and a relaxation frequency over 3 kHz is preferred. Inspired by Gerber's equation, we have prepared a polymer-stabilized BPLC with negative Kerr constant using a host with a negative dielectric anisotropy. We have investigated its electro-optic properties and compared them with its positive counterparts. These results set important guidelines for optimizing the blue phase LCDs from material viewpoint.

From Chapter 4 to Chapter 6, we have proposed several approaches to enhance the optical efficiency of blue phase LCDs from device point of view.

Firstly, from the LC cell level we conceived enhanced protrusion electrode and complimentary enhanced protrusion electrode structures for improving the optical efficiency of a blue phase LCD sandwiched between two crossed polarizers. By compensating the dead zones with effective regions, we have successfully improved the transmittance of LC cell to 100%.

Secondly, from the LCD panel level the fast response blue phase LCDs would enable color sequential display and triple the optical efficiency.

Thirdly, from the LCD system level we proposed a transflective blue phase LCD, where ambient light, instead of deteriorating the contrast ratio, serving as a light source. Such displays greatly reduce the optical power while maintaining good performances outdoors.

Last but not least, for 3D displays, which consists of LCD system and additional 3D accessories, we proposed several fast switching blue phase LC adaptive lenses for the most efficient naked-eye 3D display technology—Integral imaging. The lenses are polarization independent, which doubles the optical efficiency for an unpolarized panel such as organic LED; they have parabolic phase profiles for reducing cross talk; and they have fast switching time, which would provide real-time accommodation for 3D videos.

The study covers from materials to devices, from the most basic LC cell to the most complicated system design. We have improved the optical efficiency of blue phase LCDs little by little from different device levels, and we believe this work will make an important impact to next-generation LCDs.

## LIST OF PUBLICATIONS

Journal Publications:

- [1] Y. Li, Y. Liu, Q. Li, and S. T. Wu, “Polarization independent blue-phase cylindrical lens with a resistive film”, *Appl. Opt.* **51**, 2568-2572 (2012).
- [2] Y. Li, Y. Chen, J. Sun, S. T. Wu, S. H. Liu, P. J. Hsieh, K. L. Cheng, and J. W. Shiu “Dielectric dispersion on the Kerr constant of blue phase liquid crystals”, *Appl., Phys. Lett.* **99**, 181126 (2011).
- [3] C. T. Lee, Y. Li, H. Y. Lin and S.T. Wu, “Design of polarization-insensitive multi-electrode GRIN lens with a blue-phase liquid crystal”, *Opt. Express* **19**, 17402-17407 (2011).
- [4] Y. Li and S. T. Wu, “Transmissive and transfective blue-phase LCDs with enhanced protrusion electrodes”, *J. Display Technol.* **7**, 359-361 (2011).
- [5] J. Yan, L. Rao, M Jiao, Y. Li, H. C. Cheng, and S. T. Wu, “Polymer-stabilized optically isotropic liquid crystals for next-generation display and photonics applications”, *J. Mater. Chem.* **21**, 7870-7877 (2011).
- [6] Y. Li and S. T. Wu, “Polarization independent adaptive microlens with a blue-phase liquid crystal”, *Opt. Express* **19**, 8045-8050 (2011).
- [7] J. Yan, Y. Li, and S. T. Wu, “High-efficiency and fast-response tunable phase grating using a blue phase liquid crystal”, *Opt. Lett.* **36**, 1404-1406 (2011).
- [8] Y. Li, M. Jiao and S. T. Wu, “Transfective display using a polymer-stabilized blue-phase liquid crystal”, *Opt. Express* **18**, 16486-16491 (2010).
- [9] J. Yan, H. C. Cheng, S. Gauza, Y. Li, M. Jiao, L. Rao, and S. T. Wu, “Extended Kerr effect of polymer-stabilized blue-phase liquid crystals”, *Appl. Phys. Lett.* **96**, 071105 (2010).

- [10] M. Jiao, Y. Li, and S. T. Wu, “Low voltage and high transmittance blue-phase liquid crystal displays with corrugated electrodes”, *Appl. Phys. Lett.* **96**, 011102 (2010).
- [11] Y. Li, T. X. Wu, and S. T. Wu, “Broadband wide-incident-angle polarization converter using liquid crystal films”, *J. Soc. Info. Display* **17**, 849-852 (2009).
- [12] Y. Li, T. X. Wu, and S. T. Wu, “Design optimization of reflective polarizers for LCD backlight recycling”, *J. Display Technol.* **5**, 335-340 (2009).
- [13] Y. Li, Z. Ge, and S. T. Wu, “A simple transflective LCD for mobile applications”, *J. Display Technol.* **5**, 319-322 (2009).
- [14] M. Jiao, S. Gauza, Y. Li, J. Yan, S. T. Wu, and T. Chiba, “Negative A-plates for broadband wide-view liquid crystal displays”, *Appl. Phys. Lett.* **94**, 101107 (2009).
- [15] Y. Li, Z. Ge, R. Lu, M. Jiao, and S. T. Wu, “Fast-response liquid crystal displays using crossed fringe fields”, *J. Soc. Info. Display* **16**, 1069-1074 (2008).

Conference Proceedings:

- [1] Y. Li, Y. Chen, J. Sun, S. T. Wu, S. H. Liu, P. J. Hsieh, K. L. Cheng, J. W. Shiu, S. Yamamoto and Y. Haseba, “Frequency Effects on Polymer-Stabilized Blue-Phase Liquid Crystals”, SID Display Week 2012, Los Angeles, Boston, MA, June 2012.
- [2] Y. Li and S. T. Wu, “Polarization independent adaptive microlens with a blue-phase liquid crystal”, SID Display Week 2011, Los Angeles, CA, May 2011. (Distinguished Student Paper ).
- [3] Y. Li, M. Jiao and S. T. Wu, “A wide-view transflective display using a polymer-stabilized blue-phase liquid crystal”, SPIE Photonics West, Invited Talk, San Francisco, CA, Jan. 2011.
- [4] M. Jiao, Y. Li and S. T. Wu, “Low voltage and high transmittance blue-phase liquid crystal

displays with corrugated electrodes”, SID Display Week 2010, Seattle, WA, May 2010.

[5] S. T. Wu, Z. Ge, C. C. Tsai, M. Jiao, S. Gauza and Y. Li, “Enhancing the energy efficiency of TFT-LCDs”, SID Display Week 2009, San antonio, TX, June 2009.

[6] Y. Li, Z. Ge and S. T. Wu, “A simple transfective LCD for mobile display applications”, SID Display Week 2009, San antonio, TX, June 2009.

[7] Y. Li, Z. Ge, R. Lu, M. Jiao and S. T. Wu, “Wide-view and fast-response LCDs using crossed fringe field switching effect”, International Display Research Conference, Orlando, FL, Nov. 2008.

U.S. Patent:

[1] Y. Li, M. Jiao, S. T. Wu, Y. P. Chang, M. H. Yang, and C. C. Tsai, "DISPLAY DEVICE WITH PATTERNED ELECTRODES", U.S. patent application 13/348, 652 (2012).

## LIST OF REFERENCES

- [1] D. K. Yang and S. T. Wu, *Fundamentals of Liquid Crystal Devices* (Wiley, 2006).
- [2] P. G. de Gennes and J. Prost, *The Physics of Liquid Crystals* 2nd ed. (Clarendon, Oxford, 1993).
- [3] J. P. Sethna S. Meiboom, W. P. Anderson, and W. F. Brinkman, *Phys. Rev. Lett.* **46**, 1216 (1981).
- [4] R. Memmer, *Liq. Cryst.* **27**, 533 (2000).
- [5] P. P. Crooker, *Chirality in Liquid Crystals*, Editors: H. S. Kitzerow and C. Bahr. (Springer, New York, 2001).
- [6] A. Saupe, *Mol. Cryst. Liq. Cryst.* **7**, 59 (1969).
- [7] J. Yan and S. T. Wu, *Opt. Materials Express* **1**, 1527 (2011).
- [8] H. Kikuchi, *Liquid Crystalline Blue Phases* (Springer Berlin, Heidelberg, 2008).
- [9] H. Choi, H. Higuchi, and H. Kikuchi, *Soft Matter*. **7**, 4252 (2011).
- [10] H. J. Coles and M. N. Pivnenko, *Nature* **436**, 997 (2005).
- [11] H. Yoshida, Y. Tanaka, K. Kawamoto, H. Kubo, T. Tsuda, A. Fujii, S. Kuwabata, H. Kikuchi, and M. Ozaki, *Appl. Phys. Express* **2**, 121501 (2009).
- [12] E. Karatairi, B. Rozic, Z. Kutnjak, V. Tzitzios, G. Nounesis, G. Cordoyiannis, J. Thoen, C. Glorieux, and S. Kralj, *Phys. Rev. E* **81**, 041703 (2010).
- [13] H. Kikuchi, M. Yokota, Y. Hisakado, H. Yang, and T. Kajiyama, *Nat Mater.* **1**, 64 (2002).
- [14] J. Kerr, *Philos. Mag.* **50**, 337 (1875).
- [15] H. Stegemeyer and F. Porsch, *Phys. Rev. A* **30**, 3369 (1984).
- [16] H. S. Kitzerow, *Mol. Cryst. Liq. Cryst.* **202**, 51 (1991).

- [17] J. Yan, H. C. Cheng, S. Gauza, Y. Li, M. Z. Jiao, L. H. Rao, and S. T. Wu, *Appl. Phys. Lett.* **96**, 071105 (2010).
- [18] P. R. Gerber, *Mol. Cryst. Liq. Cryst.* **116**, 197 (1985).
- [19] L. Rao, J. Yan, and S. T. Wu, *J. Inf. Display* **18**, 954 (2010).
- [20] S. T. Wu, *Phys. Rev. A*, **33**, 1270 (1986).
- [21] H. C. Cheng, J. Yan, T. Ishinabe, and S. T. Wu, *Appl. Phys. Lett.* **98**, 261102 (2011).
- [22] K. M. Chen, S. Gauza, H. Xianyu, and S. T. Wu, *J. Display Technol.* **6**, 49 (2010).
- [23] Z. Ge, S. Gauza, M. Jiao, H. Xianyu, and S. T. Wu, *Appl. Phys. Lett.* **94**, 101104 (2009).
- [24] L. Rao, J. Yan, S. T. Wu, S. I. Yamamoto, and Y. Haseba, *Appl. Phys. Lett.* **98**, 081109 (2011).
- [25] L. Rao, Z. Ge, S. T. Wu, and S. H. Lee, *Appl. Phys. Lett.* **95**, 231101 (2009).
- [26] Y. Li, Y. Chen, J. Sun, S. T. Wu, S. H. Liu, P. J. Hsieh, K. L. Cheng, and J. W. Shiu, *Appl. Phys. Lett.* **99**, 181126 (2011).
- [27] K. S. Cole and R. H. Cole, *J. Chem. Phys.* **9**, 341 (1941).
- [28] T. K. Bose, B. Campbell, S. Yagihara, and J. Thoen, *Phys. Rev. A* **36**, 5767 (1987).
- [29] K. M. Chen, S. Gauza, H. Xianyu, and S. T. Wu, *J. Display Technol.* **6**, 318 (2010).
- [30] M. Mori, T. Hatada, K. Ishikawa, T. Saishouji, O. Wada, J. Nakamura, and N. Terashima, *J. Soc. Inf. Display* **7**, 257 (1999).
- [31] Y. Li and S. T. Wu, *J. Display Technol.* **7**, 359 (2011).
- [32] A. Lien, *Appl. Phys. Lett.* **57**, 2767 (1990).
- [33] Z. Ge, T. X. Wu, X. Zhu, and S. T. Wu, *J. Opt. Soc. Am. A* **22**, 966 (2005).
- [34] Y. Li, M. Jiao and S. T. Wu, *Opt. Express* **18**, 16486 (2010).



- [35] X. Zhu, Z. Ge, T. X. Wu, and S. T. Wu, *J. Display Technol.* **1**, 15 (2005).
- [36] Z. Ge and S. T. Wu, *Transflective Liquid Crystal Displays* (Wiley, New York, 2010).
- [37] J. H. Lee, X. Zhu, and S. T. Wu, *J. Display Technol.* **3**, 2 (2007).
- [38] C. H. Chen, F. C. Lin, Y. T. Hsu, Y. P. Huang, and H. P. Shieh, *J. Display Technol.* **5**, 34 (2009).
- [39] Z. Ge, M. Jiao, R. Lu, T. X. Wu, S. T. Wu, W. Y. Li, and C. K. Wei, *J. Display Technol.* **4**, 129 (2008).
- [40] C. H. Lin, Y. R. Chen, S. C. Hsu, C. Y. Chen, C. M. Chang, and A. Lien, *J. Display Technol.* **4**, 123 (2008).
- [41] O. Itou, S. Hirota, J. Tanno, M. Morimoto, K. Igeta, H. Imayama, S. Komura, and T. Nagata, *Jpn. J. Appl. Phys.* **47**, 7195 (2008).
- [42] S. Pastoor and M. Wopking, *Display*, **17**, 100 (1997).
- [43] A. Stern and B. Javidi, *Proc. IEEE*, **94**, 591 (2006).
- [44] M. G. H. Hiddink, S.T. de Zwart, O.H. Willemsen and T. Dekker, *SID Tech. Dig.* **37**, 1142 (2006).
- [45] B. Javidi, F. Okano, and J.-Y. Son, *Three-Dimensional Imaging, Visualization and Display Technology* (Springer-Verlag, New York, 2008).
- [46] S. A. Benton and V. M. Bove, *Holographic Imaging* (Wiley, New York, 2008).
- [47] Y. J. Wu, Y. S. Jeng, P. C. Yeh, C. J. Hu, and W. M. Huang, *SID Tech. Dig.* **39**, 260 (2008).
- [48] M. Cho, M. Daneshpanah, I. Moon and B. Javidi, *Proc. IEEE* **99**, 556 (2011).
- [49] H. Liao, M. Iwahara, Y. Katayama, N. Hata, and T. Dohi, *Opt. Lett.* **30**, 613 (2005).
- [50] B. Lee, S. Jung, S. W. Min, and J. H. Park, *Opt. Lett.* **26**, 1481 (2001).

- [51] Y. Kim, J. H. Park, H. Choi, J. Kim, S. W. Cho, and B. Lee, *Appl. Opt.* **45**, 4334 (2006).
- [52] K. Ueda, T. Koike, K. Takahashi, and T. Naemura, *Proc. SPIE* **6803**, 68031A (2008).
- [53] N. A. Riza and M. C. Dejule, *Opt. Lett.* **19**, 1013 (1994).
- [54] A. F. Naumov, M. Yu. Loktev, I. R. Guralnik, and G. Vdovin, *Opt. Lett.* **23**, 992 (1998).
- [55] Y. Choi, J. H. Park, J. H. Kim, and S. D. Lee, *Opt. Mater.* **21**, 643 (2002).
- [56] H. Ren, Y. H. Fan, and S. T. Wu, *Opt. Lett.* **29**, 1608 (2004).
- [57] Y. H. Fan, H. Ren, X. Liang, H. Wang, and S. T. Wu, *J. Display Technol.* **1**, 151 (2005).
- [58] Y. H. Lin, H. S. Chen, H. C. Lin, Y. S. Tsou, H. K. Hsu, and W. Y. Li, *Appl. Phys. Lett.* **96**, 113505 (2010).
- [59] Y. Li and S. T. Wu, *Opt. Express* **19**, 8045 (2011).
- [60] S. T. Wu, *Phys. Rev. A* **33**, 1270 (1986).
- [61] C. T. Lee, Y. Li, H. Y. Lin and S. T. Wu, *Opt. Express* **19**, 17402 (2011).
- [62] Y. Li, Y. Liu, Q. Li, and S. T. Wu, *Appl. Opt.* **51**, 2568 (2012).
- [63] A.F. Naumov and G. Vdovin, *Opt. Lett.* **23**, 1550 (1998).
- [64] M. Jiao, J. Yan, and S. T. Wu, *Phys. Rev. E* **83**, 041706 (2011).